Spring 2011

# Constitutive mechanical properties of carpal tunnel soft tissue structures

Erin Kimberly Main
*University of Iowa*

# CONSTITUTIVE MECHANICAL PROPERTIES OF CARPAL TUNNEL SOFT TISSUE STRUCTURES

by

Erin Kimberly Main

A thesis submitted in partial fulfillment
of the requirements for the Master of
Science degree in Biomedical Engineering
in the Graduate College of
The University of Iowa

May 2011

Thesis Supervisors: Research Assistant Professor Jessica Goetz
Professor Thomas Brown

Graduate College
The University of Iowa
Iowa City, Iowa

CERTIFICATE OF APPROVAL

_____

MASTER'S THESIS

_____

This is to certify that the Master's thesis of

Erin Kimberly Main

has been approved by the Examining Committee
for the thesis requirement for the Master of Science
degree in Biomedical Engineering at the May 2011 graduation.

Thesis Committee: _____
Jessica Goetz, Thesis Supervisor

_____
Thomas Brown, Thesis Supervisor

_____
Nicole Grosland

_____
Madhavan Raghavan

ACKNOWLEDGMENTS

I would like to thank my advisors Dr. Jessica Goetz and Dr. Thomas Brown for their invaluable guidance and support during the course of this project. I am grateful for the opportunity to work and the learning experiences provided during the last two years in the Orthopaedic Biomechanics Laboratory. I would like to offer a special thank you for Dr. M James Rudert and Tom Baer for their assistance with the design and construction of the various testing devices used in this project. I appreciate the assistance I received from Dr. Yuki Tochigi and Dr. Anneliese Heiner during the initial tissue dissections and in the programming and set-up of the different testing protocols. I would also like to thank Noelle Klocke and Curtis Goreham-Voss for the help with pilot work and the optimization routine. Finally, thanks to my officemates, co-workers, and family for their help and support. Financial support provided by NIH grant AR 053899.

TABLE OF CONTENTS

LIST OF TABLES

LIST OF FIGURES

# CHAPTER I: INTRODUCTION

## Overview of Carpal Tunnel Syndrome

Median nerve compression within the carpal tunnel was first described in 1854, but it was not until the mid 1900s that the term carpal tunnel syndrome (CTS) was first introduced (Stecco and Aldegheri 2008). Only recently have studies begun to address the role of soft tissue biomechanics in the development of CTS. Although the exact cause of CTS is not known, increased pressure within the tunnel and elevated stress on the median nerve from contact with the surrounding structures may be possible mechanisms of insult to the median nerve (Viikari-Juntura and Silverstein 1999). To accurately evaluate contact stresses on the median nerve, physiologically relevant constitutive material properties are needed for the soft tissue within the carpal tunnel and determining these properties is the purpose of this work.

The American Academy of Orthopaedic Surgeons define CTS as a symptomatic compression neuropathy of the median nerve at the level of the wrist, characterized physiologically by evidence of increased pressure within the carpal tunnel and decreased function of the nerve at that level (AAOS 2007). CTS symptoms include tingling, numbness, and pain in the thumb, index, middle, and radial side of the ring finger, as well as on the radial side of the palm (Phalen 1966). Today, this condition accounts for approximately 90% of all entrapment neuropathies (Aroori and Spence 2008). The yearly incidence of CTS in the United States is 1-3 cases per 1000 persons and the prevalence is 50 cases per 1000 persons (AAOS 2007). Treatment of CTS leads to 400,000 to 500,000 carpal tunnel release surgeries being performed each year in the United States, at an annual economic cost of over $2 billion (Palmer and Hanrahan 1995).

A variety of non-occupational patient factors have been identified in association with the development of CTS. Several studies have acknowledged the strong female

gender bias linked with this neuropathy (Aroori and Spence 2008; AAOS 2007; Mondelli, Giannini, and Giacchi 2002). Specifically, comparative studies have found CTS incidence to be between 1.51 and 2.07 times higher in females than in males (Stevens et al. 1988; Bland and Rudolfer 2003). Other patient risk factors that have been linked to CTS include diabetes, arthritis, obesity, and pregnancy (AAOS 2007; Sperka et al. 2008).

CTS has also been reported in association with occupations requiring repetitive hand and wrist motions (AAOS 2007; Sperka et al. 2008). The United States Bureau of Labor Statistics has reported that for individuals suffering from CTS, the median number of days away from work after diagnosis was 27. This duration of disability ranks CTS the highest among the other major disabling workplace injuries and illnesses, such as fractures, amputations, and tendonitis (BLS 1999). In a study of individuals who had filed CTS-related worker's compensation claims, the percentage of respondents reporting persistent symptoms interfering with their work 4 years post-claim was 53%, with job loss reported by 38%. Out of that same group of respondents, 64% reported that their lingering symptoms interfered with home and recreational activities, and 44% reported that the symptoms interfered with sleep (Keogh et al. 2000). Such persistent symptoms can lead to huge indirect costs. For example, a study of CTS claimants in Washington state found that the cumulative loss in earnings for the individuals that were followed for CTS was between $197 million and $382 million over a 6 year period (Foley, Silverstein, and Polissar 2007).

## Diagnosis and Treatment of Carpal Tunnel Syndrome

There has been no single test that has been identified as a "gold standard" for the diagnosis of CTS; however, the American Society of Orthopaedic Surgeons has set forth a list of recommended guidelines for the diagnosis of this neuropathy. The first of these diagnostic recommendations includes an assessment of the patient's history including nature, location, and duration of symptoms (AAOS 2007). The primary CTS

symptoms are tingling or numbness in the distribution of the median nerve. Less common symptoms include weakness, clumsiness, and radiating pain to the arm and shoulder (Aroori and Spence 2008). CTS symptoms can be either intermittent or persistent, and in some cases they may be expressed exclusively at night (Kendall 1988). Symptoms can also be exacerbated by certain activities, such as driving or holding a telephone (AAOS 2007).

Based on the patient's history, the AAOS diagnostic guidelines then suggest a physical examination. This examination should include an evaluation of the hand/wrist range of motion, pinch/grasp strength, and manual muscle testing to examine for any atrophy of the muscles in the palm of the hand (AAOS 2007). Provocative tests such as Phalen's test and Tinel's sign may also be useful for diagnosis. Phalen's test is conducted by placing the patient's wrist in maximum flexion for 60 seconds. For Tinel's sign the patient is repeatedly tapped over the volar surface of the wrist. For both tests, a positive result occurs if the patient experiences paresthesia or tingling in the distribution area of the median nerve (Katz and Simmons 2002). A review by Katz and Simmons reported sensitivities and specificities of Phalen's test from 40% to 80%, and sensitivities of Tinel's sign of 25% to 60%, with specificities of 67% to 87% (Katz and Simmons 2002).

If the patient history and physical examination indicate CTS, nerve conduction studies are recommended prior to surgical intervention (AAOS 2007). Nerve conduction studies measure the conduction velocity of the median nerve within the region of the carpal tunnel. Surface electrodes are secured to the base of the ring finger and approximately 13 cm proximal to that location on the arm. A small electric current is applied to the arm electrode and propagation of that electrical potential along the median nerve is measured using the distal electrode. In CTS patients, demyelination of the median nerve can occur leading to a delay in its conduction velocity (Aroori and Spence 2008). Based on a review by Aroori and Spence, electrodiagnostic tests can be

expected to have sensitivities between 49% and 84%, and specificities of 95% to 99% (Aroori and Spence 2008).

After a diagnosis has been made, there are both surgical and non-surgical (conservative) treatment options for CTS. Non-surgical treatments include the use of hand braces, anti-inflammatory drugs, workplace modifications, and local corticosteroid injections. These treatments are typically recommended for individuals who present with mild to moderate CTS, as classified by lack of muscle atrophy and minimal delay in median nerve conduction velocity on electrodiagnostic tests (Aroori and Spence 2008). For patients with severe CTS, surgical treatment is recommended. Surgical treatment involves the complete division (transection) of the transverse carpal ligament (TCL) in order to increase the size of the carpal tunnel, thereby relieving the pressure on the median nerve. Carpal tunnel release surgery can be performed using either open or endoscopic techniques. A variety of studies have compared the long-term outcome of these two surgical alternatives, and no clear difference in patient outcomes has been found (Bickel 2010). However, in the short term, endoscopic release has been shown to produce less post-operative pain and to allow patients to return to activity in a shorter period of time (Bickel 2010). The success of carpal tunnel release surgery has been well documented, with 88% of patients reporting a reduction in symptoms and 79% reporting functionality improvement post-surgery (Badger et al. 2008).

## Anatomy of the Carpal Tunnel

The high incidence of CTS, as compared with other compressive neuropathies, results from the median nerve's vulnerable location within the carpal tunnel. The carpal tunnel itself is an osseoligamentous compartment located at the base of the hand. It is bounded by the transverse carpal ligament (TCL) on the volar (palmar) side and by two rows of carpal bones on the medial, lateral, and dorsal sides (Figure 1). Externally, the proximal bound of the tunnel is defined using a line drawn along the volar wrist crease.

The distal bound is represented by the intersection of a line through the center of the long finger and Kaplan's cardinal line, which is drawn parallel to an abducted thumb (Rotman and Donovan 2002). Internally, these tunnel bounds can be defined using the carpal bones themselves, with the proximal edge of the pisiform and the distal edge of the hook of the hamate delineating the proximal and distal bounds of the tunnel, respectively.

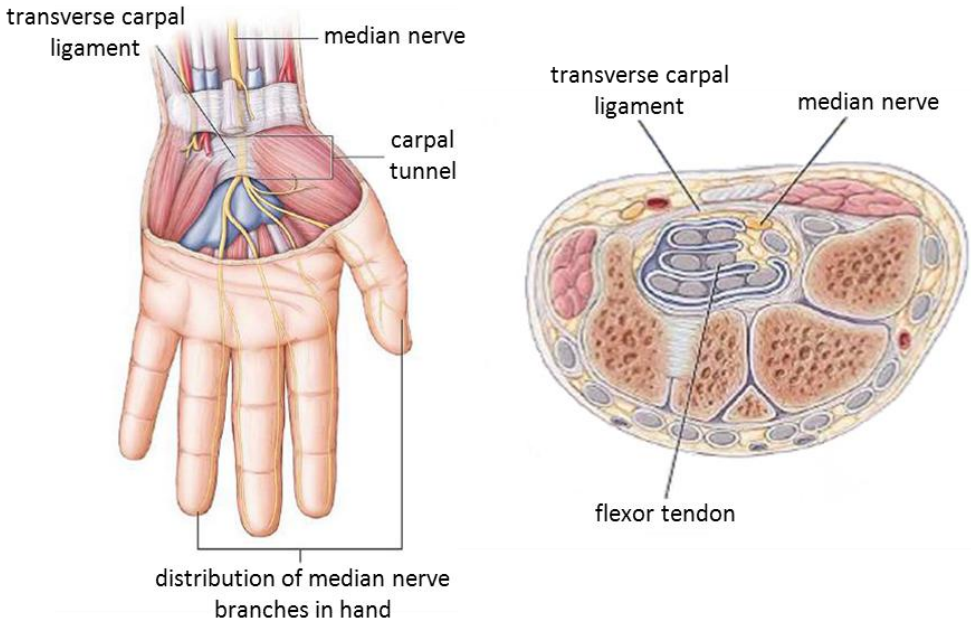


Figure 1. Carpal tunnel anatomy, adapted from (Katz and Simmons 2002).

The terms TCL and flexor retinaculum have often been used synonymously to describe the ligamentous structure that forms the volar bound of the carpal tunnel. This has led to confusion about the particular anatomy described by each term. One of the more widely accepted terminologies was defined by Cobb et al. (1993), who described the flexor retinaculum as being comprised of three distinct sections, one of which is the TCL. The distal section of the retinaculum is an aponerosis that spans from the thenar

to the hypothenar muscles. The proximal region of the flexor retinaculum lies under the antebrachial facia and is formed by a thickening of the deep investing forearm fascia. The central region of the retinaculum is comprised of the TCL proper, and it is this structure which forms the volar bound of the carpal tunnel. This ligament has bony attachments radially on the tuberosity of the scaphoid and the ridge of the trapezium and on the ulnar side on the pisiform and the hook of the hamate (Cobb et al. 1993). A second study (Stecco et al. 2010) has also characterized the tissue within the central flexor retinaculum region. Two histologically distinct fibrous regions were identified subcutaneously on the volar side of the hand, with the dorsal-most region having a more ligament-like appearance. Based on that finding, Stecco et al. went on to suggest the use of the term "TCL" to refer to the ligamentous structure that spans between the carpal bones, and that the term "flexor retinaculum" be abandoned since it does not adequately describe a specific region (Stecco et al. 2010).

The surface of the TCL makes an angle of approximately 24˚ with the palm as the ligament runs in the dorsal direction. The ligament is spindle-shaped in the medial/lateral direction, being widest in the proximal/distal direction at its attachment sites on the carpal bones and shortest in the center of the palm. The central width of the TCL in the proximal/distal direction is approximately 24 to 36 mm, and it is thinnest at its proximal (0.6 – 2 mm) and distal (0.1 – 1 mm) edges. It is thickest in the center (1.6 - 3.6 mm) (Rotman and Donovan 2002).

The contents of the carpal tunnel include the nine digital flexor tendons, as well as the median nerve. The nine digital flexor tendons consist of four flexor digitorum superficialis (FDS) and four flexor digitorum profundus (FDP) tendons that run to the index, middle, ring and little fingers, as well as the flexor pollisis longus (FPL) tendon, which runs to the thumb (Rotman and Donovan 2002). The flexor tendons originate proximal to the carpal tunnel from the extrinsic finger flexor muscles (Armstrong and Chaffin 1978). Within the bounds of the carpal tunnel, the FDP (or deep) tendons are

typically located on the dorsal side of the tunnel with the FDS (or superficial) tendons stacked volarly above them. After traversing the tunnel in a tight group, the tendons diverge to their respective digits. Lumbrical muscles arise from and insert on the flexor tendons distal to the tunnel boundary, and provide the coordination needed to link the flexion and extension of each digit. At the mid-level of the proximal phalanx, the superficial tendons divide to allow for the passage of the deep tendons to the volar side of the hand. The divided superficial tendons reunite on the dorsal side of the deep tendons. The superficial tendons split again and attach on medial and lateral sides of the middle phalanx, while the deep tendons insert on the volar side of the distal phalanx. The deep tendons are responsible for flexion of the distal phalanx, while the superficial tendons perform flexion of the proximal interphalangeal joints (Idler 1985).

The median nerve is typically located on the radial/volar side of the carpal tunnel, directly beneath the transverse carpal ligament and superficial to the tendons. The nerve is typically a single bundle within the tunnel, and branches upon exiting distally to innervate the radial side of the hand (Phalen 1966).

## Carpal Tunnel Mechanics

Contraction of the extrinsic finger flexor muscles causes flexion of the finger joints via gliding of the flexor tendons around a system of pulleys including the TCL, palmar aponerosis, and digital fibro-osseous canal (Goodman and Choueka 2005) (Figure 2). The TCL supports the flexor tendons during wrist flexion (Armstrong, 1978). The palmar aponeurosis pulley is located distal to the TCL and approximately 1.0 cm proximal to the metacarpophalangeal joint (Goodman and Choueka 2005). In the fingers, a series of annular and cruciate pulleys surround the tendons to form the digital fibro-osseous canal. This series of pulleys prevent bowstringing of the tendons from occurring during finger flexion. These pulleys also allow maximum flexion of the joint to occur with minimal flexor tendon excursion (Kline and Moore 1992).

The longitudinal excursion of the tendons though the tunnel is dependent upon the shortening of the muscles to which they are attached. Typically with the wrist in a neutral position, the FDP tendons have a mean excursion length of 32 mm, while the FDS tendons have a somewhat lower mean excursion value of 24 mm. The distance of tendon excursion has been shown to increase when wrist motion is allowed (Wehbe and Hunter 1985).

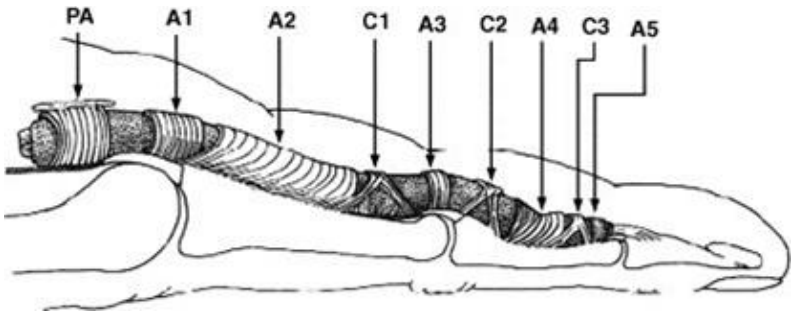


Figure 2. Pulley system for the digital flexor tendons with the palmar aponerosis (PA) and the series of annular (A) and cruciate (C) pulleys located in the fingers (Goodman and Choueka 2005).

The forces experienced by the digital flexor tendons *in vivo* can range from 0 to 8 N during passive motion (Dennerlein 2005). Ratios for the force experienced by the FDS relative to the applied fingertip force vary from 3.3 during a single finger press activity (Dennerlein 2005), up to 5.4 for a single finger tapping activity (Dennerlein et al. 1998). During pinch and grasp maneuvers, the ratio of the tendon force to the applied fingertip force for the FDP and FDS tendons of the index, long and little finger ranges from 0.73 up to 4.32 (Chao, Opgrande, and Axmear 1976). As a result of the excursions and loading experienced by the flexor tendons during finger motion and loading, the tendons themselves undergo a variety of transverse rearrangements within the tunnel (Figure 3) (Skie et al. 1990; Goetz et al. 2010). With these rearrangements, the median

nerve can become compressed or entrapped between the flexor tendons and the tunnel boundaries. This entrapment can cause the nerve to experience a variety of tensile, compressive, and shear forces between itself and adjacent structures in the tunnel (Bay, Sharkey, and Szabo 1997).

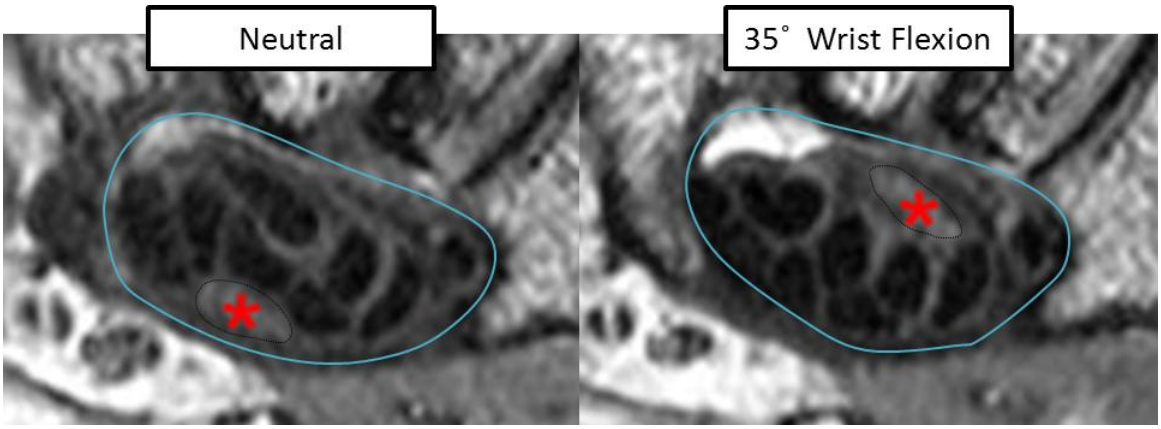


Figure 3. Cross-sectional magnetic resonance images at the level of the hook of the hamate illustrating transverse rearrangement of the flexor tendons and median nerve within the carpal tunnel when the wrist is moved from a neutral position to 35˚ flexion. Boundaries of the carpal tunnel are identified with the blue line and position of the median nerve is identified with a red asterisk.

## Motivation for Present Study

There are two major paradigms for the mechanism of injury to the median nerve leading to the onset of carpal tunnel syndrome. The first is nerve ischemia caused by increased pressure in the carpal tunnel, and the second is mechanical insult leading to elevated contact stresses on the median nerve (Viikari-Juntura and Silverstein 1999). Elevated carpal tunnel pressure has been observed in CTS patients as compared to normal control subjects (Rempel and Diao 2004). Carpal tunnel pressures have also been shown to increase with certain wrist postures and loading activities (Rempel and Diao 2004). It has therefore been suggested that with repetitive hand loading and wrist

motions continually elevating the pressure within the carpal tunnel, median nerve ischemia may result, subsequently triggering the onset of CTS (Rempel and Diao 2004).

A second potential mechanism leading to CTS symptoms is contact stress on the median nerve arising as a result of median nerve impingement by the flexor tendons or by the tunnel boundaries. Transverse rearrangements of the median nerve and flexor tendons within the carpal tunnel have been shown for a variety of different wrist angles and hand loading activities (Skie et al. 1990; Goetz et al. 2010). This rearrangement of the tissues within the carpal tunnel could result in compression of the median nerve. To date, however, only a single study has attempted to quantify the contact stresses on the median nerve associated with this potential CTS-inducing mechanism (Ko and Brown 2007). Patient-specific finite element (FE) analysis informed by magnetic resonance (MR) images provides an attractive non-invasive means to study the contact stresses that could develop on the median nerve. However, FE simulations for such purposes must incorporate physiologically realistic material properties of the tissues, in order to obtain accurate solutions. Transverse compressive forces are produced on the carpal tunnel tissues as a result of wrapping, rearrangement, and impingement events, but as of yet there is a lack of knowledge about how these tissues behave under compressive load. Thus, the purpose of this work was to characterize transverse material property behavior and constitutive properties for the digital flexor tendons, the median nerve, and the transverse carpal ligament.

# CHAPTER II: LITERATURE REVIEW

## Digital Flexor Tendons

There is an extensive body of literature (reviewed by Wang (2006), Summers and Kobb (2002), and many others) describing the mechanical behavior of tendons. The vast majority of these studies have focused on tendon longitudinal tensile behavior. This is logical, given that longitudinal loading is the normal functional modality for tendons. Stress-strain curves for tendon extension are characterized by an initial toe region which is attributed to the uncrimping of the collagen fibers. In this region there is a large, nonlinear deformation under low load. This toe region is followed by the linear region, the slope of which is frequently characterized by a Young's modulus (Goodman and Choueka 2005). In the few studies focusing on the material properties of digital flexor tendons, wide variation associated with species has been observed. For example, in ovine digital flexor tendons, a toe region modulus of 10.5 MPa and a linear region modulus of 34 MPa were measured (Lynch et al. 2003). These animal tissues were found to be much less stiff than the FDP and the FDS tendons of human cadaveric forearm specimens, which had an average Young's modulus value of 750 MPa under 6% strain (Harris, Walker, and Bass 1966).

In contrast to the abundance of literature describing the axial tensile behavior of tendons, only a very small number of investigations have addressed tendon transverse compressive behavior. Using unconfined compression experiments, the mean compressive modulus of rabbit patellar tendons was found to be 19.49 kPa (Williams et al. 2008). Other work (Lee et al. 2000) has addressed the local compressive stiffness of the human supraspinatus tendon using indentation testing. That work demonstrated a non-homogenous stiffness distribution on the bursal versus articular sides of the tissue. The compressive moduli of intrasynovial versus extrasynovial tendon fascicles from canine hind paws have been compared using indentation testing (Shin et al. 2008), with

the finding that extrasynovial tendons are less stiff than the intrasynovial ones. Finally, in another study by Kou et al. (2001), the elastic properties of bovine Achilles tendons were determined in planes parallel and perpendicular to the fiber axis using a cyclic compression-relaxation method. The ratio of the Young's modulus in the parallel direction to that in the perpendicular direction was approximately 4 for small strains, and decreased with increasing strain. This limited set of transverse compression studies employed differing measurement techniques for the respective tissue specimens involved, all of whose geometries and anatomical functions differ substantially from those of human digital flexor tendons within the human carpal tunnel.

## Median Nerve

Unlike the digital flexor tendons, the primary function of the median nerve is not to carry an axial load. Therefore, the nerve structurally does not have the axially oriented collagen fiber bundles comparable to those in tendons. Despite not being explicitly loaded in the longitudinal direction, however, longitudinal stretching of the median nerve can occur from frictional shear forces resulting from movement of adjacent flexor tendons, or from length changes in the nerve bed during joint flexion and extension (Bay, Sharkey, and Szabo 1997). An approximately linear relationship has been established between the longitudinal gliding of the flexor tendons and of the median nerve within the tunnel. Specifically, the average flexor tendon displacement needed for full finger flexion is 3 cm, which translates into 1 cm of longitudinal displacement of the median nerve (Szabo et al. 1994). Under tension, peripheral nerves have been shown to exhibit nonlinear load-deformation curves, with a long toe region and very low stiffness (Grewal et al. 1996). In a review by Grewal et al. (1996), the median nerve was reported to experience an ultimate load ranging between 73 N and 220 N, and to exhibit elastic behavior during elongations up to 11% to 17% longitudinal

strain. No frank structural damage to the median nerve was found prior to 20% to 32% nerve elongation (Grewal et al. 1996).

In contrast to the few studies investigating compression of digital flexor tendons, numerous studies have employed compression testing to address the pathomechanisms of peripheral nerve injury (Viikari-Juntura and Silverstein 1999). For example, Rydevik and Nordborn (1980) used a specially designed compression chamber to examine the acute and long-term effects of nerve compression on the signal conduction velocity of rabbit tibial nerves. Compression at 50 mmHg for two hours induced only minimal acute and no long-term effects on conduction velocity. However, reduced acute and long-term conduction velocity was observed with compression between 200 and 400 mmHg for two hours (Rydevik and Nordborg 1980). In a related study, changes in intraneural blood flow were evaluated in rabbit tibial nerves following graded compression. Venular flow was found to be impaired at pressures of 20 to 30 mmHg, while arteriolar and intrafascicular capillary flow were not compromised until reaching pressures of 40 to 50 mmHg (Rydevik, Lundborg, and Bagge 1981). Histological examination of rat sciatic nerves following compression has shown ischemia, axonal damage, and demyelination (Powell and Myers 1986).

Despite the numerous studies that have addressed pathological functional changes to peripheral nerves with compression injures, only a small subset of studies have addressed the transverse mechanical properties of nerve. The Young's modulus of rabbit sciatic nerves in the transverse direction was found to be 41.6 kPa, using a custom parallel compression apparatus (Ju, Lin, and Lin 2004). Radial compression experiments performed on rabbit sciatic nerves found the Young's modulus in the transverse direction to be 66.9 kPa (Ju et al. 2006). Another pair of studies utilizing a custom circular compression apparatus investigated the mechanical properties of sciatic nerves in normal and diabetic rats. The apparent Young's modulus was 210.7 kPa, which was approximately two times larger than the observed value for normal rats of

116.3 kPa (Chen, Lin, and Ju 2010b). In the second of these studies, a quasi-linear viscoelastic model was fit to the experimental compression data. The fitted data indicated that diabetic nerves have a lower amplitude of viscous response, and a viscoelastic stress relaxation response that requires a longer relaxation period to reach equilibrium (Chen, Lin, and Ju 2010a). Although these studies addressed transverse mechanical properties of nerves, they did so using nerve tissues that again are anatomically different from the median nerve of the human carpal tunnel.

## Transverse Carpal Ligament

As the volar bound of the carpal tunnel, the TCL serves as an important component of the pulley system for the digital flexor tendons. The carpal arch is formed between the TCL's insertion sites on the carpal bones on the radial and ulnar side of the hand. Since the median nerve can become compressed against the TCL during functional hand activities, an understanding of the mechanics of the TCL is of great importance.

Many studies have evaluated the functional properties of the carpal arch to better understand the use of TCL transection as a treatment option for CTS. In these studies, the TCL was found to contribute somewhat to the stability of the carpal tunnel during the application of radial/ulnar loads (Xiu et al., 2010; Tengrootenhuysen et al., 2009; Guo et al., 2008). However, when intact carpal tunnels were compressed in the dorso/palmar direction, the TCL was not found to play an essential role in maintaining carpal arch stability (Garcia-Elias et al. 1989).

In addition to studies which have evaluated the TCL's contribution to the stability of the carpal arch, other work has examined the TCL's role in moderating shape changes of the carpal tunnel. In a study by Li et al. (2009), carpal tunnel expansion was measured following the application of palmarly directed forces applied to the dorsal side of the TCL, using a lever apparatus. The cross-sectional area of the tunnel was

found to increase with increasing loads. The increase in tunnel area was attributed to a decrease in the arch width between the radial and ulnar bounds of the TCL, rather than lengthening of the TCL. The length of the TCL remained constant with applied loads up to 200 N. Thus, the increase in area was a result of the arching of the ligament in the volar direction, combined with the inward translation of the carpal bones. While these studies have evaluated the TCL's role in maintaining carpal arch dimensions and stability, no stiffness measurements of the carpal bone/TCL complex were obtained which would be relevant for implementation into FE models.

The compliance of human, dog, rabbit, and rat carpal tunnels has been evaluated using a tapered rod pulled distally though carpal tunnels from which the flexor tendons and median nerve had been removed. Humans were found to have the stiffest tunnel, with the canine tunnel being most mechanically similar (Tung et al. 2010). External compliance measures of the carpal tunnel, including the TCL, have also been made. Li (2005) measured the relationship between carpal tunnel compliance and gender using external indentation testing. The effective tunnel compliance for females was found to be 26.3% lower than that for males (Li 2005). Also, surface indentation has been performed on the volar surface of the hand using a cylindrical ultrasound palpation sensor. Compressive forces up to 20 N were applied, and the stiffness of the skin-TCL layer and TCL-carpal bone layer were measured and found to be 6.72 N/mm and 15.63 N/mm respectively (Zheng, 2006).

Despite the utility of these studies in understanding the TCL's role in maintaining carpal bone stability and the overall compliance of the carpal tunnel, only a few studies have isolated the TCL and assessed its properties independent of the tunnel. Lin et al. (1983) performed uniaxial tensile testing on excised TCL specimens from CTS patients and normal controls. Their results demonstrated no statistically significant difference in elastic properties between the two groups. In other work, the stiffness of the TCL was determined to be 131.8 N/mm, by means of tensile testing performed on bone-

ligament-bone preparations (Garcia-Elias et al. 1989). Although these studies addressed the constitutive mechanical properties of the TCL isolated from the entire carpal tunnel, they focused only on the tensile properties of the ligament in the radio/ulnar direction. However, contact between the TCL and the median nerve *in vivo* is compressive and occurs in a transverse plane. Thus, knowledge of the TCL's constitutive behavior in the transverse direction under compression is important for accurately predicting the contact stresses that develop on the median nerve as a result of contact with the TCL.

# CHAPTER III: TRANSVERSE COMPRESSIVE PROPERTIES OF THE DIGITAL FLEXOR TENDONS AND THE MEDIAN NERVE

One plausible mechanism of insult to the median nerve is impingement by the digital flexor tendons that co-occupy the tunnel. FE analysis of carpal tunnel structures during hand loading activities provides a systematic means to study this insult mechanism. However, knowledge of the transverse compressive properties of the flexor tendons and median nerve is needed for physiologically accurate contact stress analysis to be performed in that context. As discussed above, only a very limited number of studies have addressed the transverse compressive properties of tendon and nerve, and those few that have done so have investigated tissue structures whose anatomical function and geometry differ substantially from those of the digital flexor tendons and the median nerve. Thus, one purpose of this work was to obtain a material property definition for the compressive behavior of these tissue structures suitable for implementation into future FE models of the whole carpal tunnel. This was approached using a combination of experimental bench top testing, FE modeling, and optimization techniques.

## Experimental Compression Testing

Digital flexor tendons and median nerves were dissected from ten fresh frozen cadaveric forearm specimens (5 male and 5 female) with a mean age of 53 years (range of 30 to 65 years). The tissues were excised after specimens had been allowed to thaw at room temperature overnight. Proximal and distal tunnel boundaries were marked on each tissue structure prior to its removal from the hand, using sutures secured around the tissue (Figure 4). To account for longitudinal sliding of the flexor tendons within the tunnel during normal finger movements, the proximal bound of the flexor tendons was marked on the proximal side of the pisiform with the fingers in full extension. The distal bound was marked at the distal edge of the hook of the hamate with the fingers in

flexion. Both the proximal and distal boundaries were marked on the median nerve with the fingers in extension, using the same anatomical landmarks as used for the flexor tendons. The length of the flexor tendon that was encompassed anywhere within the carpal tunnel at some instance during finger flexion was on average 5 to 6 cm. Similarly, the length of the median nerve that was encompassed at some instance within the carpal tunnel averaged 4 cm. For testing, a tissue length of approximately 12 cm, centered on this bounded sector, was excised.


Figure 4. Excised superficial tendon, with proximal and distal tunnel encompassment extrema marked using sutures.

Following the excision of each tissue specimen from the tunnel, all subsynovial connective tissue, tendon sheath, and muscle were removed. The equivalent circular diameter of each specimen was determined to the nearest 0.25 mm using a purpose-developed set of gauges. Each gauge was comprised of two matching semicircular openings that when brought together forced the highly deformable tissue to conform to a circular cross-sectional area (Figure 5). The smallest circular hole that allowed unobstructed passage of the tissue was the tissue's equivalent circular diameter. Diameter measurements were taken in the region of the specimen that was to be compressed during testing, which was located 55 mm from the distal end of the specimen.

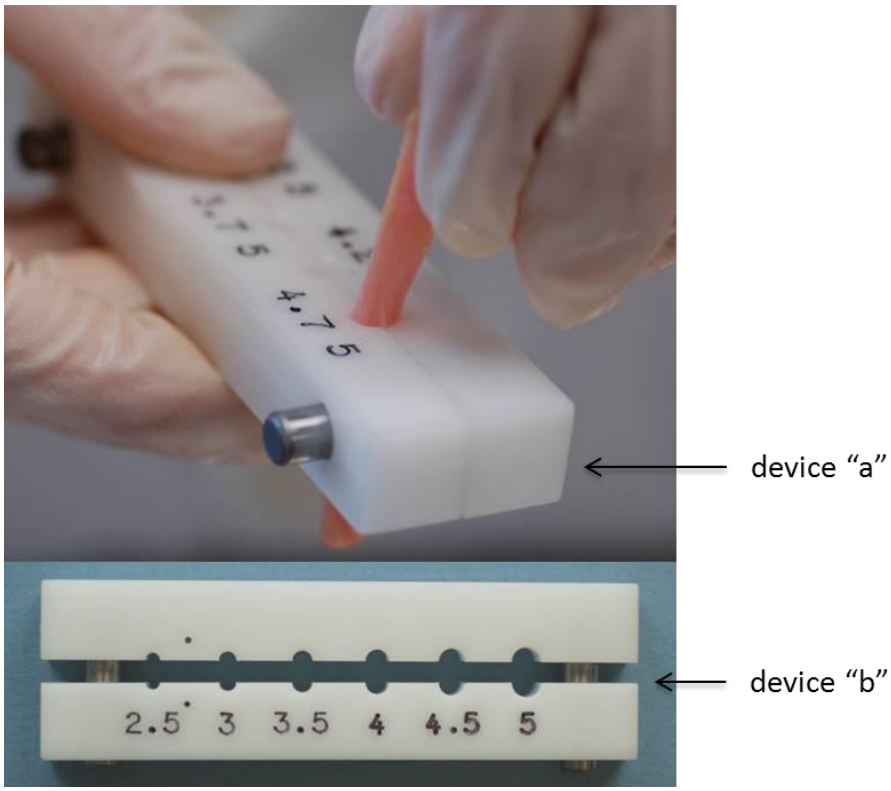


Figure 5. Use of a purpose-developed gauge to measure a nerve cross sectional area. Numeric values indicate circular diameter in millimeters. The full range of measurements was divided two smaller devices for easier handling (device “a” and device “b”).

Hollow cylindrical Delrin collars with an internal diameter matching the measured equivalent circular diameter were placed on the distal and proximal ends of each specimen. The collars that were applied to the median nerve were split along their length to ease application without damaging the fragile tissue. Specimens were then mounted in serpentine clamps for compression testing in a transverse testing apparatus designed and built by Dr. M. James Rudert (Figure 6). The Delrin collars were located directly outside of the serpentine clamps and served to prevent the tissue flattening caused by the clamping mechanism from extending into the testing region.

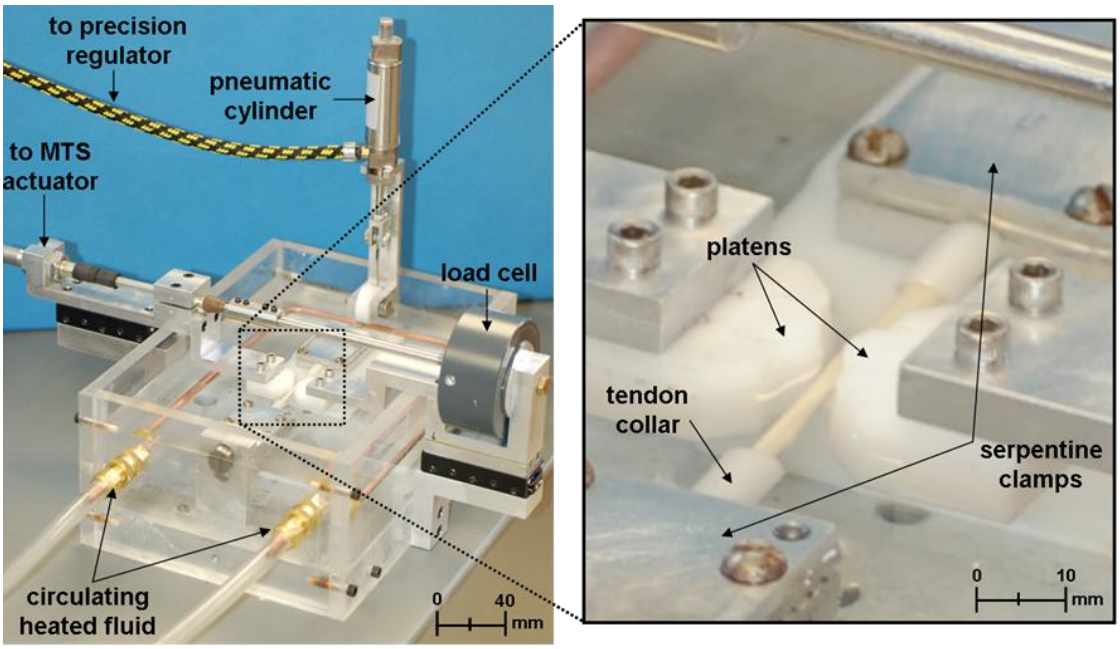


Figure 6. Transverse compression testing device, with tendon specimen mounted in the serpentine clamps. During testing, tendon collars prevented the flattening associated with clamping from extending into the central testing region (inset). Axial load was applied by a pneumatic cylinder controlled by a precision regulator. Transverse compression was applied via the convex Delrin platens, whose displacement was controlled by an MTS actuator.

Compression testing was performed with the tissues submerged in a 37 ˚C saline bath. The bath temperature was maintained using heated water circulated through copper tubing at the base of the testing fixture. Axial tension was applied to the tissue specimens through the serpentine clamps, using a pneumatic cylinder (Airpel E16 D1.0, Airpot Corp., Norwalk, CT, USA) controlled by a precision regulator with a pressure gauge (MGA-100, SSI Technologies, Inc., Janesville, WI, USA). Transverse compression of the flexor tendon and median nerve specimens was applied horizontally via two convex Delrin platens with a 5 mm radius of curvature. The platens were driven together in displacement control by an MTS 810 actuator to apply tissue compression. The entire platen/load cell construct was mounted on bearing slides (N-2 Bearing Slides, Del-Tron Precision, Inc., Bethel, CT, USA) and was allowed to displace horizontally. The “floating

platen" aspect of this apparatus allowed for compression to be applied equally to each side of the tissue structure, thus eliminating any bowing of the tissue during testing.

As a result of the native tissue morphology and use of the cylindrical Delrin collars, the physical cross-sectional shape of the tissue specimens within the apparatus was approximately elliptical. Prior to compression testing, each specimen's major axis was assessed within the testing apparatus, with the tendon or nerve was placed under initial axial pre-loads of 5 N or 3 N, respectively. During this assessment, the platens were brought together manually in 0.1 mm increments using the MTS under displacement control. The distance between the two convex platens at the instant of visually observed load uptake initiation was recorded as the major axis dimension of the specimen. The minor axis dimension of the tissue cross section was calculated using the following equation:

$$minor\ axis = \frac{4 * CSA}{\pi * major\ axis}$$

$$with\ CSA = \pi \left(\frac{equivalent\ circular\ diameter}{2}\right)^2$$

After axis dimension determination, compression testing was performed with the tendon and nerve under axial loads of 15 N or 5 N, respectively. The 15 N axial load used for the flexor tendons was based on measured tendon load during an isometric pinch activity with a fingertip force of roughly 5 N (Dennerlein 2005). Although not explicitly tensed during hand activity, the median nerve is subject to secondary longitudinal loading associated with friction from gliding of the actively loaded flexor tendons. For example, during finger flexion, the ratio of flexor tendon longitudinal displacement to median nerve longitudinal displacement has been shown to be approximately 3 to 1 (Szabo et al. 1994). Thus, for the transverse compression testing the nerve specimens were subjected to a reduced axial load (5 N).

Transverse compression was applied quasistatically (0.5 mm/sec) up to a total compression of 40% (Williams et al. 2008) of the specimen's major axis dimension. Compressive load uptake was measured with a 111.2 N (25 lbf) load cell (Sensotec 3167-25, Honeywell, Columbus, OH, USA) at a sampling rate of 1000 Hz. Compression tests were repeated three times per specimen, with a seven- or ten-minute recovery interval between tests for the tendons or the median nerve, respectively.

During compression of the tissue specimens, the testing apparatus itself and the MTS actuator cable underwent slight deflections, which if not accounted for would have introduced slight errors into the displacement data measured by the MTS. Overall device compliance was determined by bringing the platens into contact with each other with no specimen present. Platens were driven together under displacement control until the measured load exceeded 40 N, which was above the maximum force values observed for any of the tissue specimens during compression testing. When the loads were plotted against platen displacement, the resulting linear load/displacement curve indicated repeatable device behavior at all measured loads. The inverse of the slope of that force/displacement curve constituted the compliance of the device (0.0082 mm/N) (Figure 7). This tare compliance value was then used to correct the MTS-measured displacement values ($D_{MTS}$) to find the actual platen displacement ($D_{Platen}$), using the following equation:

$$D_{Platen} = D_{MTS} - (Force * 0.0082)$$

As a result of overcoming friction at the initiation of platen movement, and from resistance to the displacement of the platens through the fluid bath prior to tissue contact, the resulting force/displacement curves were slightly offset from 0 N at the beginning of the test. The curves included noise on the order of 0.05 to 0.1 N. To correct the curves to a zero force value prior to tissue contact, correction force values were calculated by averaging force data that were acquired prior to contact of the

platens with the tissue. This required starting the compression test with a gap of at least 1 mm between the platens and the tissue surface. This average force offset value was then subtracted from each measured force value in the tissue specimen's data set.

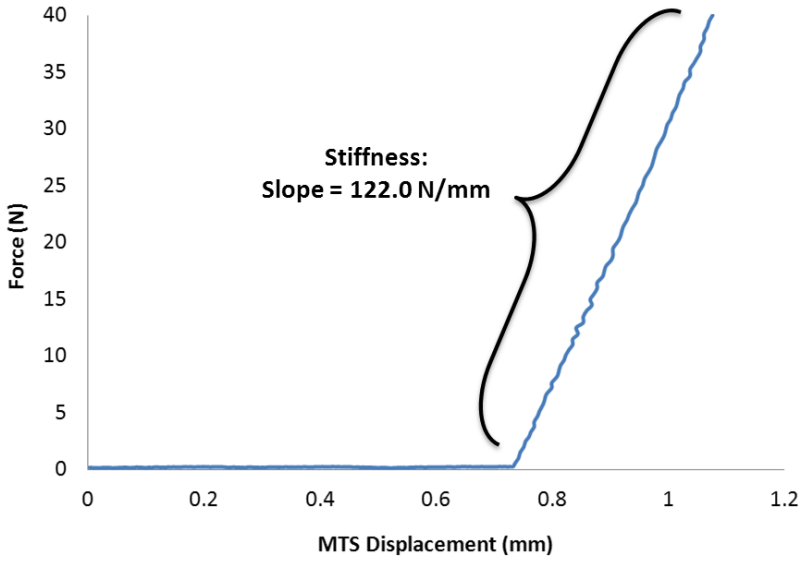


Figure 7. Force versus MTS displacement data obtained during the evaluation of the compliance of the testing apparatus. The slope of the graph corresponds to the stiffness of the device (122.0 N/mm). The inverse of this stiffness represented the device compliance (0.0082 mm/N ). This value was used to correct the experimentally measured transverse force/displacement data.

To decrease the noise in the force/displacement data, a boxcar filter was used on the transverse force values. An average was taken for the first 10 force values in each testing series. That average value replaced the raw tenth transverse force value in the series. A force average was then computed for the second through eleventh force values in the compression test, and this value replaced the eleventh transverse force value. This process was continued for the entire compression data set. The offset-corrected and filtered force/displacement data were then plotted, and the compression

test with the smoothest force/displacement curve from each specimen was selected for use in the subsequent finite element analysis.

## Finite Element Modeling

Specimen-specific FE models corresponding to each individual physical test were run in ABAQUS v6.9-1 (Simulia, Providence, RI, USA). Because many repeats of a given model were used in the optimization, half-tissue models divided down the symmetry plane (Figure 8) were used to reduce model run times. The convex cylindrical compression platen was modeled in ABAQUS CAE as a rigid surface, and was meshed with 2,500 rigid body (R3D4) elements. The rigid surface was geometrically identical to the platen used for testing: semicircular, 5 mm in curvature radius and 1.27 cm in height. FE meshes for each of the digital flexor tendons and median nerves were created using TrueGrid (XYZ Scientific Application, Inc., Livermore, CA, USA). Tissue specimens were modeled as prismatic, with an elliptical cross section defined using the major and minor axis tissue dimensions that had been determined during experimental testing. The tissue length that was modeled corresponded to the clamp-to-clamp distance measured during experimental testing while the specimen was under no axial load. Tissue specimens were meshed with 8-noded hybrid hexahedral continuum elements (C3D8H). The models had increased mesh refinement (8 elements/mm) in the longitudinal direction, centered on the platen contact region. The total number of elements in the model varied between 20,000 and 30,000, depending on the cross-sectional area and length of the tissue specimen.

The transverse compression of the tissue that had been performed experimentally was then modeled in ABAQUS. The ends of the tissue mesh were constrained against axial (z-direction) displacement during the analysis. This was consistent with tissue immobilization in the serpentine clamps during experimental

testing. The nodes along the symmetry plane were held fixed in the transverse direction, so as to represent the presence of the other half of the tissue (Figure 9).

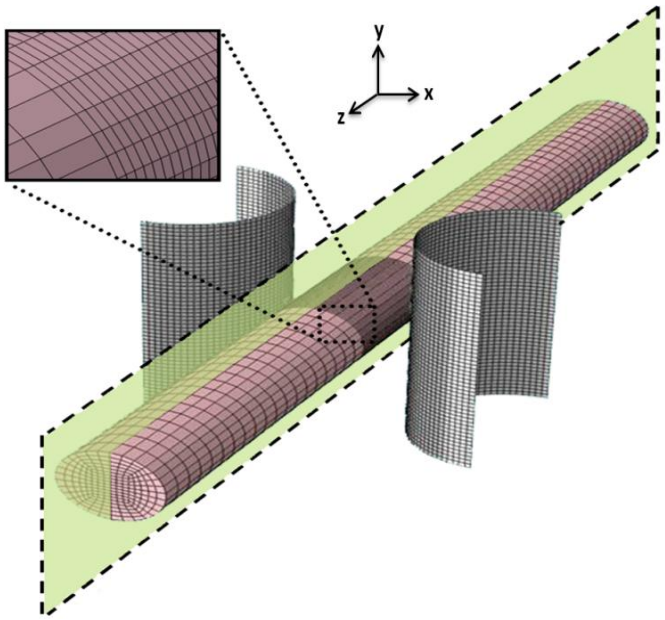


Figure 8. FE model corresponding to the experimental set up, with convex circular platens, and with the tissue cross-section approximated as an ellipse. The symmetry plane shows the division for the half-tissue model that was used to reduce run times.

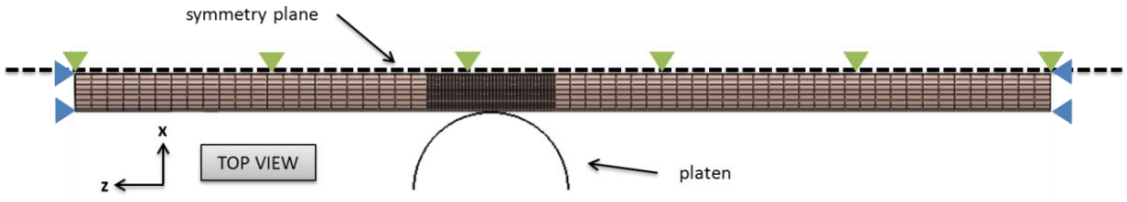


Figure 9. Top-down view of the half-tissue model used for analysis. Nodes located on the ends of the tissue were constrained against axial displacement in the z-direction (blue fixities). Nodes along the line of symmetry were constrained against movement in the x-direction (green fixities).

Two centrally located nodes on each end of the tissue mesh were held fixed in the transverse plane (x- and y-direction) to prevent rotation of the mesh during compression (Figure 10). Contact was defined between the rigid platen outer surface and the surface of the tissue mesh. Transverse compression in the FE model was displacement driven, with the displacement magnitude corresponding to the 40% major-axis strain that had been applied experimentally. Compression was prescribed through a rigid body reference node located at the center of the convex platen. The platen was constrained to allow movement only in the direction of experimental displacement (x-direction). Throughout the analysis, the rigid body reference node was used to collect reaction force data.

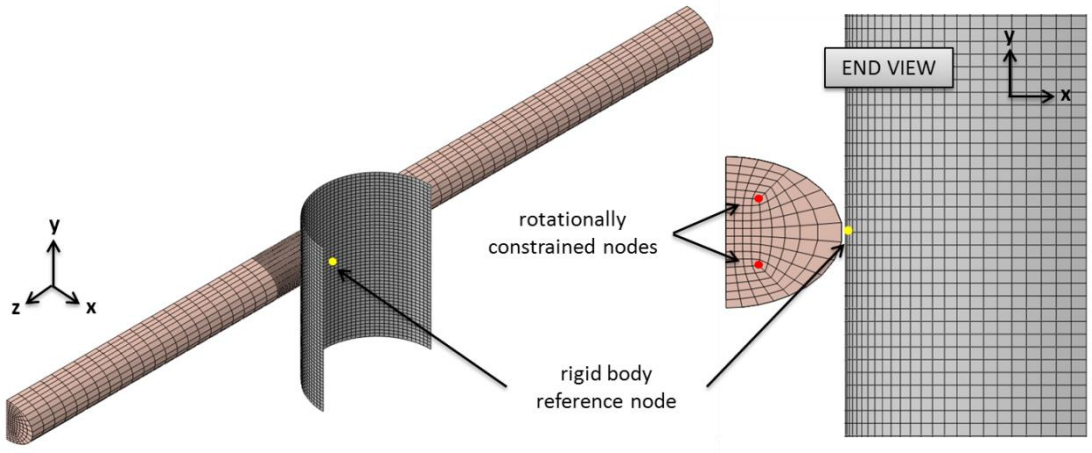


Figure 10. Orthogonal projection (left) and end view (right) of an illustrative FE model with the rigid body reference node used to drive the platen displacement indicated by the yellow dot. Two nodes (red dots) on each end of the tendon (or nerve) model were constrained in the x- and y-directions to prevent rigid body rotation.

A series of material property definitions were explored in the FE models to evaluate how well each constitutive characterization fit the experimental data. The first of these was the Neo-Hookean model, which utilizes a single coefficient to characterize

the relationship between strain energy and the first invariant of the left Cauchy-Green deformation tensor. However, the Neo-Hookean model did not impart enough nonlinearity to accommodate the extensive toe region associated with the tendon/nerve load uptake (Figure 11). The second candidate material property definition was the hyperelastic Mooney-Rivlin model, which is an expansion of the Neo-Hookean model implementing an added constant characterizing the contribution of the second invariant. With the Mooney-Rivlin model, additional nonlinearity was introduced that better captured the curvature of the experimental force/displacement curves. However, use of this model was precluded by its non-unique converged solutions for the fitted material constants.

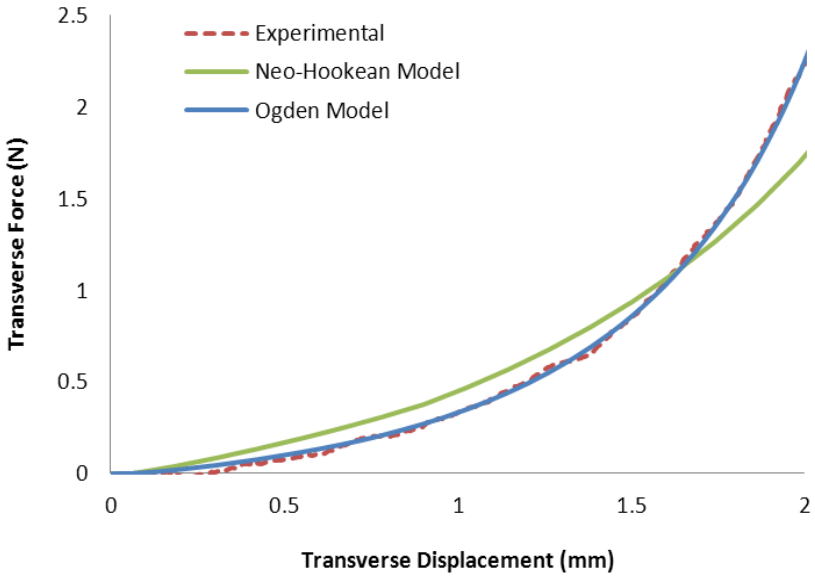


Figure 11. Example of fits achieved for an illustrative tendon with the Neo-Hookean and Ogden hyperelastic material property definition.

After identifying the shortcomings of the other two material property definitions investigated, a first-order Ogden hyperelastic constitutive definition was finally selected

for modeling the tendon and nerve transverse compressive behavior. This model gave acceptable fits to the nonlinear experimental data, using a minimal number of coefficients. And, optimization of the material coefficients did not result in the problem of non-unique solutions. For the first order Ogden constitutive model, strain energy (W) is expressed as a function of the deviatoric principal stretches ($\lambda_n$):

$$W(\lambda_1, \lambda_2, \lambda_2) = \frac{\mu}{\alpha^2}(\lambda_1^\alpha + \lambda_2^\alpha + \lambda_3^\alpha - 3)$$

The coefficients μ and α predominately reflect material behavior in the initial load uptake (toe) and in the linear (post-toe) region of the experimental stress-strain curve, respectively (Figure 12).

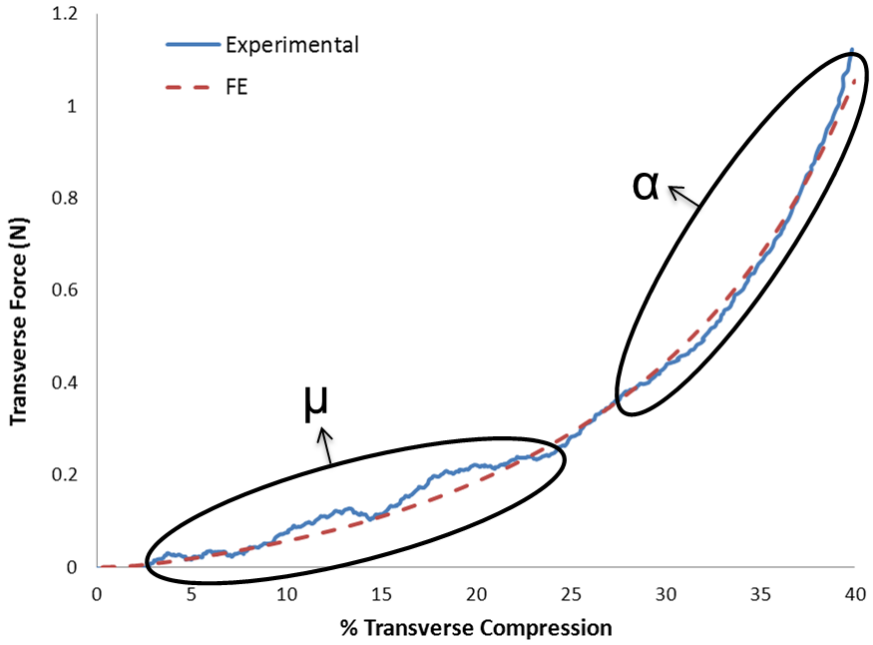


Figure 12. Transverse force/compression graph for an illustrative tendon, with experimental data plotted in blue and the FE model fit of the data plotted in red. The μ coefficient predominately affects the low-strain behavior or the initial load uptake region of the curve, whereas the α coefficient predominately affects the higher-strain behavior or the more linear post-toe region of the curve.

## Optimization Routine

Each specimen-specific FE model was used in conjunction with an automated least-squares nonlinear MATLAB (The Mathworks, Natick, MA, USA) optimization routine, to determine Ogden coefficients that best replicated the experimental load/deformation curve. To begin the optimization routine, initial values for the two Ogden coefficients ($\mu$ and $\alpha$) were loaded into the ABAQUS FE input file, and the FE model was run to completion in ABAQUS. Reaction force data from the rigid body reference node on the platen were written to an FE output file for each model time step. The step time and reaction force data were then extracted from this output file and read into MATLAB. Using the known rate of platen displacement applied in the FE model, the step time data were converted to platen displacement values. The experimental force versus displacement data for the specific tissue specimen being modeled were also read into MATLAB for comparison with the FE data.

The FE and experimental displacement data were then used to generate a list of evenly spaced displacement values that spanned the intersection of the two data sets. Two new sets of force values, one each from the experimental and the FE element model data, were then constructed by interpolating force values from the data sets at each displacement value in the newly-created list of displacement values. The result was an experimental force and an FE model force at identical displacement values, which allowed for a direct comparison of force differences between the physical experiment and the FE model. The use of the evenly spaced displacement values used for the interpolation equally weighted the curve fit in the higher strain and lower strain regions. A vector of the differences between the incremental experimental and FE model force values was then calculated and passed to the least squares nonlinear optimization function. The optimization function used the differential force values to calculate the sum of the squared error for the FE model run.

Following the initial FE run, small perturbations were made to each of the coefficients independently, while holding the other coefficient constant. These two coefficient updates were written into the FE input file, and the error calculation methodology was repeated to evaluate the influence of each coefficient on the error value. Based on the results of these preliminary incremental changes, the optimization function incrementally adjusted the individual Ogden coefficients in subsequent FE runs in order to reduce the error between experimental data and the FE model (Figure 13).

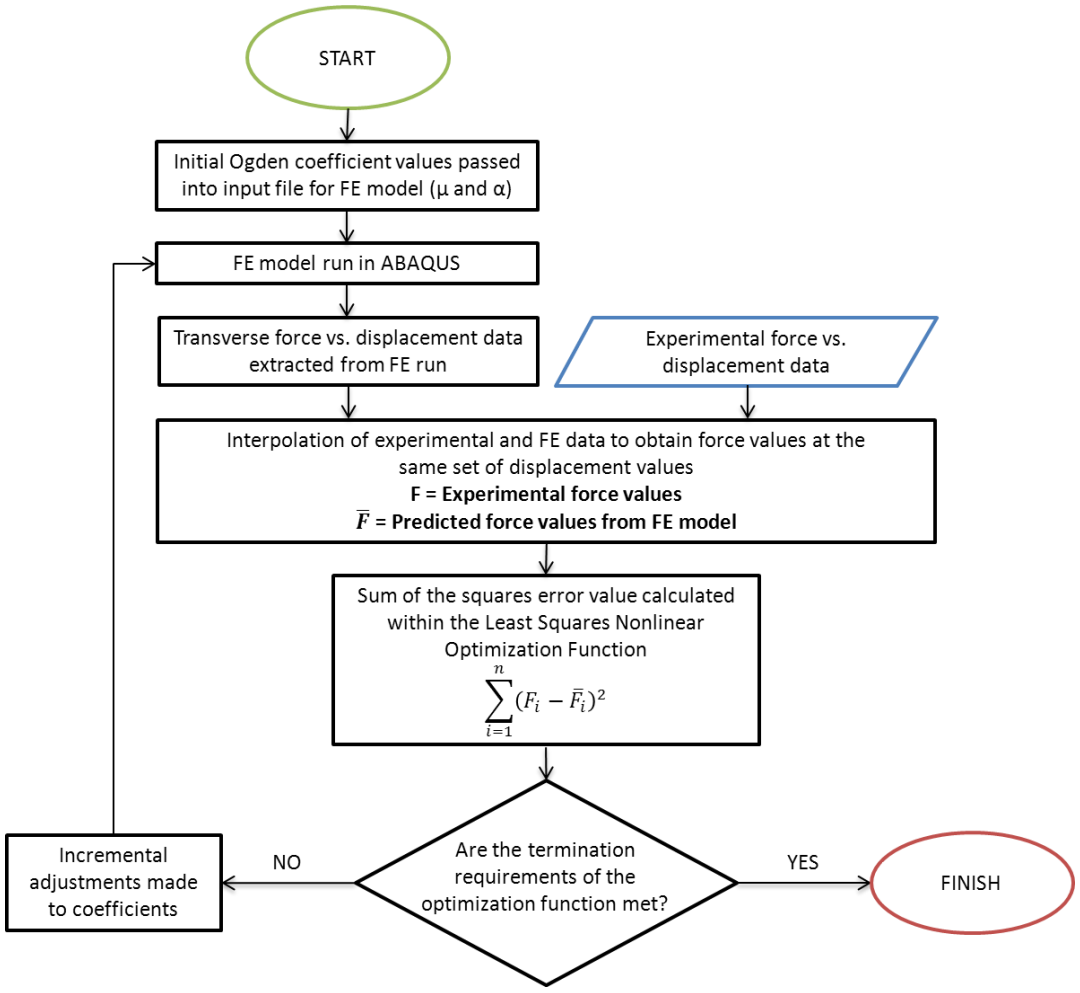


Figure 13. Flowchart for the steps of the least squares nonlinear optimization routine for obtaining a specimen-specific Ogden material property definition.

The optimization function terminated when one of the optimization function's two specified stopping criteria were met (Figure 14). For the first criterion, the optimization process ended when the norm of the iterative changes in the scaled (dimensionless) coefficient values decreased below a termination value of $1x10^{-4}$. This termination requirement was evaluated using the scaled coefficients at the $i^{th}$ iteration, as:

$$\sqrt{(\mu_{i-1} - \mu_i)^2 + (\alpha_{i-1} - \alpha_i)^2} < 1 \times 10^{-4}$$

The values of the μ and α coefficients were scaled within the optimization function to be of the same order of magnitude. This allowed for incremental changes made to the individual coefficients to have a comparable influence on the error value. The termination value of $1x10^{-4}$ was selected because it prevented excessive adjustments (less than 1% of the optimized coefficient values) from being made to the individual coefficients.

For the second stopping criterion, iterations ended when the changes in the sum of the squared error (SSE) of computational versus experimental forces relative to the SSE from the previous iteration decreased below the termination value of $1x10^{-4}$. This tolerance was evaluated at the $i^{th}$ iteration, as:

$$\frac{|SSE_{i-1} - SSE_i|}{(1 + |SSE_{i-1}|)} < 1 \times 10^{-4}$$

The SSE termination value was selected because it resulted in good curve fits to the experimental data, and prevented an excessive number of FE model iterations. Each run of the FE model took approximately 8 minutes, and the entire iterative optimization routine took approximately 3 hours per specimen to converge, depending on the choice of the initial coefficient values.

Following the completion of the optimization process for each specimen tested, Ogden coefficients were compared among the different flexor tendons and with the median nerve, using linear mixed-model analysis for repeated measures, with tendons

and nerve as the fixed-effect repeated measures factor. Based on estimates from this fitted model, Tukey's test was then performed to check for pairwise mean differences in Ogden coefficients between tendons and nerve.

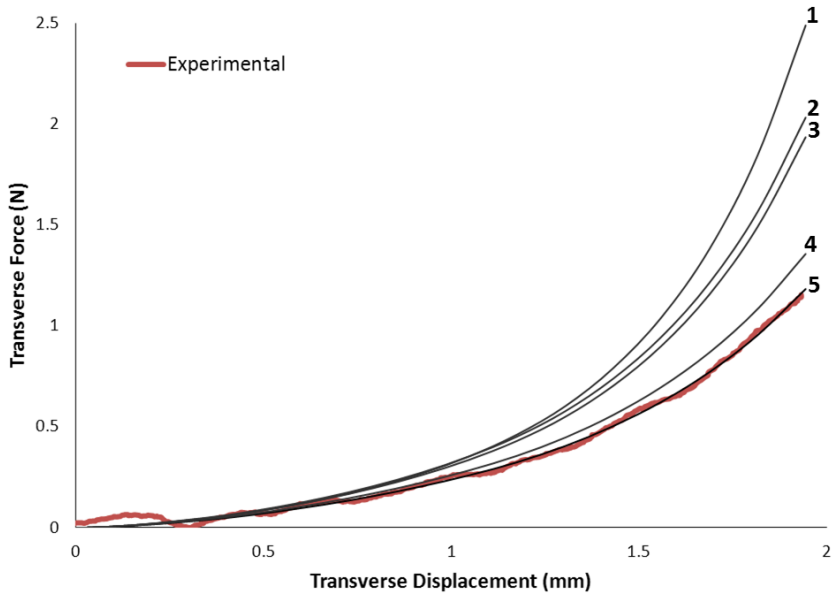


Figure 14. Transverse force versus displacement data for multiple iterations of the optimization routine. The experimental curve is represented by the red line, and the individual FE iterations are represented by the numbered black lines. Initial values for the Ogden coefficients ($\mu$ = 40 kPa and $\alpha$ = 12) were used in the first FE iteration (1). Small changes were made to each individual coefficient while holding the other fixed (2 & 3), to evaluate the error between the experimental and FE data associated with each individual coefficient. The optimization program then used this information to make further adjustments to both coefficients (4) before arriving at the final solution (5), here $\mu$ = 32.3 kPa and $\alpha$ = 9.4.

## Supplemental Experimentation

Prior to finalizing the convex platen design used during compression testing of the flexor tendons and nerve, a series of different platen geometries were investigated to ensure that accurate and reproducible material properties could be resolved from the

experimental data using reverse FE analysis. An earlier platen geometry for the transverse testing apparatus had been concave, and oriented horizontally along the tissue length (Ko, Rudert, and Brown 2007). The internal diameter of the concave platen used with each specimen had corresponded to the experimentally measured equivalent circular diameter. With this earlier arrangement, the platens had closed around the tissue specimens during transverse compression. Use of this platen geometry had been intended to allow for the straightforward calculation of tissue/platen contact area, in the intent of allowing for direct calculation of stress-strain curves from the experimental data.

To validate the use of those variable concave platen diameters, a single piece of 30A durometer rubber cording was compressed transversely using concave platens of three different sizes (3.25, 4.25 and 5.25 mm diameter). The purpose of this test was to ensure that comparable material property coefficients could be obtained for the test specimen, despite the use of the different platen geometries. Rubber cording was used in place of a cadaveric tissue specimen to avoid the introduction of experimental uncertainties related to the potentially irregular cross-sectional geometry of the tissue specimens, and to avoid variation in the specimen's compressive behavior between tests. To obtain material property definitions for the rubber cording, FE modeling and optimization was used (as discussed above). Rigid surfaces representative of each platen geometry were created in ABAQUS CAE. The rubber cording was modeled as a cylinder (Figure 15) and was ascribed a linearly elastic material property definition. The fitted Young's modulus values for the different rubber experiments varied significantly, based on the diameter of concave platens used. A modulus value of 0.3 MPa was obtained for the 5.25 mm diameter concave platens, whereas a value of 0.5 MPa was obtained for the 3.25 mm diameter platen.

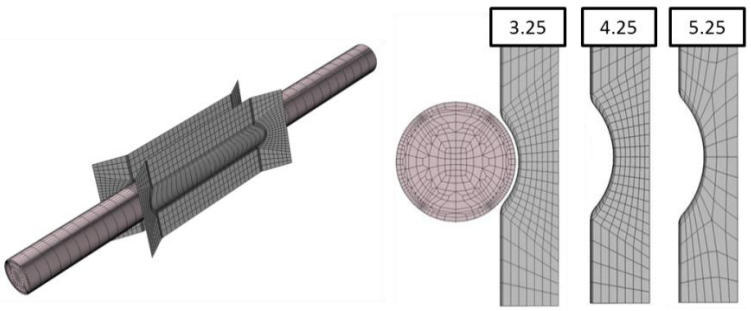


Figure 15. FE model with concave platens used for rubber cord validation (left). End-on views (right) of the 3.25 mm, 4.25 mm and 5.25 mm diameter platen sizes.

These large relative discrepancies in the fitted Young's modulus values presented a problem for accurately evaluating the transverse properties of the digital flexor tendons and the median nerve. Possible sources of error introduced with the use of these platens included fluid entrapment between the specimen and the concave platen surface, and premature contact between the specimen and the upper or lower edge of the platen.

Once reverse FE was adopted for resolving the material properties of the specimens, prior knowledge of the tissue/platen contact area throughout compression was no longer needed. Two new platen geometries were therefore tested using the rubber cording, one a flat platen geometry and the other a convex platen geometry (Figure 16). Similarly, linearly elastic modulus values were fitted to the experimental curves associated with the flat and convex platen geometries, using FE models that included the corresponding platen geometries. Good agreement was obtained between the two fitted Young's modulus values, with both platen geometries yielding Young's modulus values of approximately 0.7 MPa (Figure 17). The flat and convex platens eliminated any concern of fluid entrapment and/or premature contact between the edges of the platen and the tissue. The improved consistency in material property calculation led to the abandonment of the earlier concave platens. Of these two more

consistent geometries, the use of the convex platen was preferred over the flat geometry, in order to avoid uneven contact between the tissue and the edges of the flat surface, since physiologic tissues are not prismatic along their lengths. Additionally, the convex platen geometry avoided the introduction of any physiologically unrealistic sharp edges in the transverse compression experiments.

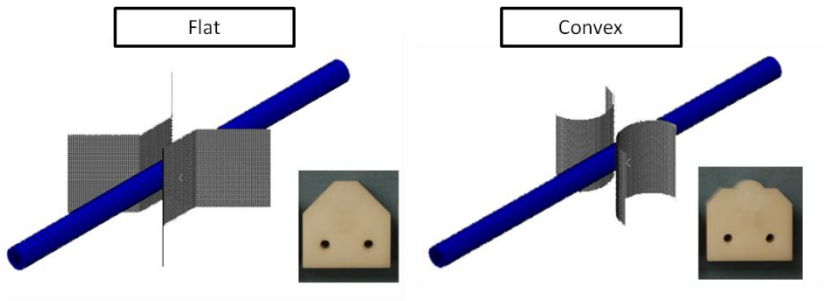


Figure 16. FE models with the flat (left) and convex (right) platen geometry used in the rubber cord validation. Inset on both models shows a single platen of each type used during physical testing.

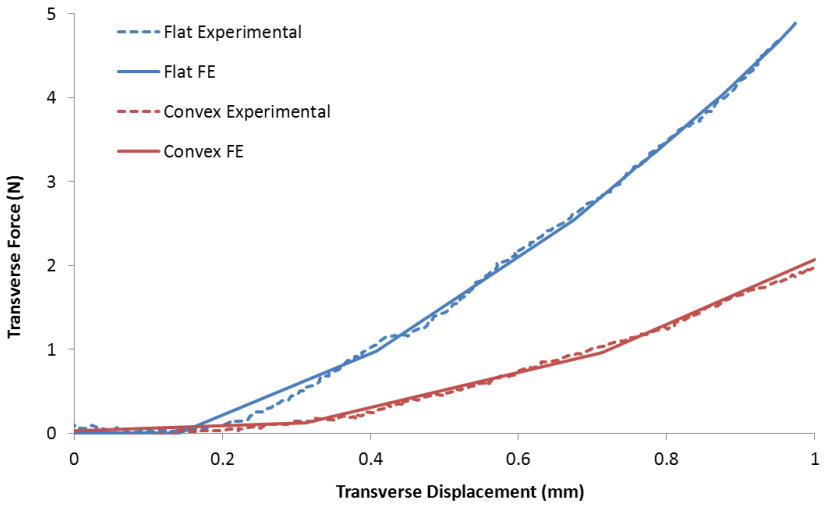


Figure 17. Linear elastic curve fits for the transverse compression of the rubber cording using the flat and convex platen geometry. With both platen geometries Young's modulus values of approximately 0.7 MPa were obtained.

Once reproducibility of material property measurements associated with platen geometry was confirmed, the recovery time required between each of a specimen's three replicate testing cycles was assessed to ensure complete reproducibility of compressive behavior between individual trials. For this testing, a single flexor tendon was compressed 40% of the measured major axis dimension, and the maximum force achieved during the compression test was recorded. After compression, the load was removed and the tissue was left in the serpentine clamps to recover in the heated fluid bath for ten minutes. An identical second compression test was then performed on the specimen, and again the peak compressive force value was recorded. The recovery time between subsequent compressive tests was then decreased to seven, five and three minutes. The original maximum compressive load for the tendon was recovered when recovery time intervals of at least five minutes were used, but the maximum compressive load decreased from its original value when only three minutes was allowed between replicate trials. To ensure complete repeatability, a seven-minute recovery time between replicate trials was selected for the flexor tendons. After similar sensitivity testing, a ten-minute recovery interval was determined to be adequate for the median nerve.

Repeatability between completely independent testing trials was also evaluated. First, the tissue specimen's major axis dimension was assessed, and a transverse compression test was performed on that specimen. The specimen was then completely removed from the serpentine clamps, allowed to recover for 7 minutes, and then re-gripped in the clamps. A second major axis length assessment was made, and another compression test was then performed. Minimal changes in the peak transverse compressive load (< 0.2 N) and major axis dimension (< 0.2 mm) were observed.

The natural, slightly flattened cross section of the tendons and nerve caused the tissues to rest in a preferred orientation within the open serpentine clamps. For the preponderance of the specimens tested, the major axis of the specimen's approximately

elliptical cross-section rested in the plane parallel the clamp opening. This orientation resulted in the specimens being compressed along their major axis. For completeness, the influence that the specimens' orientation within the serpentine clamps had on coefficient determination was evaluated. Compression testing was performed on two superficial specimens with their major axis oriented horizontal to the clamps openings. The specimens were then rotated 90 degrees from their preferred direction, and FE models were generated for both orientations. The average difference in the optimized coefficient values was 6.25% for μ and 5.5% for α. Owing to the small differences in material property behavior associated with transverse axis orientation, all specimens therefore were considered transversely isotropic.

The choice to compress the tissues to 40% of their major axis dimension was based on data from cadaveric and *in vivo* functionally loaded MRI scans of the carpal tunnel contents. As can be seen on axial magnetic resonance images of the unloaded carpal tunnel (Kunze et al. 2009; Goetz et al. 2010), the cross-sectional geometries of the tendons and median nerve do not match the elliptical profile that was observed for excised tissue specimens. In the present work, specimens were compressed transversely beginning from an excised, completely strain-free configuration, with a smoothly elliptical cross-sectional profile. To support the choice of the 40% compression, the "pre-strains" associated with tissue confinement within the tunnel were investigated. This was done in two cadaveric forearm specimens, by obtaining MR images of the flexor tendons and median nerve *in situ* within the carpal tunnel. The boundaries of the flexor tendons and median nerves were segmented from images within the carpal bounds using a purpose-developed semi-automated MATLAB program (Kunze et al. 2009) (Figure 18).

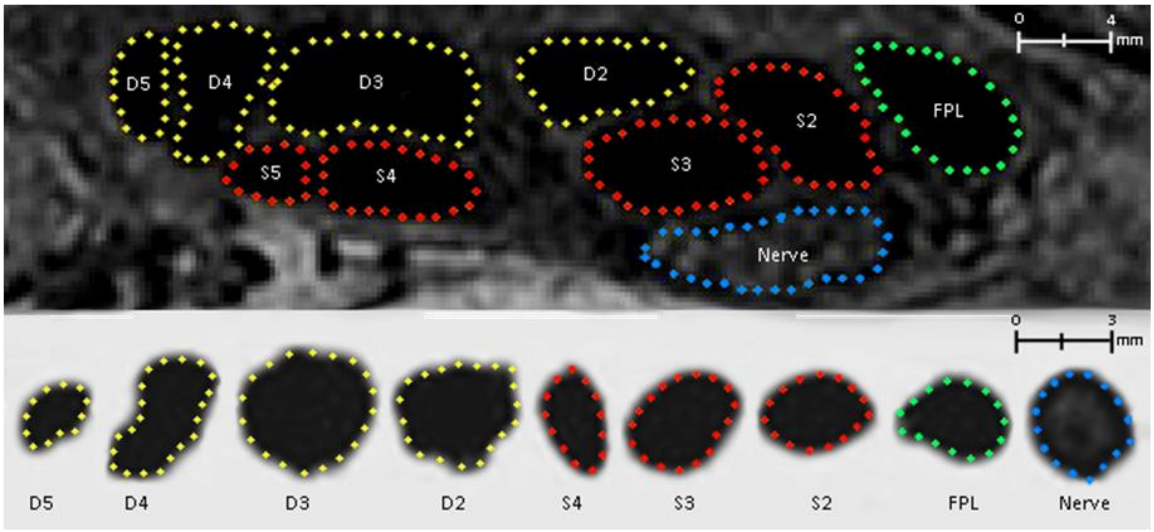


Figure 18. MR image of the tendons and nerve within a cadaveric carpal tunnel (top) and the same tissues excised and suspended in the saline bath (bottom). Note the rounder appearance of the tissue cross-section in the lower saline bath image.

The tissues were then physically dissected from the carpal tunnel and tied to a custom-designed tissue suspension apparatus placed in a saline filled bath. MR images of the tissues in the suspension apparatus were obtained and segmented using the same MATLAB program as was used for segmenting the *in situ* MR images. Corresponding slices were identified from the *in situ* cadaveric segmentation and the excised saline bath segmentations. This was done on a specimen-specific basis, using the analogous tunnel boundary locations identified on MR images and on each specimen during tissue dissection.

Flattening ratios were calculated to quantify the differences in bulk tissue shape between the excised and *in situ* segmentations. Flattening ratio was defined as the minor axis length of an ellipse fit to the tunnel boundary, divided by the major axis length of the fitted ellipse. Higher flattening ratios indicate a rounder profile, with a flattening ratio of 1 corresponding to a perfect circle. The flattening ratios of the excised tissues imaged in the saline bath were larger (i.e. rounder cross-sections) than

the *in* situ values (Table 1), indicating that the structures were appreciably "pre-strained" simply by being confined within the tunnel. Visual comparisons between the *in situ* and excised tissue segmentations were made by aligning major axis of each segmentation horizontally, and overlaying their centroids (Figure 19).

Table 1. Flattening ratios calculated for each tissue structure in corresponding *in situ* cadaveric and excised saline bath segmentation slices, with positive difference values indicating a rounder tissue shape in the excised segmentation than in the *in situ* segmentation.

| Tissue Structure | *In Situ* | Excised | Difference |
|---|---|---|---|
| Superficial Index | 0.42 | 0.52 | 0.10 |
| Superficial Middle | 0.67 | 0.75 | 0.08 |
| Superficial Ring | 0.75 | 0.71 | -0.04 |
| Deep Index | 0.29 | 0.43 | 0.14 |
| Deep Middle | 0.66 | 0.76 | 0.10 |
| Deep Ring | 0.53 | 0.80 | 0.27 |
| Deep Little | 0.42 | 0.80 | 0.38 |
| FPL | 0.53 | 0.73 | 0.20 |
| Median Nerve | 0.39 | 0.68 | 0.29 |

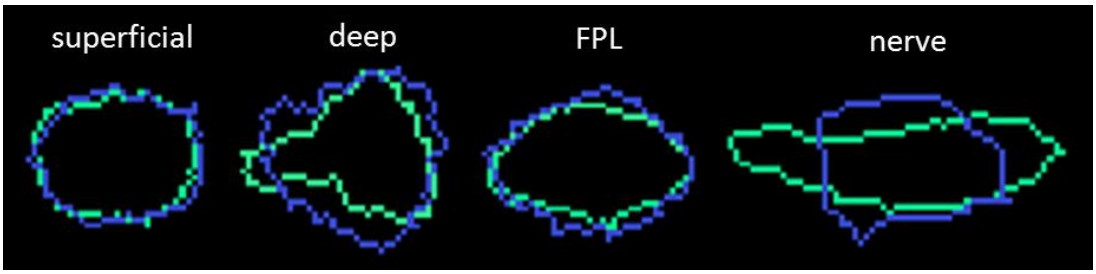


Figure 19. Corresponding slice overlays of the *in situ* cadaveric segmentations (green) and the excised tissue segmentations (blue) for illustrative superficial, deep, and FPL tendons, and the median nerve.

Given the appreciably lower flattening ratios associated with tissue confinement within the tunnel, unidirectional strain values were evaluated for the median nerve and flexor tendons based upon the *in situ* cadaveric relative to excised tissue segmentations. For the median nerve, this average strain value was 29%, and for the tendons this strain averaged 16% (range 3%-33%) (Main et al. 2011). Appreciable flattening of the flexor tendons and median nerve is associated with confinement in the tunnel, and further deformations can occur with functional movement. To investigate this, MR images of the carpal tunnel from individuals with a neutral wrist position in the absence of hand loading were compared to images acquired while the individuals were performing wrist flexion and isometric loading activities. Unidirectional strains on the tissues on the flexed and loaded scans were calculated relative to the neutral unloaded scans. The unidirectional strain measurements associated with wrist flexion averaged 17% for the nerve (range 6-28%) and 11% (range 1-29%) for the flexor tendons. The unidirectional strains associated with isometric hand loading averaged 11% for the nerve (range 3-26%) and 12% (range 0-36%) for the flexor tendons. The additive combination of the unidirectional strains associated with confinement within the tunnel and with wrist flexion/hand loading was approximately 40% for the median nerve and 28% for the flexor tendons. Thus, a major axis strain of 40% was selected to incorporate the full range of interest for constitutive characterization (Main et al. 2011).

## Supplemental Modeling

There were also several experimental and modeling assumptions in this project which may have influenced the material property values that were obtained. The smoothest experimental force/displacement curve from each specimen was used with the FE model optimization routine. To investigate errors associated with the particular curve choice, a comparative assessment was made between the different replicate force/displacement curves. The difference in load at a tissue's maximum compression

was calculated between each of the three replicate compressive test curves and mean of those three maximum forces. This analysis was performed for tissues from three randomly selected cadaveric specimens. The largest difference between the maximum force of any single curve and the respective tissue mean was 17%, although the average difference in load at maximum compression was only 3.2%. Formal comparisons of the similarity in curve shapes were also made, by calculating a sum-of-squares error value between the individual test curves and the average of those experimental curves. The error value was initially normalized to the maximum force taken up by the specimen, and was further normalized to the percent tissue strain applied to the specimen's major axis. The maximum observed variation between the curves was 3.6% of the total load per 1% of tissue strain. On average however, this value was much lower, typically less than 0.2% of the total load per 1% of tissue strain. Thus, it was concluded that the choice to use a single experimental curve over an average curve would not cause undue variation in the fitted material property coefficients.

In addition to the use of the smoothest force/displacement curve for analysis, the tendon and nerve specimens were modeled as perfectly prismatic along their lengths. However, the physical tendon and nerve specimens had moderately non-uniform cross-sectional areas along their lengths. To validate the use of the prismatic tissue modeling assumption, several parametric FE/optimization series were undertaken to determine plausible effects of these modeling assumptions on the calculated material properties.

Experimentally, the tissue cross-sectional area was determined by the measured equivalent circular diameter, for which the gauge openings were in 0.25 mm increments. This incremental sizing required that the true tissue cross sectional equivalent circular diameter be rounded to the nearest 0.25 mm diameter, which was inherently somewhat of an estimate. To minimize the effect of this estimation, cross-sectional area measurements were taken as close to the compression testing region as

possible. Further, the influence on the optimized Ogden coefficients associated with uncertainty of measured tissue diameter by ± 0.25 mm was evaluated. FE models with increased and decreased cross-sectional areas that corresponded to changes in the measured equivalent circular diameter by one gauge size (± 0.25 mm) were generated and run through the optimization routine to determine the Ogden coefficients. The coefficients from the size-adjusted models were compared to those obtained using the model with the original equivalent circular diameter measurement. The uncertainty associated with 0.25 mm increments of the measured equivalent circular diameter involved an uncertainty of roughly 10-12% in the $\mu$ coefficient, and of 1-2% in the $\alpha$ coefficient.

During the major axis assessment step of compression testing, the platens were driven together in 0.1 mm increments by the MTS actuator, and tissue contact was determined visually. Therefore, the influence of a ± 0.1 mm major axis dimension change on the resulting optimized $\mu$ and $\alpha$ coefficients was evaluated using methodology similar to that used to assess the influence of equivalent circular diameter measurements. Optimization results for tendons with major axes that differed by ± 0.1 mm from the initial assessment, but which had the same cross-sectional area, were compared for six different specimens. The average changed in the $\mu$ and $\alpha$ coefficients associated with the perturbation in the measured major axis was 16.1% and 6.6%, for $\mu$ and $\alpha$, respectively.

These various series of parametric FE investigations demonstrated that variability in Ogden coefficients associated with plausible uncertainty in the geometric and measurement assumptions was modest (< 16% for $\mu$ and < 7% for $\alpha$). Such minor increases or decreases in either the $\mu$ or $\alpha$ coefficient would result in coefficients well within the standard deviations found for specimen-to-specimen comparisons. Additionally, such plausible uncertainties in the average coefficients were much smaller

than the differences between properties of the median nerve and the digital flexor tendons (nerve μ 64% of tendon μ, nerve α 29% of tendon α).

## Results

The first-order Ogden hyperelastic model gave visually acceptable fits to the experimental data, using a minimal number of coefficients (Figure 20). The optimization routine yielded well-convergent Ogden coefficients for each individual flexor tendon and median nerve specimen (Table 2 and Table 3). The mean Ogden coefficients for the superficial (S) tendons were μ = 35.3 (95% CI: 26.7, 43.9) kPa and α = 8.7 (95% CI: 6.5, 10.9). These values did not differ significantly from the deep (D) tendons mean coefficients of μ = 39.4 (95% CI: 29.0, 49.8) kPa (p = 0.79) and α = 9.2 (95% CI: 7.2, 11.2) (p = 0.60). The FPL tendon had a mean μ coefficient of 24.9 (95% CI: 18.0, 31.8) kPa and α coefficient of 10.9 (95% CI: 7.7, 14.2). Compared to the superficial and deep tendons, the FPL tendon had a significantly smaller mean μ coefficient (p = 0.040 versus S; p = 0.011 versus D), but no significant difference in the mean α coefficient (p = 0.28 versus S; p = 0.47 versus D).

There were three outlier tendon specimens (S2, D2, and D3), all from the same cadaver forearm, that had extremely high values of μ, perhaps indicating some unappreciated pathology. Excluding these outlier values from the calculation gave mean μ coefficients of 33.1 (95% CI: 24.7, 41.4) kPa for superficial and 35.5 (95% CI: 28.6, 42.2) kPa for deep tendons. These means were only slightly smaller than the original values (which included all specimens), and these new means had a similar pattern of statistically significant difference compared to the FPL and the nerve.

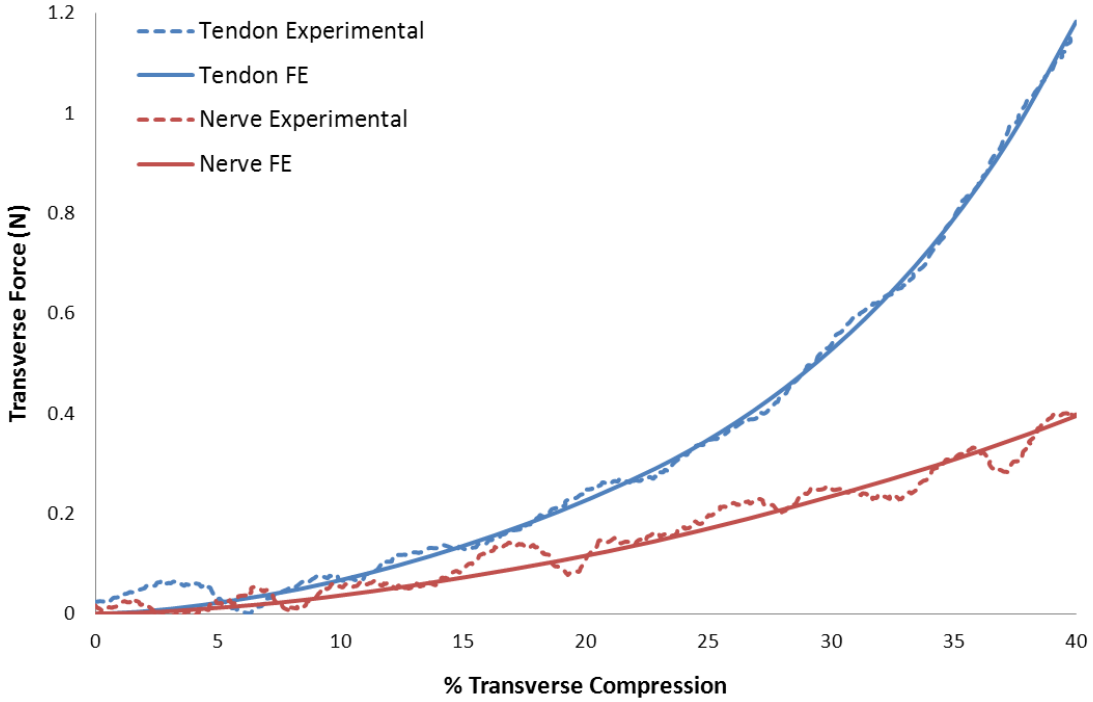


Figure 20. Experimental transverse compressive force versus percent transverse compression (dashed lines), and optimized FE results (solid lines), for illustrative digital flexor tendon and median nerve specimens. The flexor tendon shown (blue) is a D3 tendon with optimized coefficient values of $\mu$ = 32.3 kPa and $\alpha$ = 9.4. The median nerve (red) tissue has coefficient values of $\mu$ = 13.1 kPa and $\alpha$ = 2.0.

The nerve was less stiff than any of the flexor tendons (Figure 21). The mean nerve $\mu$ coefficient (12.9; 95% CI: 9.1, 16.8 kPa) was significantly smaller compared to the superficial ($p < 0.0001$), deep ($p < 0.0001$), or FPL ($p = 0.001$) tendons. The mean $\alpha$ coefficient of the nerve (6.5; 95% CI: 3.8, 9.1) was smaller than for any of the tendons, but it was found to be significantly different only from that of the FPL ($p = 0.033$ vs. FPL; $p = 0.25$ vs. S; $p = 0.27$ vs. D).

Table 2. Resulting Ogden μ coefficient (kPa) for each median nerve, flexor pollicis longus (FPL) tendon, superficial (S) tendon, and deep (D) tendon tested, with the average coefficient value across the 10 specimens given.

| Specimen # | S2 | S3 | S4 | D2 | D3 | D4 | D5 | Thumb | Nerve |
|---|---|---|---|---|---|---|---|---|---|
| 1 | 12.7 | 21.9 | 38.4 | 23.2 | 24.4 | 22.2 | 26.6 | 21.7 | 6.4 |
| 2 | 9.9 | 14.6 | 5.6 | 18.6 | 37.8 | 15.9 | 19.8 | 11.1 | 8.8 |
| 3 | 38.9 | 22.1 | 24.4 | 27.0 | 31.9 | 18.3 | 44.7 | 11.2 | 11.3 |
| 4 | 43.6 | 41.5 | 49.7 | 12.9 | 36.1 | 34.8 | 56.9 | 33.4 | 10.5 |
| 5 | 52.2 | 39.8 | 40.1 | 35.9 | 32.3 | 30.1 | 33.6 | 22.7 | 10.8 |
| 6 | 88.4 | 37.2 | 40.8 | 101.5 | 125.1 | 22.8 | 48.6 | 36.5 | 13.1 |
| 7 | 29.3 | 35.7 | 47.9 | 70.4 | 37.1 | 44.9 | 39.7 | 22.0 | 16.0 |
| 8 | 42.2 | 30.7 | 26.2 | 54.5 | 47.4 | 39.0 | 51.2 | 28.9 | 15.6 |
| 9 | 52.3 | 44.5 | 29.9 | 29.2 | 40.8 | 30.4 | 34.6 | 21.7 | 23.8 |
| 10 | 27.1 | 37.7 | 33.9 | 60.0 | 56.7 | 18.2 | 40.6 | 39.8 | 13.1 |
| **Average** | **42.7** | **33.8** | **33.2** | **45.6** | **49.5** | **28.3** | **41.1** | **25.3** | **13.7** |
| *St. Dev.* | 21.8 | 9.7 | 13.7 | 28.6 | 29.4 | 10.2 | 11.0 | 10.3 | 4.5 |

Table 3. Resulting Ogden α coefficient values for each median nerve, FPL tendon, S tendon, and D tendon, with the average coefficient value across the 10 specimens given.

| Specimen # | S2 | S3 | S4 | D2 | D3 | D4 | D5 | Thumb | Nerve |
|---|---|---|---|---|---|---|---|---|---|
| 1 | 2.6 | 5.2 | 7.6 | 6.7 | 2.2 | 2.7 | 3.7 | 3.0 | 1.7 |
| 2 | 4.1 | 8.8 | 13.3 | 5.6 | 6.8 | 8.2 | 11.0 | 15.4 | 2.9 |
| 3 | 5.3 | 3.7 | 4.3 | 6.3 | 7.9 | 2.5 | 11.7 | 9.2 | 2.4 |
| 4 | 9.8 | 5.1 | 6.3 | 9.0 | 6.9 | 2.4 | 10.0 | 5.3 | 6.2 |
| 5 | 9.1 | 8.1 | 7.5 | 17.9 | 9.4 | 9.5 | 8.6 | 10.8 | 10.4 |
| 6 | 8.8 | 8.2 | 7.0 | 19.1 | 1.8 | 17.3 | 1.8 | 13.8 | 2.0 |
| 7 | 9.9 | 10.8 | 12.4 | 11.6 | 6.7 | 13.1 | 10.9 | 13.0 | 5.7 |
| 8 | 12.6 | 12.2 | 15.0 | 13.7 | 12.8 | 7.2 | 10.5 | 16.4 | 4.9 |
| 9 | 11.6 | 14.9 | 17.0 | 14.6 | 15.0 | 13.6 | 17.2 | 13.7 | 15.2 |
| 10 | 3.2 | 7.8 | 9.4 | 13.9 | 7.7 | 3.4 | 6.8 | 8.7 | 13.2 |
| **Average** | **8.3** | **8.8** | **10.2** | **12.4** | **8.3** | **8.6** | **9.8** | **11.8** | **7.0** |
| *St. Dev.* | 3.3 | 3.4 | 4.4 | 4.7 | 3.8 | 5.3 | 4.1 | 3.6 | 4.8 |

The fingers are referred to numerically with index, middle, ring, and little fingers being numbered 2, 3, 4 and 5, respectively. The superficial little finger tendon (S5) was not tested due to its very small cross-section (< 2 mm diameter in most cases).

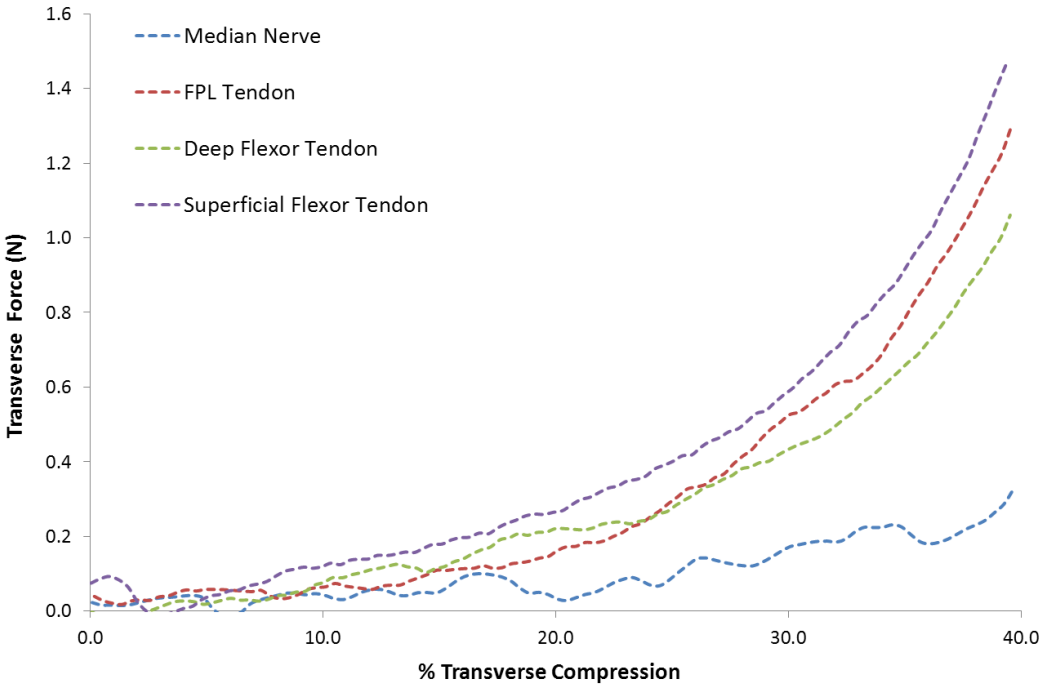


Figure 21. Plot of transverse force verses percent compression of the tissue major axis for a median nerve, FPL tendon, deep flexor tendon, and superficial flexor tendon specimen with behavior characteristic of the average μ and α coefficients for each strucutre.

## Discussion

The first-order Ogden hyperelastic material property definition provided a reasonable means to describe the nonlinear transverse compressive behavior of digital flexor tendons and median nerve, up to transverse compression of nominally 40% major axis strain. The tendons were, on average, approximately twice as stiff as the median nerve. There was no detectable variation in tissue diameter, visual appearance, or material properties associated with cadaveric specimen gender, age, weight, or height.

Somewhat surprisingly, there were only modest differences between the Ogden hyperelastic coefficients of the superficial versus deep digital flexor tendons, despite striking visually apparent differences morphologically (Figure 22). Specifically, the axially oriented fibers of the superficial tendons appeared effectively fused into a

continuum. In contrast, the deep tendons appeared as flatter, more composite structures, with individual fiber bundles evident between matrix connections. The transverse compressive behavior of these tissues is related to compression of axially tensioned fiber bundles, which in this work were subjected to identical axial loads. A possible explanation for the similarity in the transverse properties of the superficial and deep tendons, despite differences in their visual appearance, is that the transverse behavior is dominated by the tensioning of the axial fibers. The compressive properties determined may have been more a result of the bending of the identically tensioned fiber bundles, rather than the compression of the inter-bundle matrix material.

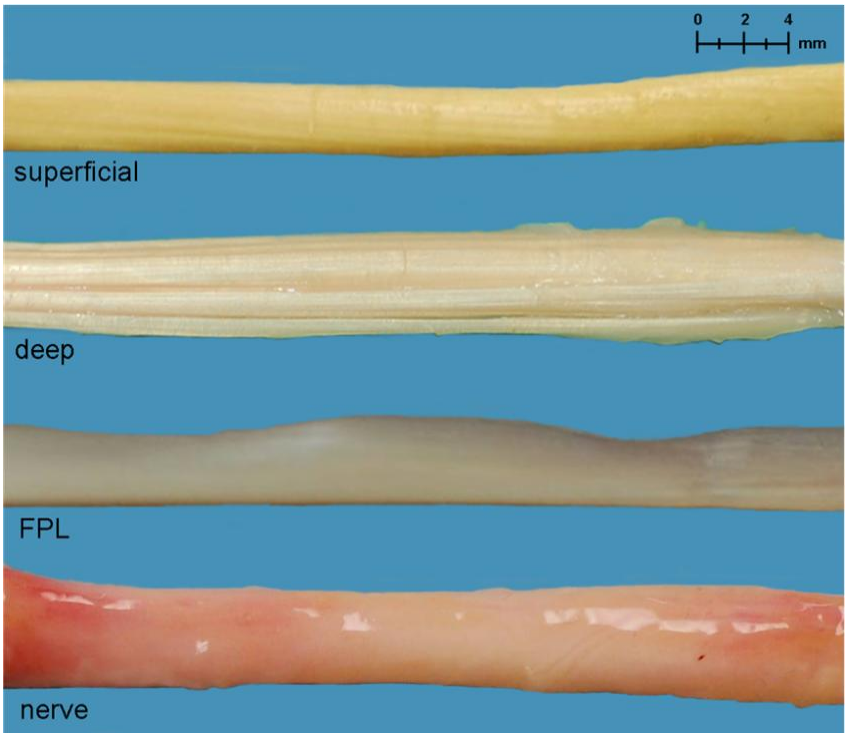


Figure 22. Illustrative appearance of superficial, deep, and FPL tendons, and the median nerve. Note the more homogenous appearance of the superficial tendon, versus the individual fiber bundles apparent in the deep tendon. The natural curvature of the FPL is apparent. There were no visible axial fiber bundles in the median nerve.

The FPL tendon had a lower mean μ coefficient and a higher mean α coefficient compared to the superficial and deep digital flexor tendons. *In situ*, the FPL tendon bends extensively around the carpal bounds as it run distally in the tunnel towards the thumb. When the FPL is excised from the hand, many of the natural bends and twists present in the tissue remain, indicating a fiber orientation that is not uniformly axially directed (Wilson and Hueston 1973). This could lead to FPL fibers that were not uniformly tensioned by the prescribed 15 N of axial load. The decreased low-strain transverse compressive stiffness of the FPL, as represented by the lower average μ coefficient, may be a result of lack of uniform tensioning. The higher α coefficient could be caused by the delayed load uptake by the more axially oriented fibers bundles located deeper in the tendon (Wilson and Hueston 1973).

There was more variation in the coefficients between the individual deep tendons than was observed between the individual superficial tendons, with the most variation seen in the μ coefficient and less in the α coefficient. The increased variability of the deep flexor tendon properties may have in part resulted in separating the interconnections linking some of the individual tendons (Kilbreath and Gandevia 1994). Sectioning of these interconnections between the deep tendons may have increased the variability in the overall cross-sectional profile of the tendons. This could have led to changes in the force/displacement behavior observed experimentally. The larger variability in coefficients may have also resulted from the challenge in identifying the precise instant of load uptake associated with the more composite structure. The deep tendon of the little finger visually appeared relatively similar to the superficial tendons, lacking the more characteristic composite structure associated with the deep tendons of the remaining fingers. The average value for the μ coefficient for the deep little finger tendon was closer to the averages observed for the superficial tendons.

All cadaveric specimens had been fresh-frozen prior to dissection and transverse tissue testing. Changes in collagen fibril composition and distribution, as well as

changes in the mechanical properties of tendons, can occur with freezing (Giannini et al. 2008; Clavert et al. 2001). To control for freeze/thaw effects, all specimens were thawed once, dissected, and then tested within a 24-hour window, to avoid the introduction of any additional freeze/thaw cycles. Standardization of one freeze/thaw for the tissues used in this study facilitated direct comparisons between the mechanical behavior of the tendons and nerves.

This portion of the project presents a combined experimental/computational assessment of the apparent transverse compressive properties of the digital flexor tendons and the median nerve, under a single axial load. As expected, the median nerve was found to be substantially less stiff than the neighboring digital flexor tendons. The hyperelastic coefficients determined can be implemented into FE models of the carpal tunnel, which in turn can be used to assess the contact stresses in the median nerve resulting from impingement by the surrounding digital flexor tendons. However, the properties determined are limited in that the transverse behavior is characterized for a single axial load. This loading may not be appropriate for FE models of all hand activities, where very different tendon loads could be expected.

# CHAPTER IV: AXIAL TENSILE AND TRANSVERSE COMPRESSIVE PROPERTIES OF DIGITAL FLEXOR TENDONS AND THE MEDIAN NERVE

The hyperelastic Ogden transverse material properties determined in Chapter 3 are specific to flexor tendons subjected to 15 N of axial tensile load and median nerves subjected to 5 N of axial tensile load. However, physiologic axial tension in the digital flexor tendons varies widely with hand position, load and activity. The median nerve is also subjected to variable axial tensioning from frictional forces created by the gliding of the differentially tensioned neighboring tendons. The specifics of how frictional loading of the median nerve may change during specific hand activities remains relatively unknown. However, it is reasonable to hypothesize that median nerve axial loads vary widely with hand position, loading, and activity. The effects of the axial tensile load borne by each tissue structure may influence its transverse compressive behavior. During the previously described transverse compression testing of the deep and superficial tendons, little difference was observed between the optimized Ogden coefficients, despite the two tissue types having very different visual appearances. It was thought that the similarities in their transverse compressive behavior were caused by the equal tensioning of the axially oriented fibers. Thus, increasing axial tension applied to the fibers could potentially influence the compressive behavior of each tissue.

To examine the influence of variable axial tensioning on the transverse behavior of the digital flexor tendons, a series of transverse compression tests were performed on a tendon specimen while that specimen was subjected to increasing axial tensile loads. Axial loads ranging from 3 N up to 30 N were applied. It was found that the transverse stiffness of the tissue increased in association with the increase in axial load (Figure 23), demonstrating interdependence of the axial tensile and transverse compressive properties of the tissue. To further evaluate this finding, FE models utilizing a fiber-reinforced nonlinear material property definition were generated, which

allowed for describing both axial and transverse behavior using a single material property definition. Implementation of this more advanced material property definition involved an appreciable increase in the algorithmic complexity of the optimization routine, because the material property definition utilized three material coefficients, and because the optimization routine had to accommodate the influence of both axial and transverse tissue behavior in order to optimize the appropriate coefficients.

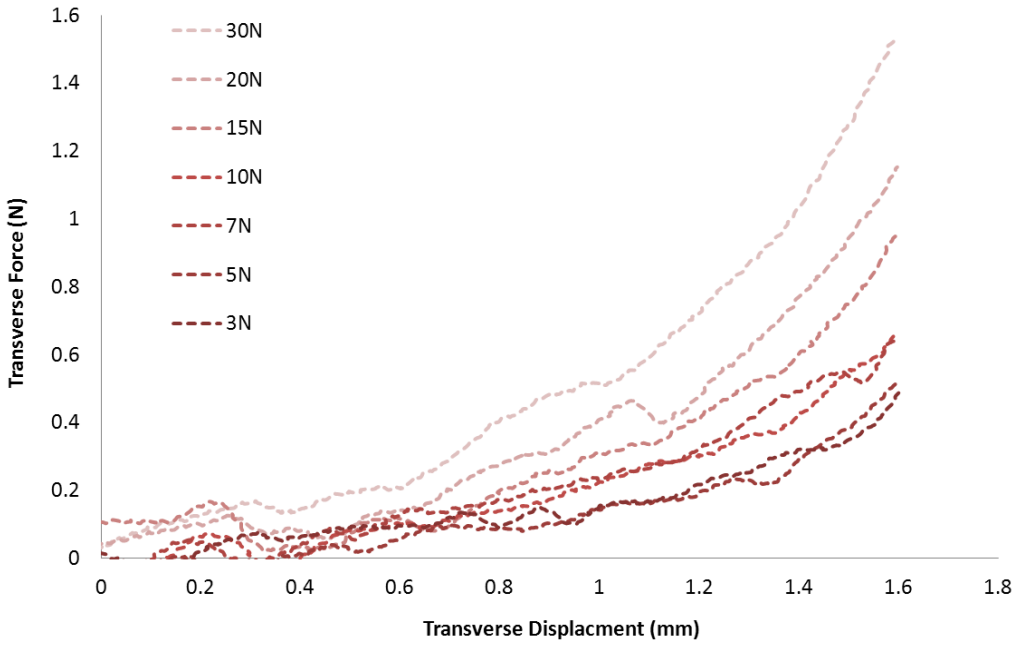


Figure 23. Transverse force versus compression graph for the tendon specimen tested under axial tensile loads ranging from 3 N (darkest curve) up to 30 N (lightest curve). The transverse stiffness of the tissue increased with increasing axial tensioning.

## Experimental Methodology

In order to develop the fiber-reinforced material property definition, axial extension data for the digital flexor tendons and the median nerve at the tension values of interest had to be collected. These data were collected on a different day than the

transverse compression data because acquiring the axial data required modification to the transverse compression device. Axial extension data were collected from three randomly selected cadaver specimens (all nine tendons and the median nerve from each) previously used for transverse testing (a 37 year old male, a 50 year old female, and a 64 year old male). To replicate the testing conditions that were present during the transverse compression data collection for the subsequent axial tension testing, cylindrical Delrin collars of the same size as those used during transverse testing were again applied to the each tissue specimen. To track axial extension during tensile testing, two tantalum beads approximately 1.0 mm in diameter were super-glued to the tissue surface, 15 mm to 25 mm apart and centered between the collars.

Tissue specimens were mounted in a modified version of the testing apparatus that had been used for transverse compression data collection. The "floating" platen/load cell construct was exchanged for a clear plastic platform mounted on a metal rod attached to the side of the heated fluid bath. The platform provided stable support for a camera centered above tissue specimens which were held in the serpentine clamps (Figure 24). The digital flexor tendons were allowed to equilibrate in the heated fluid for 7 minutes, and the median nerve was allowed to equilibrate in the heated fluid bath for 10 minutes, prior to commencing axial testing.

For tests of the flexor tendons, axial tensile load was applied using the same pneumatic cylinder, precision regulator, and pressure gauge as had been used during transverse compression testing. For the tests of the median nerve, a more sensitive regulator (Type 700 High Flow Pressure Regulator, Control Air Inc., Amherst, NH, USA) and pressure gauge (MGA-30, SSI Technologies, Inc., Janesville, WI, USA) with lower controllable limits was used. Each test consisted of axial load application over a period of approximately 30 seconds. Tests of the flexor tendons used approximately 3 N loading increments beginning from the lowest controllable limit of the regulator (approximately 1.5 N) up to 50 N. Photographs were acquired at each loading

increment, and the specific axial load being applied was recorded. For the median nerve tests, loading started at approximately 0.5 N, and loading increments of 1.5 N were used up to a maximum load of 20 N.

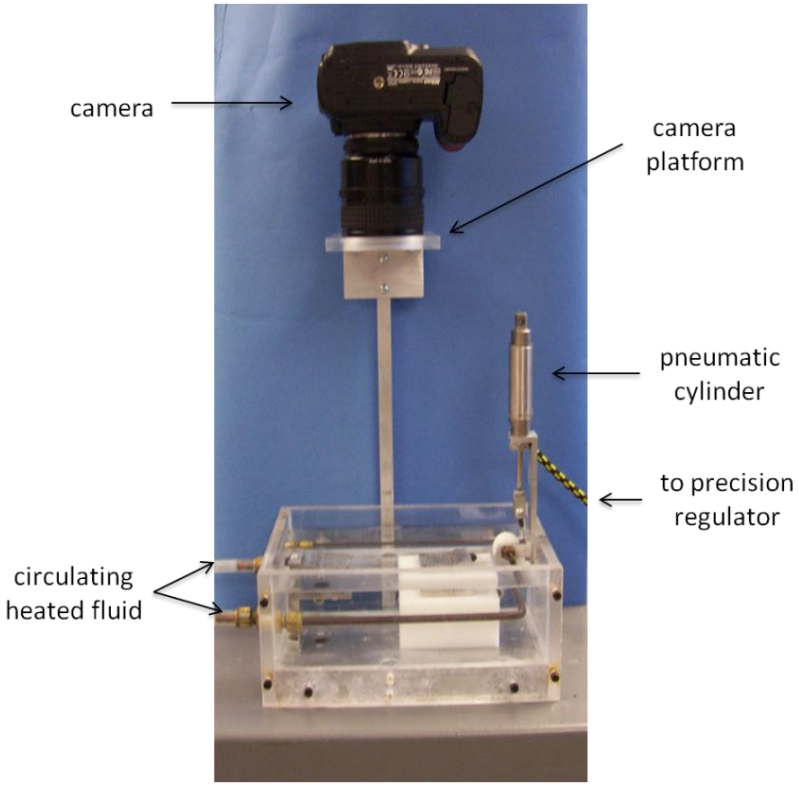


Figure 24. Modified testing apparatus with camera mounted above the tissue specimen for image acquisition during axial tensioning.

During axial extension data collection, photographs of the tissue specimens under zero axial load were not acquired. Without axial tensioning, the tendon and nerve specimens were slack and did not rest perfectly straight between the serpentine clamps. Rather, these slack tissues adopted a curved and slighted twisted appearance within the testing device. As a result, any distance measurements made between the bead markers with the tissue specimens under zero axial tensioning would have yielded

an inaccurate initial inter-bead distance measurement. Several attempts were made to manually apply a very small straightening load to remove the slack from each tissue specimen. Ideally, photographs that were acquired with the tissue specimen under this straightening load would have provided an accurate inter-bead gauge distance measurement, thus allowing axial strain to be calculated directly from the experimental data. However, the manually applied straightening load caused tissue deformations larger than those measured when the lowest axial load was applied through the regulator. As a result, the use of inter-bead distance measurements made under the manual straightening load as an inter-bead datum gauge length gave invalid strain values at subsequently applied axial force values. Thus, inter-bead distance measurements were only made on photographs in the sequence commencing from regulator application of the lowest applied axial load.

Three replicate data sets were collected for each specimen, with a 7-minute recovery period between tests of the flexor tendons, and a 10-minute recovery period between tests of the median nerve. To obtain physical measurements from each sequence of extension photographs, a photograph of a 15 cm ruler placed in the serpentine clamps was obtained prior to each testing session.

A correction was applied to the recorded axial loading values to account for the frictional force needed to drag the serpentine clamp across its Delrin block base in the fluid bath. This correction value was obtained by loading the empty serpentine clamp using the more sensitive regulator (same as that used to tension the median nerve). Increasing axial loads were applied to the empty clamp until movement of the clamp was observed. This measured correction value was 0.553 N, which was subsequently subtracted from all of the axial loading data that were collected during testing.

A semi-automated MATLAB routine was then used to evaluate the photographic sequences collected during axial extension testing and to measure changes in the inter-bead distance under the applied axial loads. Prior to the MATLAB analysis steps,

template images of the beads that were attached to the tendon or nerve surface were generated using ImageJ software (open source National Institutes of Health, Bethesda, MD, USA). The first photograph from the first of a specimen's three loading photograph sequences was used to generate the template images. In Image J, the bead region was manually defined using the oval selection tool (Figure 25). The major and minor axis lengths of the oval selection defined the dimensions of the template crop box. Template images were generated for both the left and right bead markers.

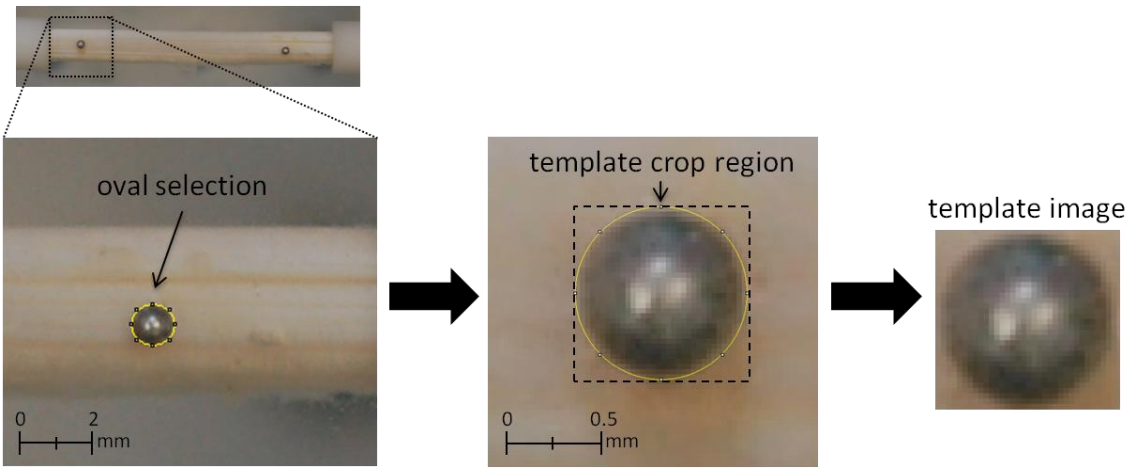


Figure 25. ImageJ oval section tool was used to define the bead region (left). Template crop region was defined using the major and minor axis lengths of the defined bead region (middle). Region was then cropped to create the template image (right).

After template image generation, analysis of the given specimen's three axial extension photograph sequences was carried out using code developed in MATLAB. For each of the three sequences, the file for the first photograph in the sequence was opened, and a reduced search region was defined by manually selecting a crop region enclosing the left bead (Figure 26). This smaller search region was used to reduce the time needed to automatically identify the bead marker in each subsequent photograph

of the sequence. The template image for the working photograph sequence was loaded into MATLAB, and both the template and the cropped search region images were converted to grayscale.

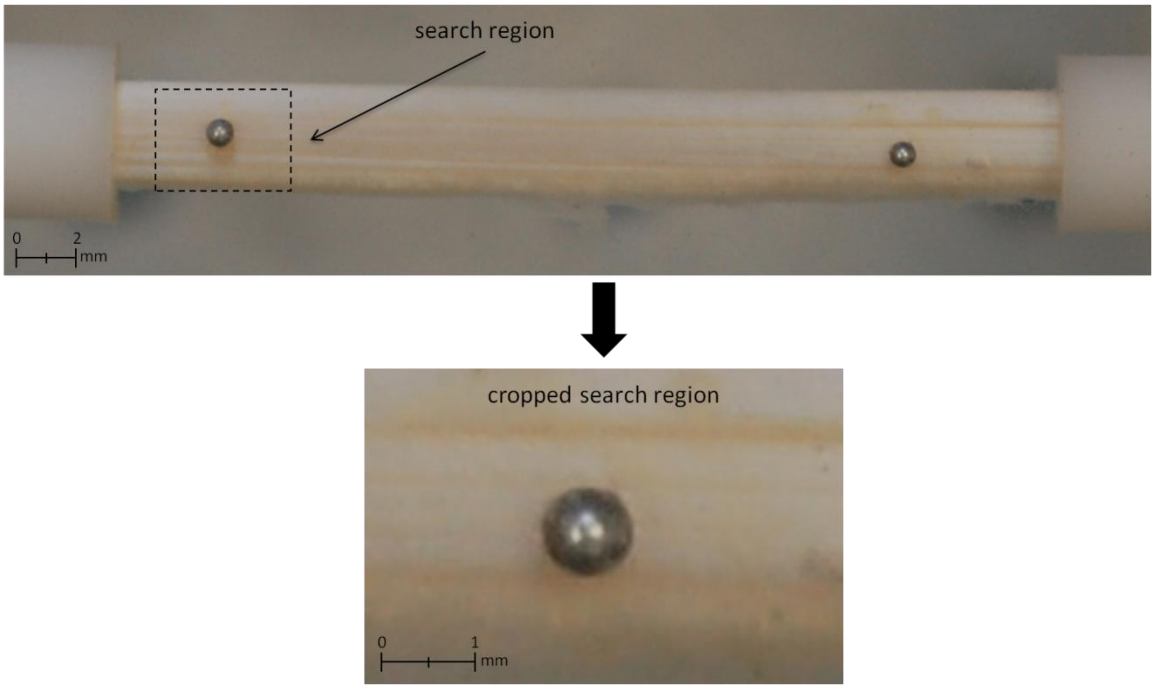


Figure 26. A search region was defined enclosing the left bead marker on the first photograph of the loading sequence (top). This region was cropped from the photograph and used as the search region image (bottom).

A template matching function was then used to detect the location of the template image within the search region image. The template matching function used two dimensional convolution to generate a matrix of correlation values equal in size to the cropped search region image (Figure 27). Correlation values ranged between 0 and 1 with higher values indicating better agreement between the two images. A minimum correlation threshold of 0.75 was prescribed for the template matching function. The function returned an error if the maximum correlation value from the convolution

matrix was less than this threshold value, indicating that the template image was not detected within the search region image. If no error occurred, the location within the convolution matrix with the maximum correlation value was identified as the position of the left bead. This same process was repeated with the right bead marker on the tissue, using its respective template image, and the distance (in pixels) between the two bead positions was calculated.

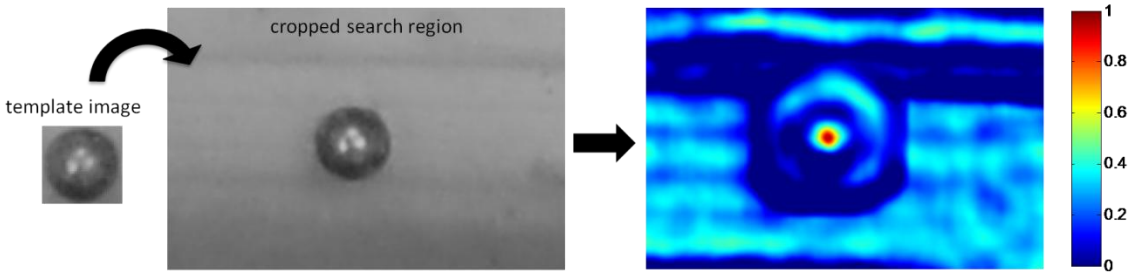


Figure 27. Bead locations are identified using a template matching function. The location of the grayscale template image within a grayscale image of the cropped search region was found using convolution (left). A convolution matrix of correlation values (right) is generated, and the location within the matrix with the highest correlation value was selected as the bead position.

Search regions defined manually on the first photograph were automatically propagated to each subsequent photograph in the loading sequence, and the bead identification procedure was repeated for all photographs comprising the loading sequence. Changes in the distance between the beads over the course of the photographic loading sequence provided a measure of tissue extension under increasing axial loads.

Photographs of the ruler which were obtained during each of the testing sessions were then used to convert the inter-bead distance measurements from pixels into metric values. After calculation of inter-bead distance for each photograph in a

loading sequence, the corresponding ruler photograph was loaded into MATLAB. This photograph was cropped so that only one centimeter of the ruler was in the field of view. A black and white image of the cropped ruler was created from the color image using a global threshold level computed by minimizing the variance within both the black and white pixels. A single ruler hash mark was manually cropped from the binary ruler image, and the centroid of that hash mark was found. A second hash mark, 5 mm away, was selected in the same manner, and the distance between the centroids of the two hash marks was computed. A scaling factor was created using the calculated number of pixels and the known physical distance between the two hash marks. This scaling factor was then used to convert the inter-bead distance measurements (tissue axial extension measurements) from pixels into millimeters.

An average axial force/extension curve was generated for each specimen using the specimen's three replicate tensile tests. Axial force values and the corresponding inter-bead distance measurements for each replicate were read into MATLAB. A vector of evenly-spaced force values was generated in 1 N increments for tendons and in 0.5 N increments for the median nerve. The vector started from the minimum axial force measurement in all three data sets and ended at the maximum axial force measurement in all three data sets. For each of the three replicate tests, inter-bead distance measurements were interpolated at each tensile force value. For each force increment, an average inter-bead distance was found using the three interpolated inter-bead distance values. The resulting average force versus inter-bead distance measurements were used in FE optimization to characterize the combined axial tensile and transverse compressive behaviors of the flexor tendons and median nerves.

## Finite Element Modeling

Using a methodology comparable to that described in Chapter III to obtain transverse compressive material properties at one axial load, optimization of specimen-

specific FE models was used to combine the axial and transverse tissue behavior into a single material property definition. A reverse FE method was employed using a half-tissue model very similar to that used in Chapter III. The rigid body platen mesh created in ABAQUS CAE for the single axial load transverse property optimization was used without modifications. Symmetric half-tissue models of the tendons and nerve were recreated with their elliptical cross-sections defined by the major and minor axis measurements taken previously during transverse testing. Tissue specimen meshes were again generated using TrueGrid, but with the mesh substantially refined within the platen contact region, relative to the previous model. The additional mesh refinement was needed for the process of identifying nodes within the model which corresponded to the physical locations of the experimental bead markers.

During axial testing, valid inter-bead gauge distance measurements for unloaded (0 N) tissue specimens could not be obtained, for the reason noted above. Without an accurate inter-bead gauge length, axial tissue strains could not be calculated from the experimental data, or scaled up from an inter-bead strain to a strain over the whole tissue specimen. Thus, data about model extension under the applied axial loads had to be monitored at nodes within the model representing the left and right bead markers. During mesh development, a 1-node set representing the left bead was defined using a node on the upper-most edge of the mesh towards the fixed end of the tissue specimen. The distance between the center of the increased mesh refinement region and the left bead node was equal to the experimentally measured bead distance at the lowest applied axial load. Unfortunately, the right node could not be selected until after the lowest applied axial load had been applied to the model. A second node set of candidate right bead nodes was created from all nodes along the upper edge of the mesh in the increased mesh refinement region (Figure 28).

To accommodate the application of axial loads within the FE model, one end of the mesh (stationary end) was constrained against axial displacement (z-direction)

during the analysis, while the nodes on the opposite end of the tissue were prescribed as a rigid surface. Axial loading was applied to the rigid end of the model using a reference node located at the center of the rigid moving end of the tissue. The nodes along the plane of symmetry in the tissue mesh were held fixed in the x direction. Contact pairs were again designated between the surface of the tissue specimen mesh and the platen.

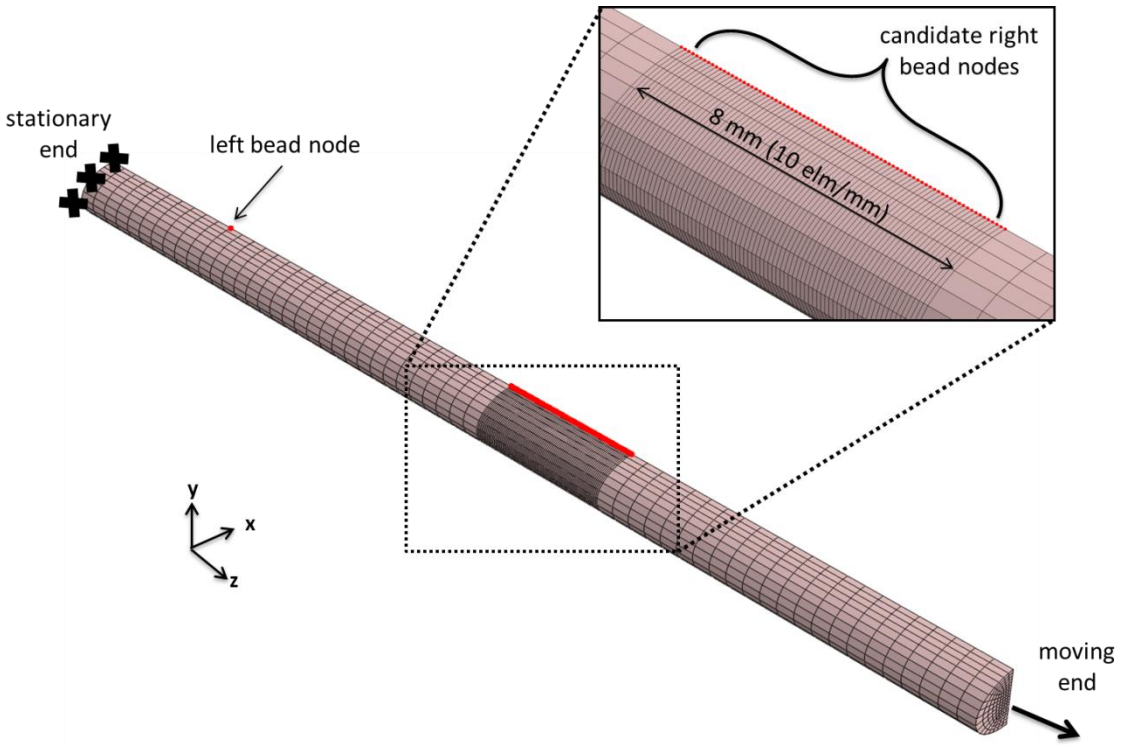


Figure 28. Tissue mesh with left bead node and node set of candidate right bead nodes highlighted in red.

In the first FE model step, an axial load was applied to the rigid body reference node on the tissue mesh, which was half (to account for the half-tissue mode) of the magnitude of the lowest experimentally applied load. In the subsequent step, the applied axial load was increased to half of the maximum load that was applied

experimentally. During the third step, the axial load was reduced to 7.5 N for the tendon half model (or 15 N overall) or 2.5 N for the nerve half model (or 5 N overall) to simulate the axial tensile load that had been applied to the tissue specimens during previous transverse compression testing. During these axial extension steps, the coordinates of the left bead node and the coordinates of each node in the candidate right bead node set were written to the FE model output file. Once the model was appropriately loaded with the axial load present while transverse compression was applied, the final FE step was to apply the 40% compression of the major-axis length in the same manner as it was modeled in the transverse compression-only FE models. As in the transverse compression-only model, the rigid body reference node on the platen was used to collect reaction force data during transverse compression.

In contrast to the first-order Ogden material property definition used to describe the transverse compression-only tissue behavior, the combined axial and transverse tissue behavior was modeled with a fiber-reinforced anisotropic hyperelastic material property definition available in ABAQUS. This particular constitutive model was proposed by Holzapfel, et al. (2000) and was initially used to model arterial wall mechanics. The required material property coefficients describe both the fiber and the matrix contributions to mechanical behavior. For this constitutive model, strain energy U is expressed using strain invariants (I) as:

$$U = C_{10}(\bar{I}_1 - 3) + \frac{k_1}{2k_2}\sum_{\alpha=1}^{N}\{\exp[k_2\langle\bar{E}_\alpha\rangle^2] - 1\}$$

$$with,\ \ \bar{E}_\alpha \overset{\text{def}}{=} \kappa(\bar{I}_1 - 3) + (1 - 3\kappa)(\bar{I}_{4(\alpha\alpha)} - 1)$$

The term κ is a fiber dispersion parameter with possible values between 0 for parallel fibers and 1/3 for randomly dispersed fibers. For this study, κ was set to 0 and the fibers were oriented along the axial direction of the tissue. The constitutive model has two coefficients that govern the properties for the fibers: $k_1$ and $k_2$. Parameter $k_1$

has units of stress, while $k_2$ is a dimensionless parameter. The matrix material is modeled as an incompressible, isotropic, Neo-Hookean material which is characterized by the coefficient $C_{10}$ (Gasser, Ogden, and Holzapfel 2006).

## Optimization Routine

Similar to the optimization routine used to fit the two Ogden coefficients in Chapter III, the anisotropic hyperelastic optimization routine utilized a least squares nonlinear optimization function. This optimization routine was used to find the three anisotropic hyperelastic coefficients ($k_1$, $k_2$, and $C_{10}$) that best replicated both the experimental transverse compressive and experimental axial extension behaviors in the FE model. Initial coefficient values were selected for the two material constants that governed the axial behavior ($k_1$ and $k_2$), as well as the single constant that represented the behavior of the matrix material ($C_{10}$) (Figure 29). These initial values were used in the first run of the FE model of axial extension followed by transverse compression. Upon completion of that first FE run, time step data and coordinates of the left bead node and candidate right bead nodes were extracted from the output file to be used in the axial extension component of the optimization process. Time step data and reaction force data from the rigid reference node on the platen were also extracted from the output file during transverse compression step of the FE run, for use with the transverse compression component of the optimization routine.

Starting with the axial component of the optimization routine, the time step data extracted from the output file were converted to tensile force values using the known applied force in the axial extension steps. For each applied axial load, the extracted nodal coordinates for the left bead node and the candidate right bead nodes were available for inter-bead distance calculations. The average experimental inter-bead distances and axial force data were also read in to MATLAB.

At the end of the first axial extension step, the lowest experimentally measured axial load had been applied to the model. It was at this axial load that the first experimental inter-bead distance measurement was available. Thus, at that time point the correct right bead node within the FE model had to be determined. To accomplish this, the distance between each candidate right bead node and the single left bead node was calculated using the nodal coordinates previously made available at the lowest applied axial load. The inter-bead distances determined from the FE model were compared to the experimental inter-bead distance measurement taken at the same axial load. The candidate right bead node whose distance from the left bead node was most similar to the experimental inter-bead distance was selected to be followed in the subsequent optimization analysis.

Following the second axial extension step, the highest axial tensile load applied experimentally was applied to the model. Inter-bead distance measurements between the left bead node and the selected right bead node were determined at each loading increment of this second step. The result was a full set of inter-bead distance measurements and corresponding axial force values from the FE model. These values were then used for comparison with the experimental axial force and inter-bead distance data.

The final step in the axial component of the optimization process was to create a set of error values. Using methods described previously, axial force values from the FE model and axial force values from the experimental data were interpolated to obtain tensile force values at one hundred evenly spaced inter-bead displacement values. The difference between the FE and experimental axial tensile force values at each inter-bead distance was calculated, and this set of values was normalized by the maximum experimental force applied to the specimen. The result was a set of error values representing the difference between the experimental and FE model prediction of the axial tensile behavior of the specimen.

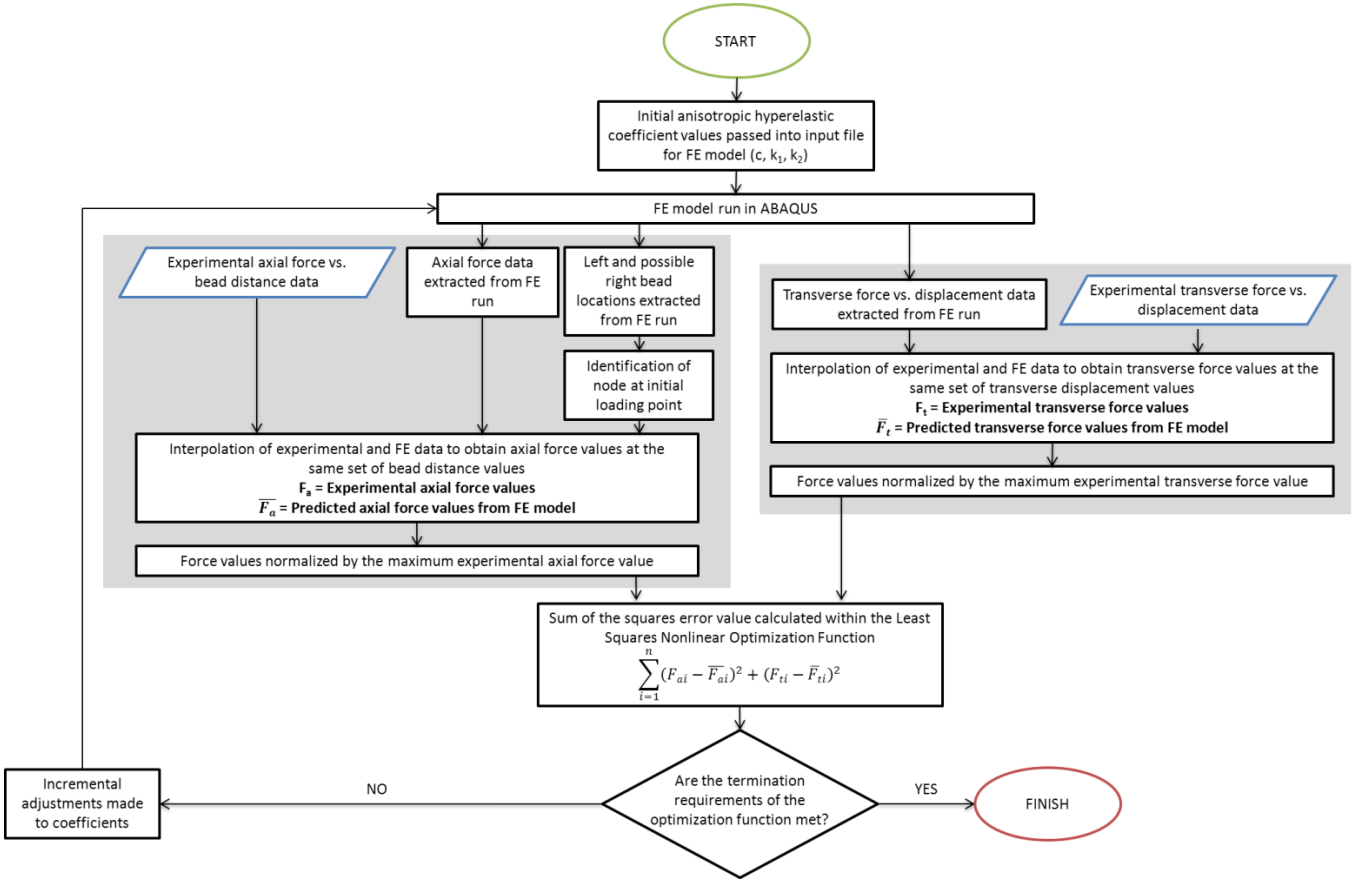


Figure 29. Flowchart detailing the steps of the anisotropic hyperelastic optimization routine used to combine axial tensile and transverse compressive behavior of the digital flexor tendons and median nerve into a single material property definition.

The transverse compression aspect of the optimization process proceeded in a similar manner to what was used for the Ogden optimization routine. The reaction force data from the reference node on the platen were used along with the time step data extracted from the FE model. The time step data were converted to displacement values using the known displacement applied to the platen. An average experimental transverse force/displacement curve for the particular specimen was also read into MATLAB. Compressive force values from the experimental data and from the FE model were interpolated at one hundred evenly spaced transverse displacement values. The difference between the transverse experimental and transverse FE forces values was calculated at each displacement value, and this set of differences was normalized by the maximum experimental transverse compressive force. The normalized set of error values from the transverse compression step represented the difference between experimental and FE model transverse compression data.

A combined set of error values was created adding together the normalized axial error values and the normalized transverse error values. By creating an equal number (100) of normalized differential force values from the axial extension and transverse compression steps, the error value equally weighted the axial and transverse behavior. The combined axial/transverse set of error values was then passed to the least squares nonlinear optimization function, where the sum of the squared error of the combined axial/transverse set of error values was calculated.

Small changes were then made to each of the material coefficients ($k_1$, $k_2$, and $C_{10}$) independently in three successive FE model runs. The influence that modifying each coefficient had on the sum of the squared error value was examined. After the three FE model runs to investigate the independent effects of each coefficient, the optimization function proceeded to make iterative changes to all three coefficients in additional FE runs until a converged solution was found. The termination criteria used

with this anisotropic model were the same as those used for the Ogden material property optimization because a similar coefficient scaling scheme was used.

Each FE model run required approximately 30 minutes to complete the series of axial tension and compression steps. As a result of the increased FE run times associated with the more complex model, the optimization routine required approximately 24 hours to converge to a solution. This was a much longer process compared to the 3 hours needed to reach a converged solution with the Ogden optimization routine. The three anisotropic hyperelastic coefficients ($k_1$, $k_2$, and $C_{10}$) obtained during the optimization routine were compared among the different flexor tendons and the median nerve.

## Results

The fiber-reinforced anisotropic hyperelastic material property definition provided reasonable fits of the axial tensile and transverse compressive experimental data (Figure 30). The optimization routine converged to unique values for the majority of the digital flexor tendon and median nerve specimens. The average transverse coefficient ($C_{10}$) value across all tendon specimens was 1.1 kPa, which was considerably higher than the average ($C_{10}$) of 0.4 kPa across median nerve specimens (Table 4). The deep flexor tendons had the largest average $C_{10}$ coefficient at 1.3 kPa, with the superficial tendons and FPL having lower average coefficient values of 1.0 kPa and 0.5 kPa, respectively.

For the axial coefficients ($k_1$ and $k_2$), which reflect the load carried by the fiber reinforcement portion of the constitutive model, the average $k_1$ coefficient for all of the flexor tendons was 59.3 MPa, which was different from the average median nerve value of 2.5 MPa. The deep tendons had the largest average $k_1$ value (68.7 MPa), and the superficial tendons (55.0 MPa) had a slightly lower average coefficient value. The FPL had the lowest average $k_1$ coefficient of 22.5 MPa.

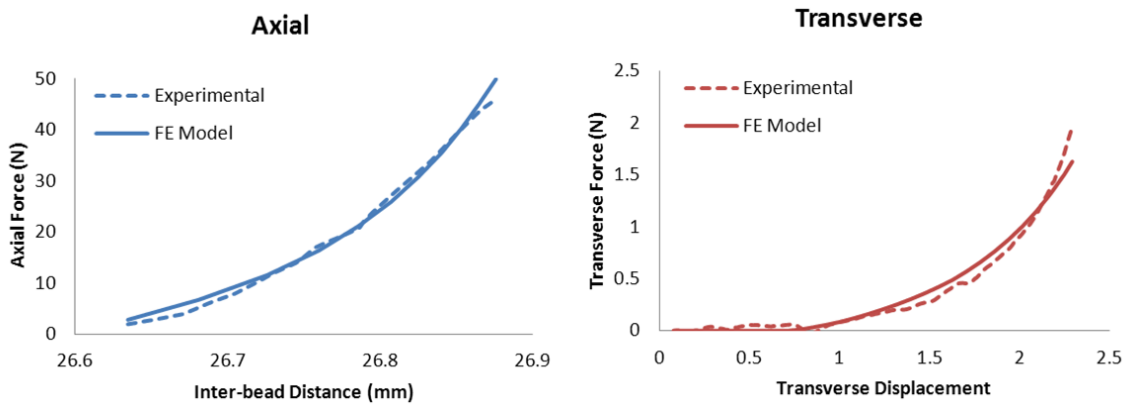


Figure 30. Axial extension curve fit (left) with experimental inter-bead distance versus axial force data (blue dashed line) and the resulting data obtained from the optimized FE material coefficients (blue solid line). The companion transverse compression curve fit (right) with experimental transverse force versus displacement data (red dashed line) and the resulting data obtained using optimized FE material coefficients (red solid line). Curves are from an illustrative S2 tendon with optimized coefficient values of $C_{10}$ = 1.2 kPa, $k_1$ = 40.7 MPa, and $k_2$ = 2.0x10$^3$.

Table 4. Average anisotropic hyperelastic coefficient values for the digital flexor tendons and the median nerve from the three randomly selected hands.

| | $C_{10}$ (kPa) | | $k_1$ (MPa) | | $k_2$ (x10$^{-3}$) | |
|---|---|---|---|---|---|---|
| | **average** | *st. dev.* | **average** | *st. dev.* | **average** | *st. dev.* |
| S2 | **1.0** | *0.9* | **59.1** | *17.0* | **2.5** | *0.3* |
| S3 | **1.3** | *1.1* | **50.2** | *35.9* | **3.8** | *0.9* |
| S4 | **0.8** | *0.7* | **55.7** | *43.1* | **3.1** | *1.0* |
| D2 | **1.6** | *1.8* | **50.7** | *22.0* | **2.3** | *1.2* |
| D3 | **1.7** | *1.1* | **108.2** | *65.5* | **4.4** | *4.0* |
| D4 | **0.6** | *0.5* | **45.0** | *14.1* | **3.2** | *0.9* |
| D5 | **1.3** | *0.3* | **70.8** | *15.6* | **1.1** | *0.3* |
| FPL | **0.5** | *0.3* | **22.5** | *3.7* | **1.9** | *0.7* |
| Nerve | **0.4** | *0.5* | **2.5** | *3.5* | **0.1** | *0.1* |

The average dimensionless $k_2$ coefficient for the digital flexor tendons ($2.8x10^3$) was again considerably different from that for the median nerve ($0.1x10^3$). The superficial tendons had the largest average $k_2$ coefficient value of $3.13x10^3$, while the deep tendons and FPL had lower coefficient values of $2.75x10^3$ and $1.92x10^3$, respectively.

## Validation

As previously described, the transverse compressive behavior of a flexor tendon was examined experimentally under variable axial loads (Figure 23). In that experiment, an increase in transverse stiffness was observed with increasing axial load. To ensure that the optimized anisotropic coefficient values accurately portrayed this pattern of stiffer compressive behavior with increasing axial tension, a set of optimized material property coefficients was calculated for one axial load, and then that material property was used in simulations at different axial loads.

Using the methodology described in this chapter, optimized anisotropic hyperelastic coefficient values were determined for the tendon that had previously been transversely tested at multiple axial loads. Like all other the optimization runs, coefficients were optimized using the transverse compression test performed under 15 N of axial load and the axial extension data obtained from analysis of photographic sequences of the tendon under loads ranging from 1.5 N to 50 N. The optimized coefficients were then used in simulations of transverse compression under the same variable axial load that were used experimentally. In those simulation, the models were prescribed a single axial loading step to desired axial load (3 N to 30 N) followed by a transverse compression step to 40% of the tissue's major axis.

Transverse force versus compression data at each applied axial load was extracted from the FE model and overlaid onto the experimental transverse compression data under the same applied axial loads. The resulting FE curves

reasonably fit the observed experimental behavior (Figure 31), demonstrating increasing transverse compressive stiffness with increasing axial tensile loads. This indicated that coefficients for the fiber reinforced anisotropic hyperelastic material definition that were optimized at one axial load could also be used to accurately reflect transverse behavior under a variety of different tensile loading activities.

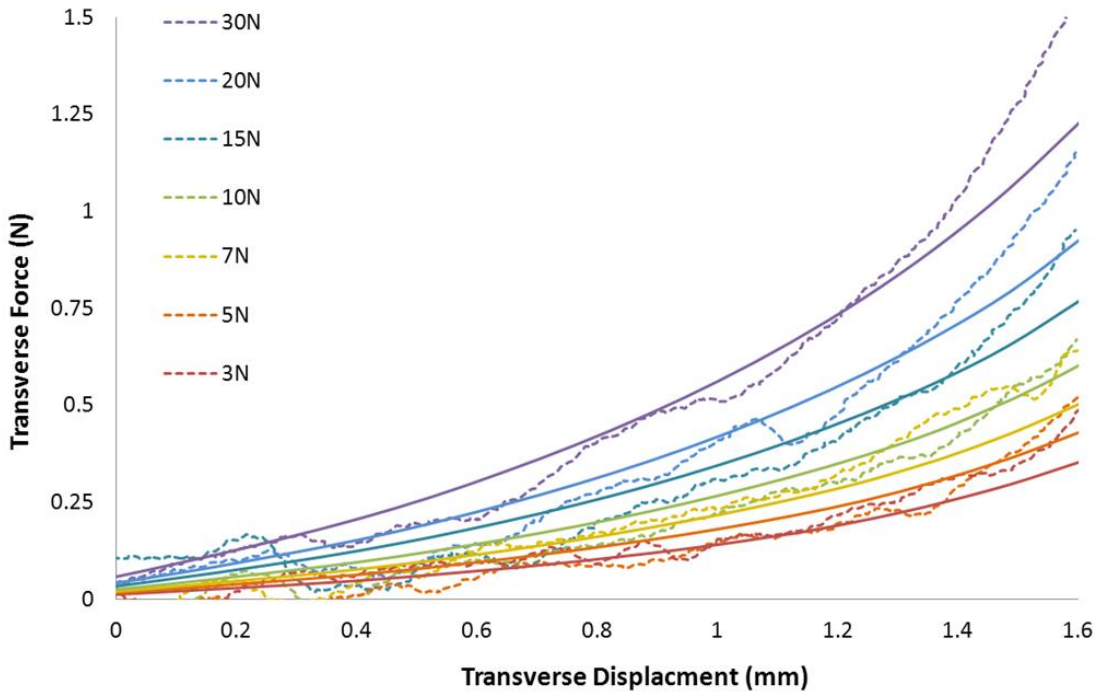


Figure 31. Experimental transverse force versus compression data (dashed lines) and transverse force versus compression data extracted from FE models (solid lines) for a superficial flexor tendon whose compressive behavior was measured and modeled at increasing axial loads. Identical material properties were used in all seven FE simulations.

## Discussion

The fiber-reinforced anisotropic hyperelastic material property definition was able to characterize both the axial tensile and transverse compressive behavior of the digital flexor tendons and the median nerves. The optimized coefficient values for the

digital flexor tendons were appreciably stiffer than for the median nerve specimens in both axial extension and in transverse compression. Since the median nerve is considerably less stiff transversely, contact between the nerve and the more rigid flexor tendons can lead to the development of elevated contact stress on the median nerve. No formal statistical comparisons were made between the different flexor tendons or between the flexor tendons and the median nerve because of the small sample size of only three cadaveric specimens.

Only minimal axial extension was observed for the digital flexor tendons under applied tensile loads up to approximately 50 N. These small deformations corresponded to axial tendon strains below 1%, as calculated from the FE models. Based on descriptions of tendon extension found in the literature, axial strains of less than 2% are considered to be in the toe region of the stress-strain curve (Wang 2006). Thus, the material properties derived in this work characterize the combined axial tensile and transverse compressive mechanical behavior of the digital flexor tendons within the toe region of the stress-strain curve. The axial loads applied in this work adequately reflect the physiologic tensile loading that the flexor tendons experience during functional activities. Tensile forces on the superficial flexor tendons during tapping and grasp maneuvers have been measured at 13 N and 39 N, respectively (Schuind et al. 1992; Dennerlein 2005). Thus, the characterization of the tendon axial behavior under applied loads of up to 50 N adequately reflects functional behavior of the digital flexor tendons. To integrate more vigorous activities beyond the grip and tapping activities characterized, increased axial loads beyond 50 N would need to be applied and incorporated into the modeling and optimization routine.

Unlike the digital flexor tendons, the primary function of the median nerve is not to transmit axial load. The median nerve is not structurally reinforced by the extensive arrangement of axially oriented collagen fiber bundles that make up the digital flexor tendons. Since the nerve lacks collagen structure, it undergoes significantly more

deformation during axial tensile loading as compared to the flexor tendons. Under tensile loads of 20 N, the median nerves underwent axial displacements corresponding to approximately 8% tissue strain. Median nerves have been shown to exhibit nonlinear elastic deformation, with a relatively long toe region out to approximately 15% strain (Grewal et al. 1996). Therefore, the characterization of tensile behavior of the median nerve in this work was also within the toe region of the tissue's stress-strain curve. One study has examined the elongation of the median nerve between the shoulder and the wrist. The median nerve underwent an elongation of 4% – 5% during extension of the elbow, and was subjected to additional elongation with wrist and finger flexion (Millesi, Zoch, and Reihsner 1995). The stains applied to the median nerves in the present work exceeded the observed elongation during elbow extension, and accommodate strain associated with finger and wrist flexion. Therefore, physiologically relevant stains were used in the characterization of the axial tensile properties of the median nerve.

Inter-bead distance measurements obtained experimentally were used to model the axial extension behavior of the flexor tendons and median nerve within the FE models. The first inter-bead distance measurement was taken at the lowest applied axial, and there was no zero load inter-bead distance measurement. The tensile behavior of the tissue was extrapolated to 0 N from the lowest applied axial load. It was assumed that the estimation of the initial load uptake region by the FE model, prior to the lowest applied axial load, would not dramatically alter the material properties obtained.

The fiber-reinforced anisotropic hyperelastic constitutive model fit in this work utilized a Neo-Hookean material property definition to characterize the matrix material of the modeled tissues. With only a single coefficient, the Neo-Hookean model was not able to fully accommodate the nonlinearity and long toe regions associated with transverse compression of the flexor tendons and median nerves. However, the model

does provide a reasonable representation of the properties for comparison between the individual flexor tendons and the median nerve.

For one of the axially tested flexor tendons and one median nerve, no optimized anisotropic hyperelastic values could be determined. For the flexor tendon, the transverse compressive behavior measured experimentally was approximately two times less stiff than the other flexor tendons. When the stiff axial fibers were implemented into the FE model for this tendon, the model could not simultaneously match the very compliant transverse compressive behavior. With the median nerve specimen, the axial tensile properties were three to four times stiffer than the other median nerves. Again, the fiber-reinforced material property definition could not simultaneously fit the stiff axial tensile behavior and the compliant transverse compressive behavior. For both tissues, the $C_{10}$ coefficient governing the compressed matrix material in these FE models was essentially driven to zero by the optimization routine because the axial fibers were already providing more than enough transverse stiffness. Since the FE model could not accommodate the axial tensile and transverse compressive properties at the same time, converged solutions for the anisotropic hyperelastic coefficients were not obtained for the flexor tendon and median nerve.

The anisotropic hyperelastic material property definition provided a reasonable means to represent both the axial tensile and transverse compressive behavior of the digital flexor tendons and the median nerve. These properties are suitable for implementation into FE models of the carpal tunnel, and can be used to reflect the changes in the transverse compressive behavior of these tissues associated with the variable axial loads applied to them during functional hand activities.

# CHAPTER V: COMPRESSIVE PROPERTIES OF THE TRANSVERSE CARPAL LIGAMENT

As the volar bound of the carpal tunnel, the TCL serves as an important part of the flexor tendon pulley system in the hand. Interactions between this ligament and both the digital flexor tendons and the median nerve may play a role in the development of high contact stress on the median nerve. Numerous studies have investigated the TCL's role in regulating the compliance of the carpal tunnel. However, only a limited number of these studies have evaluated the mechanical properties of the TCL independent of its contribution to the behavior of the TCL/carpal bone complex. Further limiting their utility, these studies have only addressed the properties of the ligament in tension. The tensile properties are less than ideally relevant in the development of contact stress on the nerve, since the primary interaction between the nerve and the TCL is in compression. Therefore, in the final portion of this work, the compressive behavior of the TCL was determined experimentally using indentation testing, and an optimization technique used to fit an Ogden material property model to characterize the TCL behavior. The techniques used were very similar to those that were previously used to fit constitutive models to the compressive behavior of the flexor tendons and the median nerve.

## Experimental Methodology

Intact carpal tunnels were dissected from five fresh-frozen cadaveric forearm specimens (69 – 90 years old, 3 male and 2 female). Prior to dissection, the specimens were thawed at room temperature overnight. The first step of dissection was removal of the median nerve and digital flexor tendons from inside the tunnel. Next, the carpal bone complex was disarticulated from the metatarsals, and finally the intact carpal tunnel was disarticulated from the radius and the ulna. The remaining intact carpal tunnel section included the nine carpal bones, intercarpal ligaments, and the TCL. All

excess soft tissues (skin, muscle, fat, etc.) were carefully removed from the volar surface of the TCL and the surfaces of the carpal bones. Caution was taken to preserve all tissue that provided internal stabilization of the carpal bones. K-wires, 0.35 inches in diameter, were placed in the four volar-most carpal bones with TCL attachment sites (scaphoid, trapezium, pisiform, and hamate) to provide further stabilization of the intact tunnel. The wires were drilled through the entirety of each TCL-connected carpal bone and into and through the carpal bones on the dorsal side of the tunnel. Additional wires were placed between the proximal and distal rows of carpal bones on the dorsal side of the tunnel.

A center point of the TCL was then determined using landmarks on the carpal bones with TCL attachment sites. The identified landmarks were the volar-most aspect of each carpal bone. The TCL center location was defined as the point halfway between the hamate and trapezium landmarks in the radial/ulnar direction, and half of the specimen's proximal/distal width at that location. Next, a fiber axis corresponding to the TCL's preferential collagen orientation (Prantil et al. 2010) was defined by defining a line connecting the midpoint between the hamate and pisiform landmarks, and the midpoint between the trapezium and scaphoid landmarks (Figure 32).

The dorsal aspect of the stabilized carpal tunnel complex was then potted in polymethyl methacrylate (PMMA) to preserve the anatomical orientation of the TCL for testing (Figure 33). A square PMMA form with perpendicular cross-hairs was used to maintain specimen alignment for PMMA potting. The TCL specimen's center location was positioned under the intersection of the form's cross-hairs, and the entire specimen was rotated about that center location until the TCL fiber axis was aligned with the potting form's radial/ulnar cross-hair. Once cured and removed from the potting form, excess PMMA was cut from the outer edges of the potted carpal tunnel specimens, and an access point to the dorsal side of the TCL was created by cutting away the PMMA and dorsal carpal bones in the central region of the potted specimen.

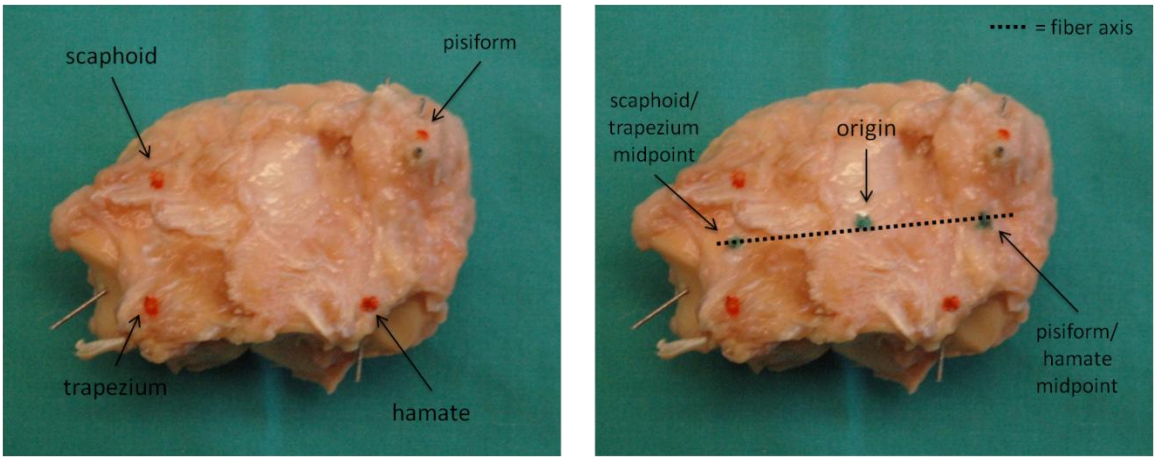


Figure 32. Landmarks (orange dots) identified (left) on the TCL's attachment sites on the scaphoid, trapezium, pisiform and hamate. Midpoints between the scaphoid/trapezium and the pisiform/hamate and the TCL origin were identified as shown with the green marks (right). The ligament's preferential fiber axis is illustrated (right), with the dashed line connecting the scaphoid/trapezium and pisiform/hamate landmarks.

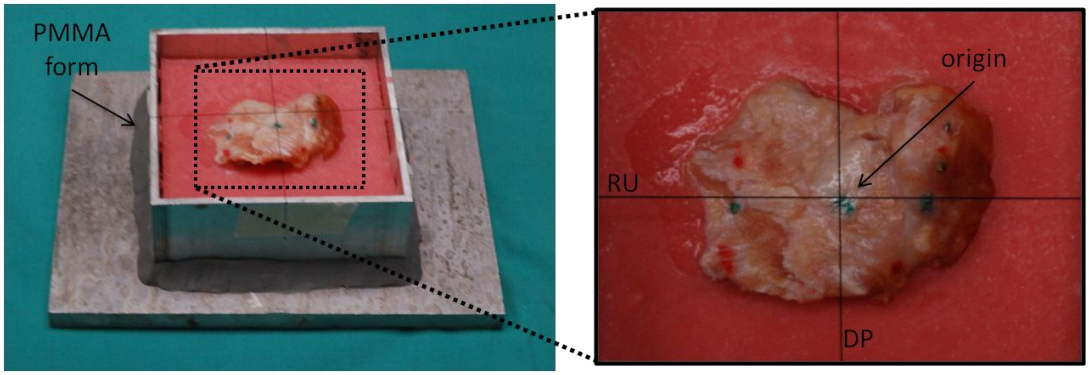


Figure 33. Potting a TCL specimen using the PMMA form, with cross-hairs corresponding to the intersection of an axis in the radial/ulnar (RU) direction and one in the distal/proximal (DP) direction.

The two potted ends of the carpal tunnel were then attached to a tensioning apparatus (Figure 34). The tensioning apparatus was comprised of two Delrin blocks that slide along metal rods in the base of the fixture. Four leveling screws located on each corner of the apparatus allowed for leveling and adjusting the height of the TCL

surface. A constant physiological tensile load of 5 N, characteristic of a grasp maneuver (Schuind et al. 1995), was applied in the radial/ulnar direction by stainless steel compression springs. Prior to the attachment of the PMMA blocks to the tensioning apparatus, the springs were compressed to a length of ½ inch using a c-clamp (Figure 35). Super-glue was then used to attach the PMMA blocks to the appropriate locations on the Delrin block surfaces, while the springs were compressed with the c-clamp. Once the glue had set, the c-clamp was released, freeing the springs to apply a 5 N tensile load across the ligament. A total of 5 testing locations were identified on each specimen. The first location was the previously identified center location. Distal, proximal, radial, and ulnar locations were identified 5 mm in their respective directions from the central location (Figure 36).

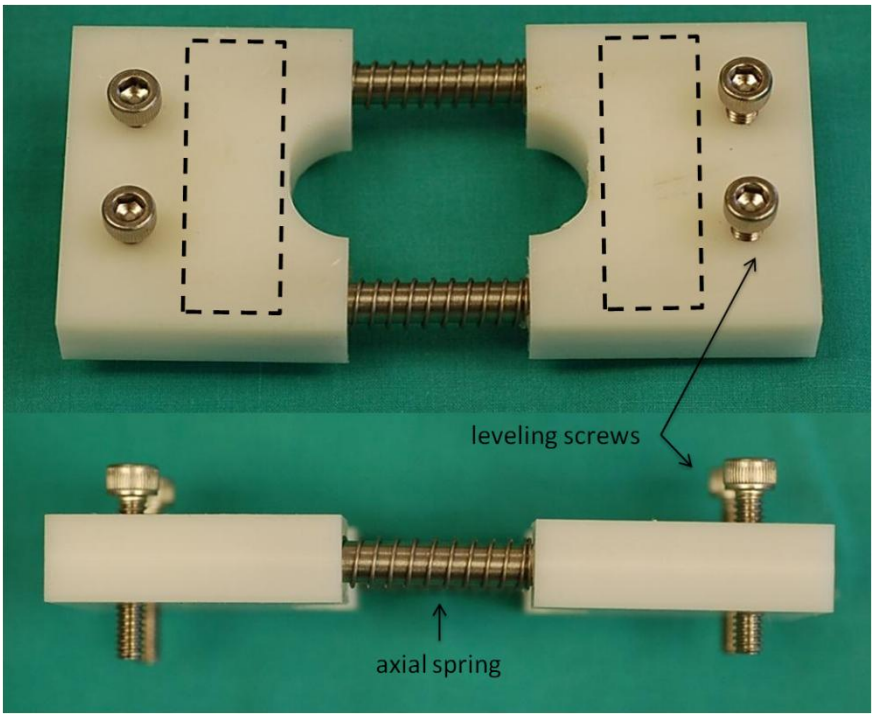


Figure 34. Oblique top view (top) and side view (bottom) of the TCL tensioning apparatus in the uncompressed state. Dash rectangles correspond to the PMMA block attachment sites.

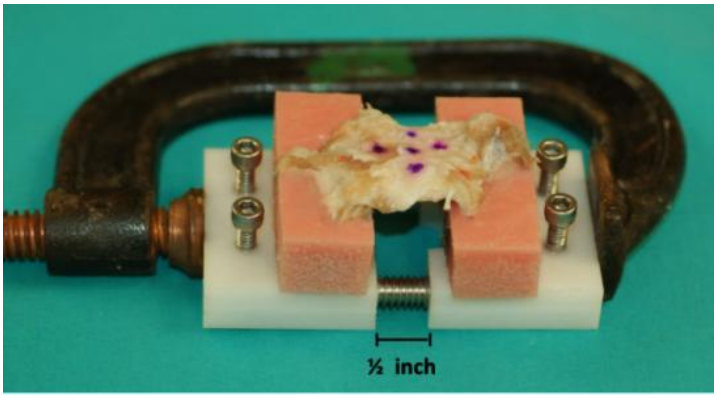


Figure 35. A c-clamp has been used to compress the springs between the Delrin blocks to a length of ½ inch. The PMMA blocks have been attached to the tensioning device while the springs are compressed. When the c-clamp is released, the compressed springs push out, thus applying 5 N of tension to the TCL specimen in the radial/ulnar direction.

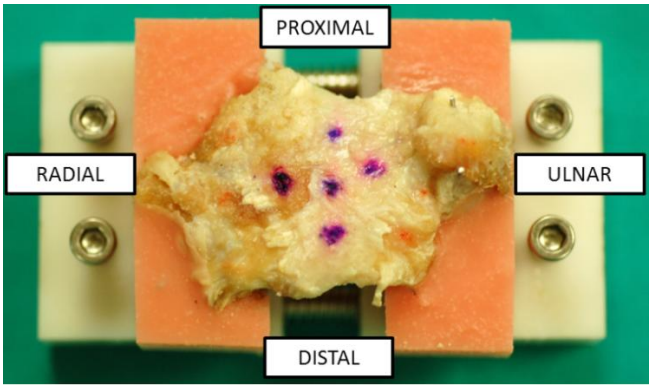


Figure 36. Testing locations identified on a TCL specimen ready for testing. The proximal, distal, ulnar, and radial testing sites are located 5 mm from the central location.

The indentation testing device (Figure 37) utilized a 3 mm diameter flat indentation tip mounted on an MTS Insight actuator in series with a 100 N load cell. The indentation tip was magnetically attached to a metal platform mounted on the bottom of the load cell. This magnetic attachment allowed for side-to-side movement of the indenter tip for precise alignment of the indentation tip over the indentation base. The

indentation base consisted of a flat metallic platen (3 mm in diameter) that was positioned within a saline bath. Zero displacement of the indentation device was established by bringing the indentation tip into contact with the indentation base without a specimen in between, until a load of 25 N was achieved. Within the indentation testing apparatus, the dorsal surface of the TCL rests on top of the indentation base, and indentation testing is performed through the downward movement of the indentation tip.

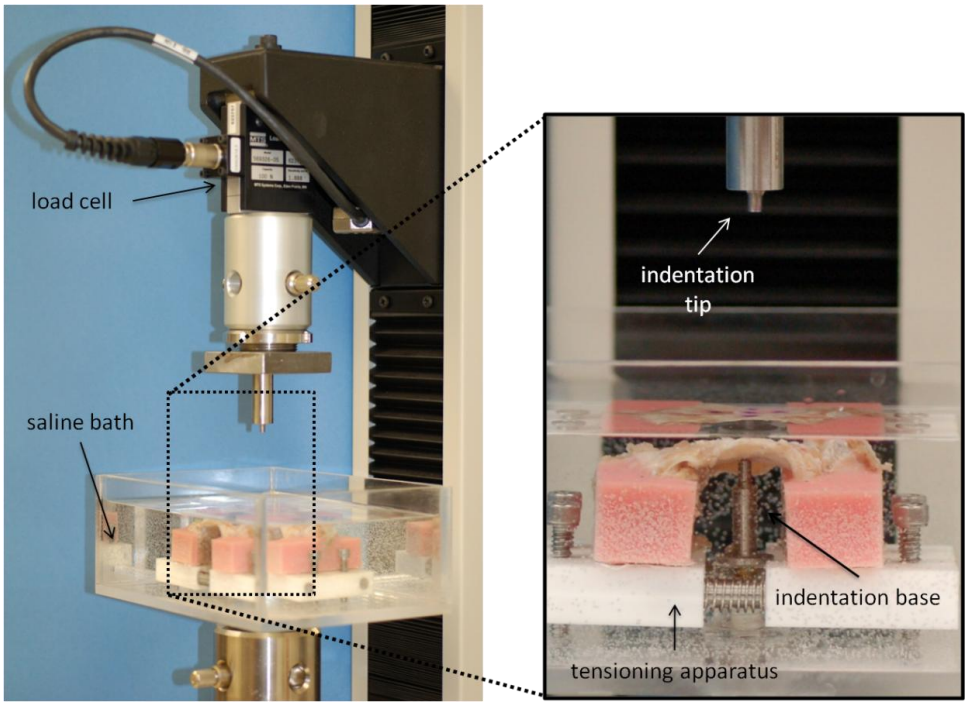


Figure 37. TCL indentation set-up shown with a TCL specimen attached to the tensioning apparatus and immersed in a saline bath.

Prior to specimen insertion into the indentation apparatus, the height/angulation of the dorsal surface of the TCL was adjusted using the leveling screws on the tensioning apparatus. This leveling step was performed because of the high variability in TCL thickness and the angle/height of the dorsal ligament surface at

each of the different testing locations on the individual specimens. To perform the leveling, the tensioning apparatus, with the attached specimen, was placed on the leveling apparatus, which consisted of a flat surface with a post replicating the geometry of the testing device indentation base (Figure 38). The leveling screws in the tensioning apparatus were adjusted until the dorsal surface of the TCL at the indentation site laid flat against the top of the indentation base replica. This leveling procedure was performed outside of the fluid bath in the testing device to improve the ability to visually assess the appropriate height of the ligament.

After the height/angulation adjustment of dorsal surface of the TCL at the desired testing location, the tensioning apparatus supporting the TCL was placed into a saline bath enclosing the indentation testing device. Then, the indentation site that had been properly adjusted using the leveling apparatus was centered over the indentation base. The tissue thickness was then assessed by lowering the indentation tip onto the tissue at a loading rate of 0.05 mm/s. Tissue thickness was determined as the distance between the indentation base and indentation tip at the instant where the measured load became higher than 0.05 N.

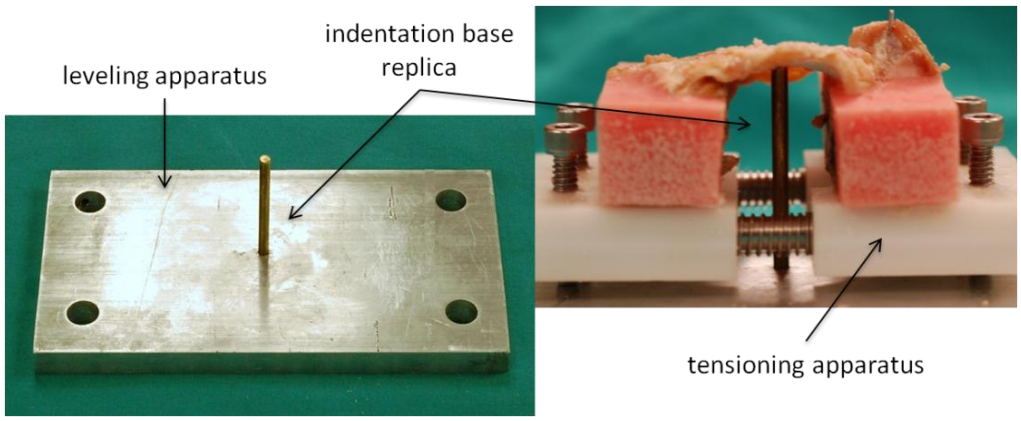


Figure 38. The replica of the indentation base on the leveling apparatus was used as a reference surface, and the leveling screws on the tensioning apparatus were used to adjust the height of the dorsal side of the TCL to this reference.

After the tissue thickness measurement, 10 cycles of cyclic loading to 10% strain, followed by unloading, were applied at a rate of 0.5mm/s to precondition the tissue. After preconditioning, the ligament was allowed to recover in the saline bath for 20 minutes. Displacement-controlled indentation testing was then performed at a loading rate of 0.5 mm/s, up to 40% of the tissue thickness. Indentation force and tip displacement were reported during each test. A total of three replicate indentation tests were performed per testing site, with a 20-minute recovery interval in the saline bath between tests. The tissue thickness was measured prior to each replicate test using the same procedure as used during preconditioning. Upon completion of the three indentation tests at a given site, the specimen was removed from the testing device and the height/angulation of the dorsal TCL surface was adjusted for the next testing location on the tissue. Identical preconditioning and indentation testing protocols were followed for each site on all five TCLs that were tested.

A device compliance correction similar to that used on the experimental data from the compression of the flexor tendons and median nerves, was applied to the TCL indentation data. The compliance of the TCL indentation apparatus was determined by bringing the indentation tip into contact with the indentation base in displacement control, followed by loading the apparatus to 100 N (Figure 39). The slope of the resulting force versus MTS displacement ($D_{MTS}$) curve was the device stiffness, and the inverse of that stiffness constituted the compliance of the indentation apparatus (0.00182 mm/N). The true displacement of the indenter ($D_{Indenter\ Tip}$) was calculated from the measured experimental data using the following equation:

$$D_{Indenter\ Tip} = D_{MTS} - (Force * 0.00182)$$

An average indentation force versus displacement curve for each compression site was calculated by averaging the three replicate indentation data sets. An average

thickness measurement for each testing site on the TCL specimens was also obtained by averaging thickness measurements from each of the three replicate indentation trials.

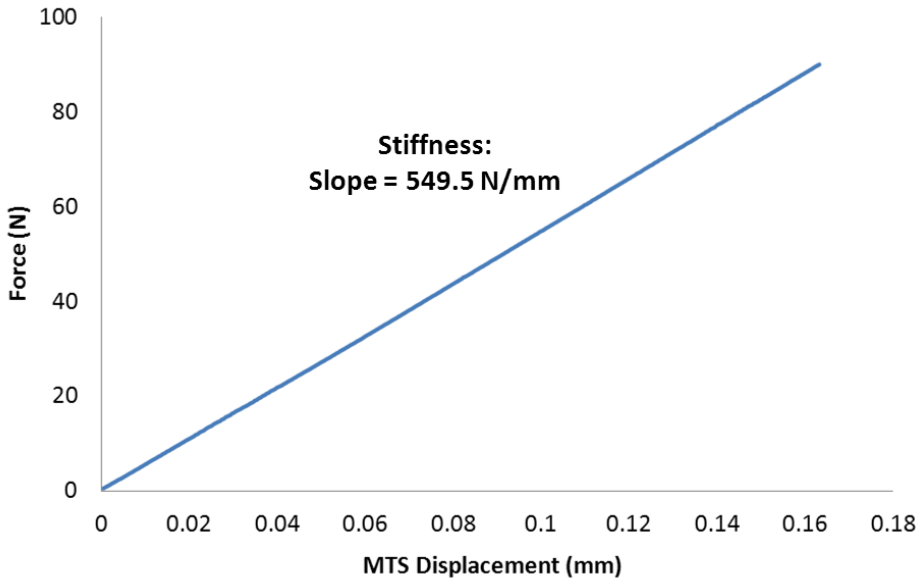


Figure 39. Compliance of the TCL indentation apparatus measured during direct contact between the indentation tip and indentation base. The slope of the force versus measured MTS displacement curve is the device stiffness (549.5 N/mm) and the inverse of that slope (0.00182 mm/N) is device compliance.

## Finite Element Model

An axisymmetric, site-specific FE model for each TCL test location was created in ABAQUS CAE (Figure 40). The indentation tip and base were modeled as rigid surfaces using a total of 25 rigid axisymmetric 2-node elements (RAX2) for each part. A bevel, with a radius of 0.5 mm, was added to the edge of both the indentation tip and indentation base to improve model convergence in the region where the indenters contacted the tissue specimen. The compression sites on the TCL specimen were modeled using a 9 mm tissue length and the average tissue thickness calculated from the three replicate indentation tests. A 1.5 mm span of increased mesh refinement (5

elements/mm along the x-axis) was added to the region that would contact the corner of the indenter. The tissue was meshed with continuum axisymmetric 4-node hybrid elements (CAX4H). A total of approximately 5,000 elements were included in the model, depending on tissue thickness. The TCL indentation behavior was modeled using the same first-order Ogden hyperelastic material property definition that was used for the transverse compression-only material property assessments of the flexor tendons and median nerve. Again, coefficients μ and α govern the material behavior for this constitutive model.

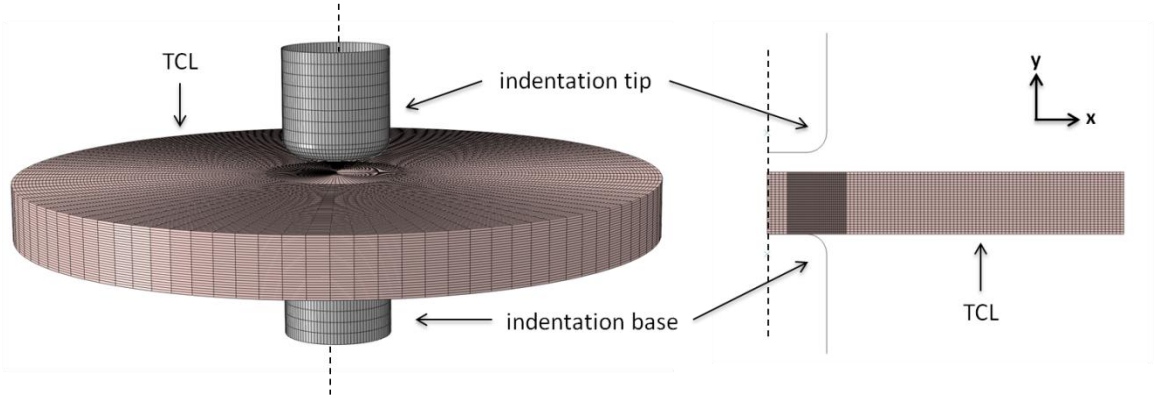


Figure 40. Axisymmetric model revolved around its axis of symmetry (dashed line) for display purposes (left). The actual appearance of the 2D axisymmetric model used for analysis shown on the right.

Indentation of the TCL was modeled by prescribing displacement of rigid body reference nodes on the indentation tip and base (Figure 41). The entire model was constrained along the axis of symmetry to simulate the presence of the surrounding tissue, by using an axisymmetric boundary condition that prevented motion perpendicular to the axis of symmetry (motion in the x-direction). The nodes along the remote edge of the tissue, away from the symmetry axis, were constrained against both x-direction and y-direction movement.

Contact was defined between the outward surfaces of the indenter tip and base and the top and bottom surfaces of the TCL mesh. In the first step of the analysis, the indentation base was displaced upwards approximately 0.05 mm to achieve slight contact between the indentation base and bottom surface of the TCL. This movement was representative of the height adjustment of the tensioning apparatus, used to align the dorsal side of the TCL at the testing location with the indentation base replica. The indentation base was then held fixed in y-direction while the indentation tip was displaced downwards a distance corresponding to 40% of the modeled tissue thickness. The rigid body reference node on the indentation tip was used to collect reaction force data.

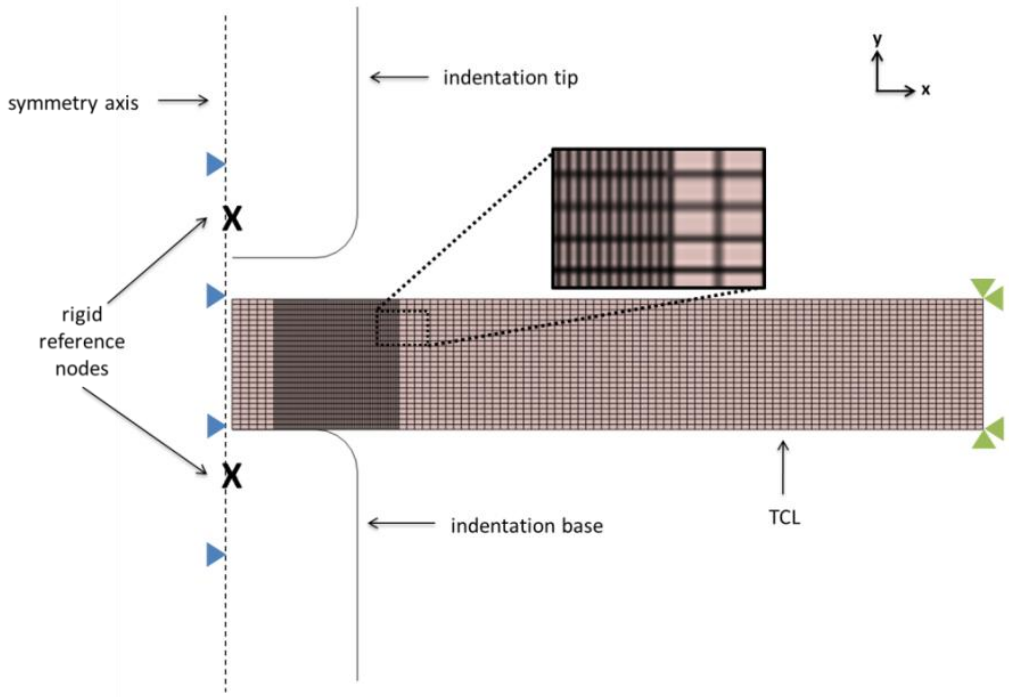


Figure 41. Rigid body reference nodes on the indentation tip and base were used to drive the FE model of TCL indentation. The entire model was constrained along the symmetry axis in the x-direction (blue fixities) and the remote end of the tissue specimen (away from the symmetry axis) was constrained against motion in both the x- and y-direction (green fixities).

## Optimization Routine

The axisymmetric FE model of the TCL was used with a slightly adapted version of the MATLAB least-squares nonlinear optimization function previously used to obtain Ogden coefficients for the transverse compression-only behavior of the flexor tendons and median nerve (Figure 13). As before, the first FE model was run using initial coefficient values for μ and α, and through iterative incremental changes in coefficient values, the error between the experimental and FE indentation force-versus-displacement curves was minimized. The same convergence criteria were applied to the TCL optimization routine as those used in the previous optimization routines. Each individual FE model took less than 1 minute to run to completion, and the average convergence time for the entire optimization routine was approximately 30 minutes.

A series of t-tests were used to compare the μ and α coefficients determined by optimization routine for the different TCL testing sites. Comparisons were made between the different sites (center, proximal, distal, radial, and ulnar) on a given ligament, as well as between different ligament specimens.

## Validation and Supplemental Modeling

During experimental testing, the tensile load was applied to the TCL via compression springs at the base of the tensioning apparatus. To confirm that the theoretical load applied by the springs was in fact fully transmitted to the ligament, rather than being partially lost to friction from the Delrin blocks binding on the metal rods, a simple validation test was performed. First, the tensioning apparatus was prepared by compressing the two compression springs in the base of the tensioning apparatus to ½ inch using a c-clamp, as was consistent with the application of the 5 N tensile load. Next, a 500 g mass was hung from an extension spring used to simulate the TCL, and the spring's extension under load was measured between marked locations on each end of the spring. The extension spring was then stretched across the top of

the tensioning apparatus and attached between parallel wires spanning the two leveling screws on each side of the apparatus. This attachment method positioned the extension spring a distance of 22 mm above the surface of the Delrin blocks, which was the approximate distance of the TCL specimens above the Delrin blocks during indentation testing (Figure 42). The stretched length of the extension spring attached to the top of the tensioning apparatus was adjusted using the attachment wires, so that the distance between the two marked end locations equaled the distance that was measured when the 500 g weight was hung from the spring. Once the length of the extension spring had been adjusted, the tensioning apparatus was released from the c-clamp. If the 5 N force applied by the two compression springs at the base of the tensioning apparatus was perfectly transferred to the extension spring simulating the TCL, both the extension and compression springs should remain at the same length they were before the Delrin blocks were released from the c-clamp.

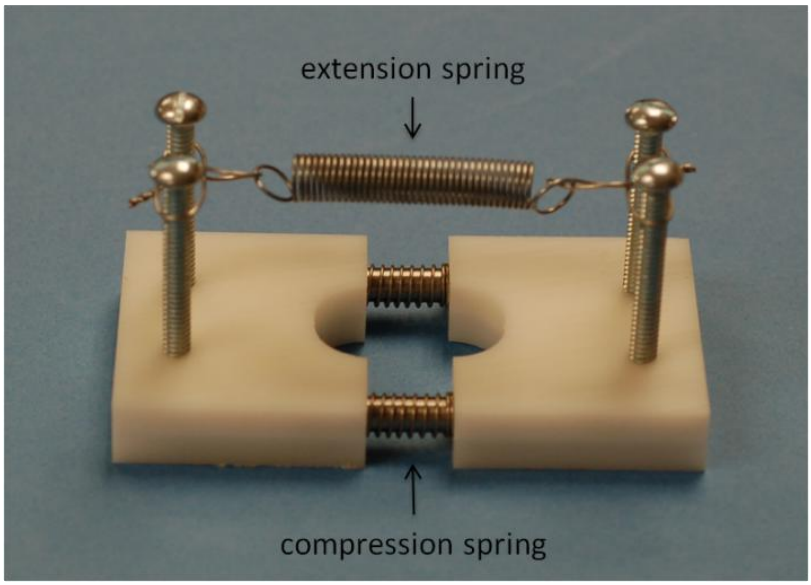


Figure 42. Tensioning apparatus with extension spring mounted above the Delrin blocks between the leveling screws.

The distance between the two Delrin blocks at the base of the testing fixture and the distance between the two end locations on the extension spring were measured using calipers. A series of four replicate measurements were obtained, two of which were performed in a fluid bath to be consistent with the experimental set-up. The distance measurements were converted to force measurements, assuming linear displacement of the springs. For the compression springs, force was calculated using the known Delrin block-to-block distance at 5N, and for the extension spring the force was calculated using the known spring extension when loaded with the 500 g mass. The loads applied by the compression springs and experienced by the extension spring were compared, and the percent difference between the two values was calculated with respect to the load applied by the compression springs. The extension spring experienced a maximum 3% reduction (average 0.8% reduction) in load from what was applied by the compression springs, with this maximum difference occurring outside of the fluid bath. As a result of the minimal difference between the forces applied by the compression springs and the force experienced by the extension spring simulating the TCL, it was concluded that the full 5N tensile load was applied to the TCL during testing, and no appreciable load was lost as a result of friction in the apparatus. Thus, the tensile load applied to the TCL was reasonably approximated as 5 N.

During indentation testing, TCL thickness was assessed by the MTS insight as the distance between the indentation tip and indentation base, at the point which the indentation force first rose above 0.05 N. To validate the 0.05 N load used in this definition of a specimen's thickness, a series of caliper measurements taken at the different testing locations was compared to the average TCL thickness values determined using the 0.05 N load criterion. The difference in the between the two TCL thickness measurements was small (average 13.1%) and may have been somewhat exaggerated by experimental error associated with compressing the tissue during the

caliper measurement. Thus, the 0.05 N loading criteria used to determine specimen thickness was considered acceptable.

One of the primary modeling assumptions associated with the FE models of the TCL was use of the average thickness measurement from the three replicate compression trials to generate the FE model. Any error in this thickness measurement would change the geometry of the FE model, and therefore would influence the coefficients obtained with the optimization routine. Among all testing locations on all TCL specimens, the largest standard deviation in thickness measurements made over the three replicate indentations tests was 0.11 mm (typical standard deviations were 0.05 mm). To validate the use of the average TCL thickness measurement for generation of the FE model of an individual TCL testing location, two additional FE meshes were generated for the TCL specimen with the largest standard deviation in the tissue thickness measurement. These additional models had a thickness ± one standard deviation (0.11 mm) from the site-average thickness (1.45 mm). These models were run through the optimization routine, and the resulting coefficient values were compared to the original coefficient values obtained using the FE model with the average TCL thickness measurement. The maximum relative difference from the original solution was 9.6% for the $\mu$ coefficient, which occurred using the plus-one-standard-deviation tissue model. The maximum relative difference from the original solution for the $\alpha$ coefficient was 12.2%. This maximum difference occurred using the minus one standard deviation tissue model. Since these small differences represented a worst-case scenario (using the specimen with the largest variability in thickness measurements between trials), using the FE models based on the TCL test site average thickness for optimization was considered reasonable for all specimens' indentation testing locations.

## Results

The optimized first-order Ogden coefficients provided good fits of the TCL indentation data (Figure 43), and unique convergence was obtained for all of the tested sites on each of the 5 specimens. The overall coefficient means across all testing sites and specimens were 122 kPa for μ and 16.4 for α. The standard deviations around those means were significantly higher for the μ coefficient (± 99 kPa) versus the α coefficient (± 1.8).

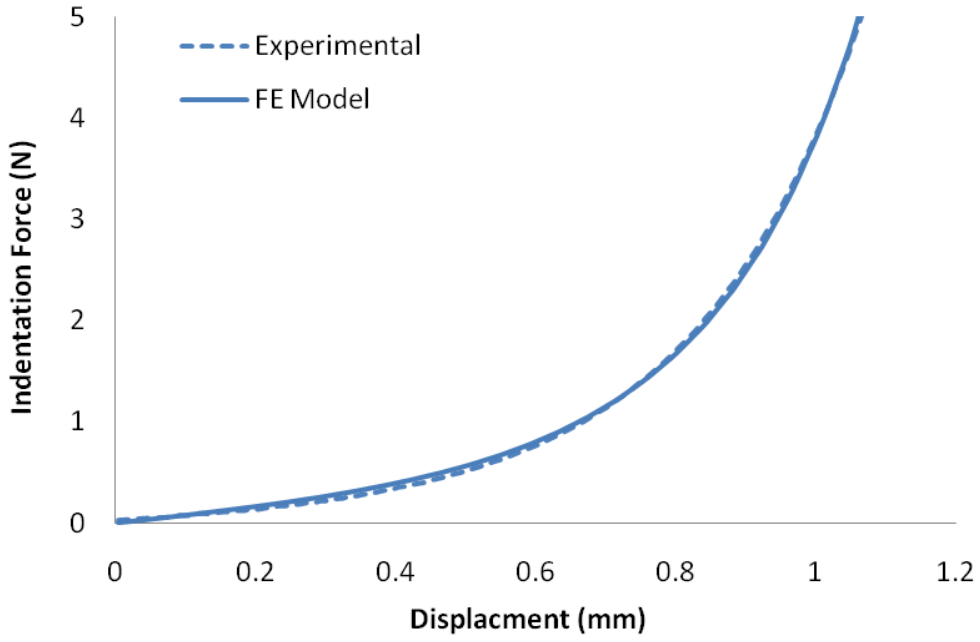


Figure 43. Plot of indentation force versus displacement for the distal compression site on TCL specimen 4. Experimental data are shown by the dashed line, and the FE data output using the optimized fit of the data (μ = 103.1 kPa and α = 16.8) are shown by the solid line This particular curve was selected for display because the optimized coefficients were close to the overall coefficient means for all specimens and locations.

The across-site average Ogden coefficients for each specimen are shown in Figure 44. As shown by the dispersion bars, there was larger variability in the μ

coefficient across sites in a given specimen than in the α coefficient. Statistically significant differences in the optimized μ coefficient were found between specimens 2 and 4 ($p = 0.08$) and specimens 2 and 5 ($p = 0.07$). For the α coefficient, significant differences were found between specimen 2 and specimens 3 ($p = 0.02$) and 5 ($p = 0.03$). However, when comparing the Ogden coefficients from the five different indentation sites on the TCL specimens, no significant difference was found for either coefficient (Table 5).

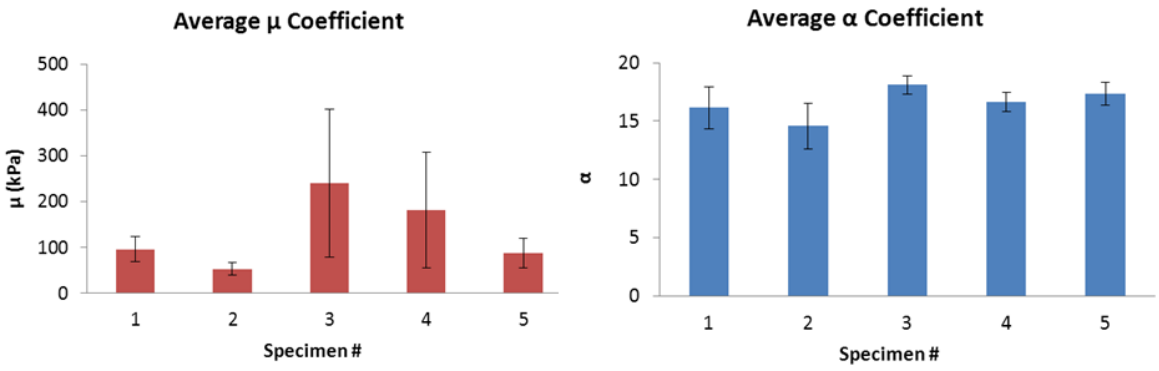


Figure 44. Average Ogden coefficients (μ and α) across the 5 testing locations (center, proximal, distal, ulnar and radial) for each tissue specimen.

The across specimen average thickness was largest for the distal compression site (2.8 mm), with the radial (2.0 mm) and ulnar (2.2 mm) sites also having higher thickness values (Table 6). The proximal and central testing locations were thinner, with average thickness values of 1.8 mm and 1.9 mm, respectively. Statistically significant differences in TCL thickness values were found between the central and distal locations ($p = 0.02$), as well as between the proximal and distal locations ($p = 0.02$).

Table 5. Ogden coefficients obtained by the optimization routine at each of the five testing locations on the different TCL specimens, with average coefficient values for each TCL testing location (center, proximal, distal, ulnar and radial) are given.

| spec. # | center | | proximal | | distal | | ulnar | | radial | |
|---|---|---|---|---|---|---|---|---|---|---|
| | u (kPa) | α | u (kPa) | α | u (kPa) | α | u (kPa) | α | u (kPa) | α |
| 1 | 100 | 15 | 108 | 18 | 126 | 16 | 92 | 18 | 52 | 14 |
| 2 | 53 | 15 | 37 | 14 | 52 | 12 | 74 | 17 | 46 | 15 |
| 3 | 224 | 18 | 408 | 19 | 86 | 17 | -- | -- | -- | -- |
| 4 | 265 | 17 | 361 | 16 | 103 | 17 | 77 | 16 | 97 | 18 |
| 5 | 74 | 17 | 144 | 18 | 68 | 18 | 78 | 18 | 72 | 16 |
| average | **143** | **16** | **212** | **17** | **87** | **16** | **80** | **17** | **67** | **16** |
| *st. dev.* | *95* | *1* | *163* | *2* | *29* | *2* | *8* | *1* | *23* | *2* |

Table 6. Width, length and average thickness measurements for the tested TCL specimens.

| | | | center | proximal | distal | ulnar | radial |
|---|---|---|---|---|---|---|---|
| **spec. #** | **width** (mm) | **length** (mm) | **average thickness** (mm) | | | | |
| 1 | 27.0 | 26.0 | 1.4 | 1.4 | 2.8 | 1.8 | 2.0 |
| 2 | 30.0 | 24.5 | 1.6 | 2.5 | 2.8 | 2.6 | 1.8 |
| 3 | 27.5 | 27.5 | 1.9 | 1.8 | 2.5 | -- | -- |
| 4 | 34.0 | 34.0 | 1.5 | 1.6 | 2.7 | 2.2 | 2.2 |
| 5 | 34.0 | 26.0 | 3.2 | 1.4 | 3.2 | 2.1 | 2.0 |
| average | **31** | **28** | **1.9** | **1.8** | **2.8** | **2.2** | **2.0** |
| *st. dev.* | *3* | *4* | *0.7* | *0.5* | *0.2* | *0.3* | *0.1* |

The ulnar and radial locations were not tested on specimen 3 due to the small size of that TCL. Width was the proximal/distal dimension of the tissue at the location of the central testing region. Length was measured between the hamate and trapezium landmarks identified on the ligament. Average thickness measurements were calculated from the three replicate thickness measurements made prior to an indentation trial.

## Discussion

The first-order Ogden material property definition provided a reasonable means to describe the indentation behavior of the TCL under 5 N of tensile loading, which is characteristic of a grip maneuver. Significant differences were found between Ogden coefficients of the different TCL specimens. The different indentation locations had similar α coefficients. The proximal testing site had the highest average μ coefficient across the different specimens that were tested, while the radial location had the lowest average μ coefficient. For the five TCL specimens evaluated, there was significantly more variance in the μ coefficient, as compared to the α coefficient.

The higher variability associated with the μ coefficient may be a result of the difficulty associated with the complete removal of all excess tissue (muscle, muscle fascia, fat, etc.) from the volar surface of the ligament (Figure 45). An example of tissue present on the surface of the TCL that is challenging to remove is muscle tissue from the thenar and hypothenar muscles, which attach directly to sites on the palmar surface of the ligament. Although great care was taken to completely remove the muscle tissue from the ligaments prior to indentation testing, some excess tissue may have remained on the volar TCL surface. Further contributing to the difficulty of completely isolating the ligament tissue, muscle fascicles from the thenar and hypothenar muscles have also been found interspersed within the collagen fibers of the ligament itself (Rotman and Manske 1993). In addition to difficultly associated with the complete removal of the muscle tissue, a separate fascial layer, derived from the thenar and hypothenar muscle fascia, is also located on the palmer surface of the TCL. It has been shown that the TCL and this facial layer are nearly identical histologically, and that mechanical separation between the fascia and the collagen fibers of the underlying ligament is very hard to achieve (Rotman and Manske 1993). The incomplete removal of extraneous tissues on the surface of the ligament may have contributed to the increased variability observed with the μ coefficient of the Ogden property definition. The μ coefficient predominately

reflects tissue behavior in the load-uptake region of the stress-strain curve, thus initial contact of the indentation tip with a variety of excess tissues on the surface of the ligament may have caused this wide variability. Since the α coefficient predominately influences the latter part of the stress-strain curve, it may be less susceptible to the influence of the incompletely removed excess tissue pieces of the surface of the ligament.

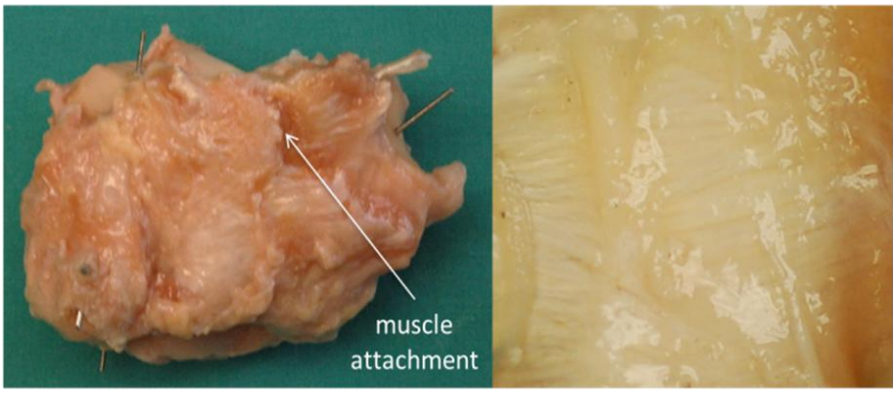


Figure 45. A TCL specimen illustrating the high variability in surface composition. Palmar view of the ligament with muscle attachment sites (left). Dorsal view of the ligament where individual ligamentous fiber bundles are evident (right).

The optimized Ogden coefficient values may have also been influenced by the tensile load applied to the ligaments in the radial/ulnar direction during indentation. Although the PMMA potting procedure was used to apply the tensile load parallel to the preferential orientation of collagen in the tissue (Prantil et al. 2010), the spindle shape of the TCL likely caused unequal tensioning across the proximal/distal width of the ligament. More specifically, the central region of the ligament appeared more tensioned than the proximal and distal edges. It was thought that this unequal tensioning of the collagen fibers along the proximal/distal direction may have caused

the center, radial and ulnar sites to be stiffer than the proximal and distal sites. However, the average μ coefficient at the proximal location was larger than the average coefficient at the center location, which is opposite of what would be expected for preferential tensioning centrally. The μ coefficients at the distal, radial and ulnar locations were all lower than the average values at the proximal and center sites. It is possible that the deviation of the μ coefficients from the expected trend may have been caused by the highly variable volar surface of the TCL. With regards to the α coefficient, there was no significant variation, despite whatever unequal tensioning of the ligament was actually present.

The average μ coefficients for the radial and distal site were lower than the average μ coefficient found for the central testing location. The radial and ulnar indentation sites were much closer to the carpal bone attachment sites compared the central indentation site, which may have influenced the Ogden coefficient values obtained. This was especially true for the ulnar site, where the hook of the hamate bends around the ulnar side of the tunnel and extends beneath the center of the ligament. In one specimen (number 3) the hook of the hamate extended all the way to the center of the ligament, which in combination with the specimen's small size, prevented indentation testing at the radial and ulnar sites for that particular specimen. Series-wide, despite there being different μ coefficients, there was no statistically significant difference between the radial, ulnar and center indentation sites. Again, statistically significant variation in coefficients associated with proximity to the carpal bones may have been masked by the highly variable μ coefficient.

The range of thickness measurements obtained at the different TCL indentation sites was from 1.4 mm up to 3.2 mm. These values were within the 0.6 mm to 3.6 mm range of values reported in literature for the thickness of the TCL (Rotman and Donovan 2002). The trend of variation in thickness found in this study along the proximal/distal direction was that the TCL was thicker at the distal test site and thinner at the central

and proximal test sites. This trend differed from that reported in literature, where the TCL was thickest at the center and thinner proximally and distally (Rotman and Donovan 2002). Again, difficulty of removing consistent amounts of muscle tissue and fascia at the different locations may have contributed to the discrepancy between the trends of TCL thickness values obtained in this study versus in the literature.

Preconditioning helped to obtain repeatable behavior between the three replicate indentation tests at each site. Without preconditioning, the first indentation test demonstrated more compliant tissue behavior than subsequent indentation tests. The cyclic preconditioning cycles to 10% strain allowed for three nearly identical indentation force/displacement curves to be obtained, with on average less than a 0.2 N difference in peak indentation force. This repeatability in the replicate indentation tests began to decrease once the TCL had been left in the saline bath for extended periods of time ( > 2 hours). This change in behavior may have been caused by the free-swelling of the tissue during the long immersion period. To avoid such artifact from being introduced into the experimental results, the TCL specimens were removed from the fluid bath after indentation testing at each site, and were allowed to recover outside the bath for approximately 20 minutes before beginning testing at the next location. While outside of the bath, the TCL specimens were covered with saline-soaked gauze to prevent the ligament from drying out.

The Ogden coefficients determined in this study reasonably describe the compressive properties of the TCL up to 40% strain. Although some proximal/distal gradient of tensioning of the collagen fibers may have been present, the reported coefficients are characteristic of TCLs under a 5 N load applied along the preferential collagen fiber orientation. The compressive properties determined for the TCL are suitable for implementation into FE models of the carpal tunnel, for purposes of understanding potential mechanisms of injury to the median nerve leading to the onset of CTS.

# CHAPTER VI: OVERALL DISCUSSION AND CONCLUSION

## Overview

The purpose of this work was to ascertain physiologically relevant mechanical property definitions for the digital flexor tendons, median nerve, and TCL for usage in FE models of the entire carpal tunnel. Such models offer an attractive non-invasive means to study contact stress insult to the median nerve. Elevated median nerve contact stresses could potentially contribute to the development of CTS. With FE implementation of tissue material property definitions developed in this work, the whole-tunnel models could provide better understanding of the mechanism of injury to the median nerve than would be the case for assumed or indirectly inferred tissue properties.

The first stage of the project was to determine transverse compressive properties for the digital flexor tendons and median nerve under a single, physiological tensile load. This was done using an Ogden hyperelastic material property definition to model the compressive tissue behavior. A logical next extension was expansion of the characterization of the mechanical properties of the digital flexor tendons and median nerves, using a fiber-reinforced anisotropic hyperelastic material property definition. Using that definition, the tensile and transverse properties were combined to accurately reflect dependency of the transverse compressive properties of the flexor tendons and median nerve upon axial tensile load. The final project stage was to model compressive mechanical behavior of the TCL. This was done using a first-order Ogden material property definition and optimization techniques similar to those employed for the tendons and nerve. The results from this work are material property definitions for the digital flexor tendons, median nerve, and TCL appropriate for implementation into FE models of contact stress in the carpal tunnel.

## Comparison of Ogden and Anisotropic Hyperelastic Material Definitions for the Flexor Tendons and Median Nerve

In the transverse-only model of the digital flexor tendons and median nerve, two Ogden coefficients were used to characterize the transverse compressive behavior of the tissues. This material property definition provided an accurate representation of the experimental compression data, beginning from the initial load uptake region, and extending into the more linear region of the force/displacement curve. Even in the worst instances, only minimal divergence was observed between the experimental data and Ogden FE characterization of the tissue behavior. Divergence of the two curves typically occurred only at compression higher than 35%, where the first-order Ogden material property definition was only able to accommodate the increasingly steep slope of the experimental curves. Because this divergence only occurred in the last 5% or so of tissue compression, the model provided an accurate representation of the compressive tissue behavior within the range of physiologic strain values determined in Chapter III (28% for the digital flexor tendons and 40% for the median nerve). Divergence may occur if extrapolated past the 40% compression to simulate more extreme loading activities beyond the wrist flexion and isometric hand loading activities used to evaluate the physiological strain range (Main et al. 2011).

Despite the fact that the Ogden material property definition provided good-quality fits, it was limited in that it only characterized the transverse compressive behavior of the flexor tendons and median nerve under a single axial tensile load. Thus, the next stage of the work was to model the transverse compressive behavior of the tissues under variable axial tensile loads. This step was necessary to accommodate the variability of tendon tensile loads that result from a variety of functional hand activities.

The fiber-reinforced anisotropic hyperelastic material property definition used to simultaneously model the tensile and transverse compressive properties of the tendons

and nerve utilized a Neo-Hookean material property definition to model the matrix material of the tissues. By definition, Neo-Hookean material property characterization uses only a single coefficient to describe material behavior. This is in contrast to the two coefficients used with the first-order Ogden model. As a result, the Neo-Hookean material property definition used for the matrix material was not able to accommodate all of the nonlinearity associated with the lengthy toe regions of the transverse compression curves. Unlike the excellent curve fits observed with the Ogden property definition in the transverse-only model, when using the anisotropic hyperelastic property definition, FE characterization of the tissue behavior tended to diverge from the experimental data between 10 – 20% tissue compression (Figure 46). Hence, the fits to the transverse compression curves obtained with the Neo-Hookean model, while reasonable first approximations, consistently fit the experimental data less well than did the Ogden model.

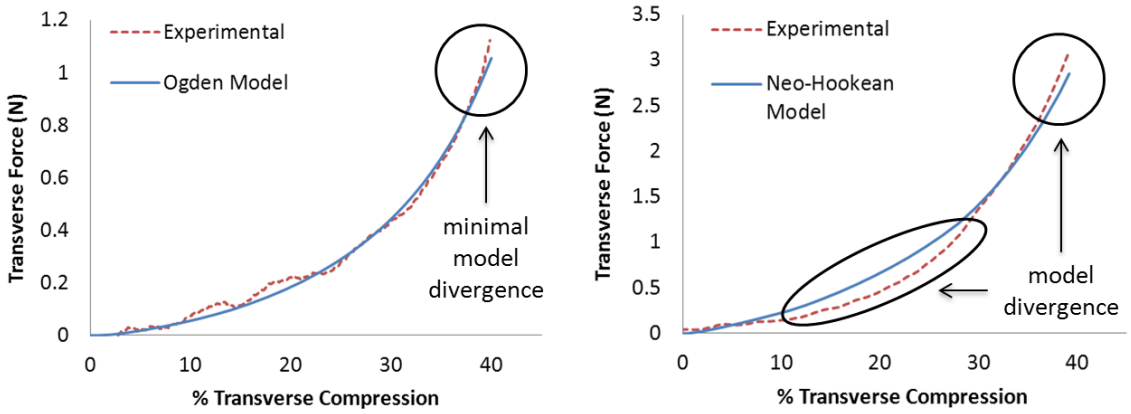


Figure 46. Transverse force versus percent compression plots, illustrating divergence of the FE model characterization of the tissue behavior from the experimental data for both the Ogden material property definition (left) and the Neo-Hookean material property definition (right).

The attraction of the Neo-Hookean fiber-reinforced material property definition was its allowance for the characterization of the transverse compressive behavior of the tissues at multiple axial loads, a major advantage over the simplified Ogden transverse-only model. The Neo-Hookean characterization of the matrix material was programed into the strain energy density function for the anisotropic hyperelastic material property definition available in ABAQUS. Future work to improve the transverse compression curve fits might involve implementation of a more complex fiber-reinforced material property definition with an alternative constitutive representation of the matrix material. Perhaps the use of a first-order Ogden material property definition for the matrix material would provide a better representation of the transverse compressive behavior of the flexor tendons and median nerve. However, a new strain energy density function incorporating an Ogden model would need to be generated and implemented into ABAQUS.

Prior to the use of the first-order Ogden material property definition in the transverse-only model, a Neo-Hookean material property definition was explored for the transverse compression behavior of several of the tendon and nerve specimens. The average material coefficient ($C_{10}$) obtained for those transverse-only Neo-Hookean fits was 25 kPa for the tendon specimens and 6 kPa for the median nerve specimens. Because the Neo-Hookean material property definition was used to represent the matrix material within the fiber-reinforced model, it is interesting to compare transverse-only Neo-Hookean $C_{10}$ coefficients to those obtained in the anisotropic hyperelastic material property definition. The average $C_{10}$ coefficients in the fiber-reinforced model were 2 kPa for the flexor tendons and 0.04 kPa for the median nerve. These Neo-Hookean coefficient values were significantly smaller than those obtained in the transverse-only model, despite resulting in nearly identical quality of curve-fits to the experimental transverse compression data (Figure 47).

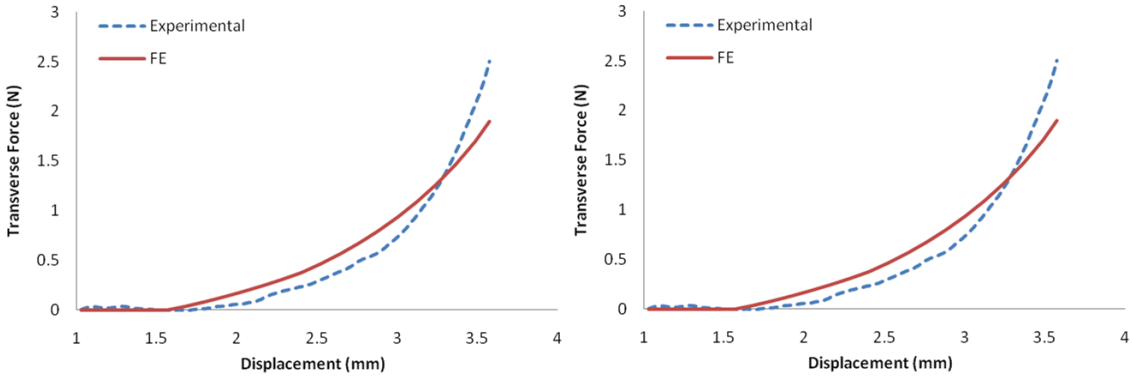


Figure 47. Illustrative curve fits of experimental transverse compression data using a Neo-Hookean material property definition with the transverse-only model (left), and the fiber-reinforced anisotropic hyperelastic material property definition that employs a Neo-Hookean material property definition to characterize the matrix material (right).

Clearly the Neo-Hookean coefficient associated with the fiber-reinforced model were dramatically smaller than those in the transverse-only Neo-Hookean model. This is likely because transverse behavior within the anisotropic hyperelastic material property definition probably would be dominated by the stiff axial fibers. The bow-stringing of taut fibers running along the length of the tissue may have contributed to the apparent compressive stiffness during transverse load application. If the transverse load was borne primarily by fibers bow-stringing, the need for stiffness in the matrix material would be minimal. For the transverse-only FE models, there were no axially oriented fibers to support the transverse compressive load, so the bulk mechanical properties of the tissue would need to be higher in order to uptake the transverse loading. Thus, the stiff axial fibers within the anisotropic hyperelastic material property model logically explain the low Neo-Hookean coefficients implicitly associated with the matrix material of the tissue.

## Comparison of Ogden Coefficients Between the Flexor Tendons, Median Nerve, and TCL

The optimized Ogden coefficient values for the flexor tendons, median nerve, and TCL were compared across all specimens tested. For both the μ and α coefficients, the TCL was significantly stiffer than either the flexor tendons or median nerve (Table 7). With the TCL being significantly stiffer, contact occurring between the median nerve and the TCL at the volar side of the carpal tunnel logically would tend to elicit the development of greater contact stresses on the nerve than would result from contact between the median nerve and the digital flexor tendons.

Table 7. Average Ogden coefficients for the flexor tendons, median nerve, and TCL.

| Tissue | u (kPa) | | α | |
|---|---|---|---|---|
| | **Average** | *St. Dev.* | **Average** | *St. Dev.* |
| Superficial Tendons | **35** | *16* | **9** | *4* |
| Deep Tendons | **40** | *22* | **9** | *5* |
| FPL | **12** | *10* | **11** | *4* |
| Median Nerve | **13** | *5* | **7** | *5* |
| TCL | **122** | *99* | **16** | *2* |

The loading modality used to evaluate the compressive stiffness of the TCL corresponded to the ligament's evolved physiologic function as a pulley for the digital flexor tendons. For the flexor tendons, the evolved physiologic function was for axial loading and not transverse compression. The decreased transverse stiffness of the flexor tendons may be a result of the tissues lack of functionally relevant loading in the transverse orientation. With regards to the median nerve, the tissue does not functionally carry an axial tensile or transverse compressive load. This lack of

mechanical loading may lead to the minimal transverse stiffness observed with this tissue.

The tensile load applied to the TCL during indentation testing was an approximation of the ligament loading during a grip activity (Schuind et al. 1995). In contrast, the axial tensile load applied to the flexor tendons during transverse compression testing was characteristic of an isometric pinch activity with a fingertip force of approximately 5 N (Dennerlein 2005). Although different functional activities were used to inform the respective tensile loads applied to the TCL versus the flexor tendons during transverse testing, differences in the mechanical properties of the two tissues would still have been observed.

## Literature Comparison

Due to the limited existing literature regarding the transverse compressive behavior of the digital flexor tendons and the median nerve, it is difficult to compare the experimental transverse stiffness measurements made in this work with literature data. For the axial tensile properties of the flexor tendons, many of the tissue stiffness values previously reported are simply Young's moduli for higher strain regions of the stress-strain curve. In the present work, the flexor tendons and median nerve were not axially tensioned to loads high enough to involve tissue deformation substantially beyond the toe-region of the stress-strain curve. However, the loadings applied in present work were based on physiologically relevant loads experienced during functional activities. Since the present experimental data did not extend well beyond the toe-region, an estimation of the Young's modulus values for comparison to literature values would not be very meaningful. However, there is one study in literature where a toe-region modulus of 10.5 MPa was reported for ovine digital flexor tendons under tensile loading (Lynch et al. 2003). To generate a comparable modulus value for the present study, a toe-region modulus was inferred from the slope of a stress-strain curve obtained from

data extracted from FE models during the axial extension step of the analysis. The tensile stress-strain data were obtained from the FE model, because as noted, no strain values were calculated from the experimental data. An approximate modulus of 0.4 MPa was inferred with this estimation technique, which is substantially lower than the value reported for the ovine flexor tendons. The difference between the two modulus values may be a result of differential loading and variable functional activities associated with the two species.

The experimentally obtained stiffness values for the TCL indentation testing can also be compared to information in the literature. To do this, the nominal stiffness of each experimental curve was evaluated in terms of the slope of the force/displacement curve within the 30-40% tissue strain region, which corresponds to the relatively linear region of the force/displacement curve. The average stiffness across all specimens in this 30-40% strain region was 18 N/mm (range of 3 N/mm to 75 N/mm). As a point of comparison, surface indentations performed with an ultrasound probe had previously found the stiffness of the overlying skin/TCL layer to be 6.72 N/mm, and the stiffness of the TCL/carpal tunnel tissues layer to be 15.63 N/mm (Zheng et al. 2006). The wide range of experimental stiffness measurements obtained during TCL indentation in the present work includes the measurement for the skin/TCL layer reported in literature.

Influence of Preconditioning and Hydration

The influence of preconditioning on tendon behavior has been studied extensively, but to the author's knowledge only in association with axial tensile properties. Preconditioning has been shown to increase the slope of the linear region of the stress-strain curve for tendon axial loading (Sverdlik and Lanir 2002). Another documented effect of preconditioning is an increase in the gauge length (the stress-free length) of the tissue (Sverdlik and Lanir 2002). The amount of preconditioning needed to reach a steady response in replicate axial extension tests has ranged from 3 cycles

(Shin et al. 2008), all the way up to 1000 cycles (Sverdlik and Lanir 2002). During compression testing of tendons, some studies have neglected to perform any preconditioning (Shin et al. 2008; Williams et al. 2008), while others have used replicate loading and unloading cycles (Lee et al. 2000). Since no consistent preconditioning protocol has been established in the literature, the preconditioning protocols used predicated simply on obtaining consistent behavior across the replicate tests. For the TCL indentation testing, preconditioning was chosen based on obtaining repeatable behavior for the three indentation tests performed at each TCL testing site. During the transverse compression tests and axial tension tests performed on the digital flexor tendons and median nerves, no preconditioning was used, because consistent behavior across the three replicate compression or extension tests spontaneously occurred (Figure 48).

According to the literature, tissue hydration during compression influences the measured mechanical behavior of tissues. For example, the tensile strength of tendons was found to be higher when the tissue was measured while submerged in a saline bath, as compared to when the tissue was simply moistened with saline (Haut and Haut 1997). In some of the preliminary transverse compression testing performed on tendons, a saline bath was not used. The stiffness of the tissues tested without a saline bath was significantly higher than the measurements obtained subsequently with the tissues submerged in the saline bath. Due to the dependency of axial tensile and transverse compressive tendon properties upon hydration state, all definitive specimen testing was done with the specimens submerged in a saline bath.

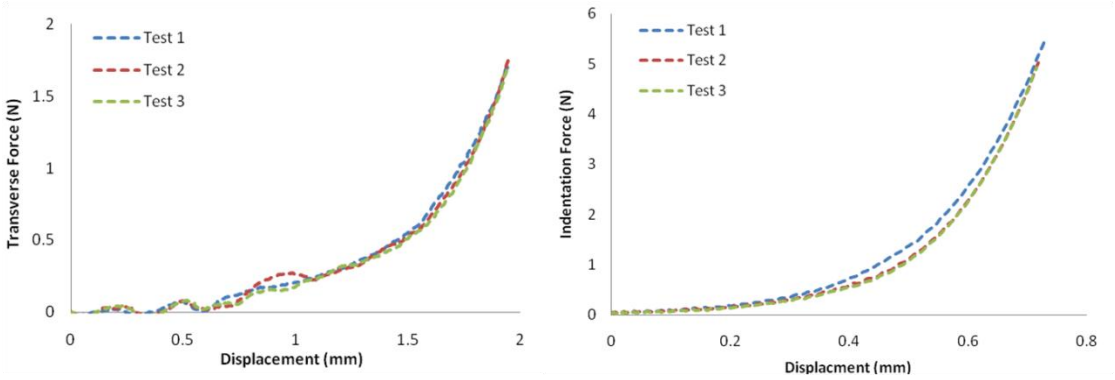


Figure 48. Typical repeatability of tissue behavior across replicate tests during transverse compression of tendons (left) and during indentation of the TCL (right).

## Conclusion

The constitutive information from the present study provides important foundational data to support further investigation of the soft tissue mechanics within the carpal tunnel, and will ultimately serve to improve understanding of the development of carpal tunnel syndrome. The material coefficients determined in this study can be implemented in anatomically-based FE models of the carpal tunnel, which in turn can be used to assess the contact stresses in the median nerve resulting from impingement by the surrounding digital flexor tendons and/or from abutment against the TCL. Also, the tensile and transverse compressive properties of the flexor tendons and median nerve that were determined using the fiber-reinforced model can potentially be applied to anatomic FE models to examine a broad range of CTS-provocative functional load activities.

# REFERENCES

AAOS. 2007. Clinical practice guideline on the diagnosis of carpal tunnel syndrome. American Academy of Orthopaedic Surgeons.

Armstrong, T. J., and D. B. Chaffin. 1978. An investigation of the relationship between displacements of the finger and wrist joints and the extrinsic finger flexor tendons. *J Biomech* 11 (3):119-28.

Aroori, S., and R. A. Spence. 2008. Carpal tunnel syndrome. *Ulster Med J* 77 (1):6-17.

Badger, S. A., M. E. O'Donnell, J. M. Sherigar, P. Connolly, and R. A. Spence. 2008. Open carpal tunnel release--still a safe and effective operation. *Ulster Med J* 77 (1):22-4.

Bay, B. K., N. A. Sharkey, and R. M. Szabo. 1997. Displacement and strain of the median nerve at the wrist. *J Hand Surg Am* 22 (4):621-7.

Bickel, K. D. 2010. Carpal tunnel syndrome. *J Hand Surg Am* 35 (1):147-52.

Bland, J. D., and S. M. Rudolfer. 2003. Clinical surveillance of carpal tunnel syndrome in two areas of the United Kingdom, 1991-2001. *J Neurol Neurosurg Psychiatry* 74 (12):1674-9.

Bureau of Labor Statistics. 1999. Lost-Worktime Injureis and Illnesses: Characteristics and Resulting Time Away From Work. U.S. Department of Labor.

Chao, E. Y., J. D. Opgrande, and F. E. Axmear. 1976. Three-dimensional force analysis of finger joints in selected isometric hand functions. *J Biomech* 9 (6):387-96.

Chen, R. J., C. C. Lin, and M. S. Ju. 2010a. In situ biomechanical properties of normal and diabetic nerves: an efficient quasi-linear viscoelastic approach. *J Biomech* 43 (6):1118-24.

Chen, R. J., C. C. Lin, and M. S. Ju. 2010b. In situ transverse elasticity and blood perfusion change of sciatic nerves in normal and diabetic rats. *Clin Biomech (Bristol, Avon)* 25 (5):409-14.

Clavert, P., J. F. Kempf, F. Bonnomet, P. Boutemy, L. Marcelin, and J. L. Kahn. 2001. Effects of freezing/thawing on the biomechanical properties of human tendons. *Surg Radiol Anat* 23 (4):259-62.

Cobb, T. K., B. K. Dalley, R. H. Posteraro, and R. C. Lewis. 1993. Anatomy of the flexor retinaculum. *J Hand Surg Am* 18 (1):91-9.

Dennerlein, J. T. 2005. Finger flexor tendon forces are a complex function of finger joint motions and fingertip forces. *J Hand Ther* 18 (2):120-7.

Dennerlein, J. T., E. Diao, C. D. Mote, Jr., and D. M. Rempel. 1998. Tensions of the flexor digitorum superficialis are higher than a current model predicts. *J Biomech* 31 (4):295-301.

Foley, M., B. Silverstein, and N. Polissar. 2007. The economic burden of carpal tunnel syndrome: long-term earnings of CTS claimants in Washington State. *Am J Ind Med* 50 (3):155-72.

Garcia-Elias, M., K. N. An, W. P. Cooney, 3rd, R. L. Linscheid, and E. Y. Chao. 1989. Stability of the transverse carpal arch: an experimental study. *J Hand Surg Am* 14 (2 Pt 1):277-82.

Gasser, T. C., R. W. Ogden, and G. A. Holzapfel. 2006. Hyperelastic modelling of arterial layers with distributed collagen fibre orientations. *J R Soc Interface* 3 (6):15-35.

Giannini, S., R. Buda, F. Di Caprio, P. Agati, A. Bigi, V. De Pasquale, and A. Ruggeri. 2008. Effects of freezing on the biomechanical and structural properties of human posterior tibial tendons. *Int Orthop* 32 (2):145-51.

Goetz, J. E., D. R. Thedens, N. M. Kunze, E. A. Lawler, and T. D. Brown. 2010. Day-to-day variability of median nerve location within the carpal tunnel. *Clin Biomech (Bristol, Avon)* 25 (7):660-5.

Goodman, H. J., and J. Choueka. 2005. Biomechanics of the flexor tendons. *Hand Clin* 21 (2):129-49.

Grewal, R., J. Xu, D. G. Sotereanos, and S. L. Woo. 1996. Biomechanical properties of peripheral nerves. *Hand Clin* 12 (2):195-204.

Harris, E. H., L. B. Walker, Jr., and B. R. Bass. 1966. Stress-strain studies in cadaveric human tendon and an anomaly in the Young's modulus thereof. *Med Biol Eng* 4 (3):253-9.

Haut, T. L., and R. C. Haut. 1997. The state of tissue hydration determines the strain-rate-sensitive stiffness of human patellar tendon. *J Biomech* 30 (1):79-81.

Holzapfel, G. A., T. C. Gasser, and R. W. Ogden. 2000. A new Constitutive Framework for Arterial Wall Mechanics and a Comparative Study of Material Models. *Journal of Elasticity* 61:1-48.

Idler, R. S. 1985. Anatomy and biomechanics of the digital flexor tendons. *Hand Clin* 1 (1):3-11.

Ju, M. S., C. C. Lin, J. L. Fan, and R. J. Chen. 2006. Transverse elasticity and blood perfusion of sciatic nerves under in situ circular compression. *J Biomech* 39 (1):97-102.

Ju, Ming-Shaung, Chou-Ching K. Lin, and Chang-Wei Lin. 2004. Transverse elasticity of rabbit sciatic nerves tested by in vitro compression. *Journal of the Chinese Institute of Engineers* 27 (7):965 - 971.

Katz, J. N., and B. P. Simmons. 2002. Clinical practice. Carpal tunnel syndrome. *N Engl J Med* 346 (23):1807-12.

Kendall, W. W. 1988. Results of treatment of severe carpal tunnel syndrome without internal neurolysis of the median nerve. *J Bone Joint Surg Am* 70 (1):151.

Keogh, J. P., I. Nuwayhid, J. L. Gordon, and P. W. Gucer. 2000. The impact of occupational injury on injured worker and family: outcomes of upper extremity cumulative trauma disorders in Maryland workers. *Am J Ind Med* 38 (5):498-506.

Kilbreath, S. L., and S. C. Gandevia. 1994. Limited independent flexion of the thumb and fingers in human subjects. *J Physiol* 479 ( Pt 3):487-97.

Kline, S. C., and J. R. Moore. 1992. The transverse carpal ligament. An important component of the digital flexor pulley system. *J Bone Joint Surg Am* 74 (10):1478-85.

Ko, C., and T. D. Brown. 2007. A fluid-immersed multi-body contact finite element formulation for median nerve stress in the carpal tunnel. *Comput Methods Biomech Biomed Engin* 10 (5):343-9.

Ko, C., M.J. Rudert, and T.D. Brown. 2007. A Technique for Determination of Transverse Material Properties of Human Flexor Digitorum Tendons. Paper read at American Society of Biomechanics, at Stanford, CA.

Kunze, N. M., J. E. Goetz, D. R. Thedens, T. E. Baer, E. A. Lawler, and T. D. Brown. 2009. Individual flexor tendon identification within the carpal tunnel: A semi-automated analysis method for serial cross-section MR images. *Orthop Res Rev* 1:31-42.

Kuo, P. L., P. C. Li, and M. L. Li. 2001. Elastic properties of tendon measured by two different approaches. *Ultrasound Med Biol* 27 (9):1275-84.

Lee, S. B., T. Nakajima, Z. P. Luo, M. E. Zobitz, Y. W. Chang, and K. N. An. 2000. The bursal and articular sides of the supraspinatus tendon have a different compressive stiffness. *Clin Biomech (Bristol, Avon)* 15 (4):241-7.

Li, Z. M., J. Tang, M. Chakan, and R. Kaz. 2009. Carpal tunnel expansion by palmarly directed forces to the transverse carpal ligament. *J Biomech Eng* 131 (8):081011.

Li, Z.M. 2005. Gender Difference in Carpal Tunnel Compliance. *Journal of Musculoskeletal Research* 9 (3):153-9.

Lin, R., E. Lin, J. Engel, and J. J. Bubis. 1983. Histo-mechanical aspects of carpal tunnel syndrome. *Hand* 15 (3):305-9.

Lynch, H. A., W. Johannessen, J. P. Wu, A. Jawa, and D. M. Elliott. 2003. Effect of fiber orientation and strain rate on the nonlinear uniaxial tensile material properties of tendon. *J Biomech Eng* 125 (5):726-31.

Main, E. K., J. E. Goetz, M. James Rudert, C. M. Goreham-Voss, and T. D. Brown. 2011. Apparent transverse compressive material properties of the digital flexor tendons and the median nerve in the carpal tunnel. *J Biomech* 44 (5):863-8.

Millesi, H., G. Zoch, and R. Reihsner. 1995. Mechanical properties of peripheral nerves. *Clin Orthop Relat Res* (314):76-83.

Mondelli, M., F. Giannini, and M. Giacchi. 2002. Carpal tunnel syndrome incidence in a general population. *Neurology* 58 (2):289-94.

Palmer, D. H., and L. P. Hanrahan. 1995. Social and economic costs of carpal tunnel surgery. *Instr Course Lect* 44:167-72.

Phalen, G. S. 1966. The carpal-tunnel syndrome. Seventeen years' experience in diagnosis and treatment of six hundred fifty-four hands. *J Bone Joint Surg Am* 48 (2):211-28.

Powell, H. C., and R. R. Myers. 1986. Pathology of experimental nerve compression. *Lab Invest* 55 (1):91-100.

Prantil, R.K., K.H. Xiu, K.E. Kim, D. Gaitan, M.S. Sacks, S. L. Woo, and Z.M. Li. 2010. The Orientation of Collagen Fibers of the Transverse Carpal Ligament. Paper read at ASB, at Providence, RI.

Rempel, D. M., and E. Diao. 2004. Entrapment neuropathies: pathophysiology and pathogenesis. *J Electromyogr Kinesiol* 14 (1):71-5.

Rotman, M. B., and J. P. Donovan. 2002. Practical anatomy of the carpal tunnel. *Hand clinics* 18 (2):219-230.

Rotman, M. B., and P. R. Manske. 1993. Anatomic relationships of an endoscopic carpal tunnel device to surrounding structures. *J Hand Surg Am* 18 (3):442-50.

Rydevik, B., G. Lundborg, and U. Bagge. 1981. Effects of graded compression on intraneural blood blow. An in vivo study on rabbit tibial nerve. *J Hand Surg Am* 6 (1):3-12.

Rydevik, B., and C. Nordborg. 1980. Changes in nerve function and nerve fibre structure induced by acute, graded compression. *J Neurol Neurosurg Psychiatry* 43 (12):1070-82.

Schuind, F., W. P. Cooney, R. L. Linscheid, K. N. An, and E. Y. Chao. 1995. Force and pressure transmission through the normal wrist. A theoretical two-dimensional study in the posteroanterior plane. *J Biomech* 28 (5):587-601.

Schuind, F., M. Garcia-Elias, W. P. Cooney, 3rd, and K. N. An. 1992. Flexor tendon forces: in vivo measurements. *J Hand Surg Am* 17 (2):291-8.

Shin, R. H., C. Zhao, M. E. Zobitz, P. C. Amadio, and K. N. An. 2008. Mechanical properties of intrasynovial and extrasynovial tendon fascicles. *Clin Biomech (Bristol, Avon)* 23 (2):236-41.

Skie, M., J. Zeiss, N. A. Ebraheim, and W. T. Jackson. 1990. Carpal tunnel changes and median nerve compression during wrist flexion and extension seen by magnetic resonance imaging. *J Hand Surg Am* 15 (6):934-9.

Sperka, P., N. Cherry, R. Burnham, and J. Beach. 2008. Impact of compensation on work outcome of carpal tunnel syndrome. *Occup Med (Lond)* 58 (7):490-5.

Stecco, C., and R. Aldegheri. 2008. Historical review of carpal tunnel syndrome. *Chir Organi Mov* 92 (1):7-10.

Stecco, C., V. Macchi, L. Lancerotto, C. Tiengo, A. Porzionato, and R. De Caro. 2010. Comparison of transverse carpal ligament and flexor retinaculum terminology for the wrist. *J Hand Surg Am* 35 (5):746-53.

Stevens, J. C., S. Sun, C. M. Beard, W. M. O'Fallon, and L. T. Kurland. 1988. Carpal tunnel syndrome in Rochester, Minnesota, 1961 to 1980. *Neurology* 38 (1):134-8.

Summers, A. P., and T. J. Koob. 2002. The evolution of tendon--morphology and material properties. *Comp Biochem Physiol A Mol Integr Physiol* 133 (4):1159-70.

Sverdlik, A., and Y. Lanir. 2002. Time-dependent mechanical behavior of sheep digital tendons, including the effects of preconditioning. *J Biomech Eng* 124 (1):78-84.

Szabo, R. M., B. K. Bay, N. A. Sharkey, and C. Gaut. 1994. Median nerve displacement through the carpal canal. *J Hand Surg Am* 19 (6):901-6.

Tung, W. L., C. Zhao, Y. Yoshii, F. C. Su, K. N. An, and P. C. Amadio. 2010. Comparative study of carpal tunnel compliance in the human, dog, rabbit, and rat. *J Orthop Res* 28 (5):652-6.

Viikari-Juntura, E., and B. Silverstein. 1999. Role of physical load factors in carpal tunnel syndrome. *Scand J Work Environ Health* 25 (3):163-85.

Wang, J. H. 2006. Mechanobiology of tendon. *J Biomech* 39 (9):1563-82.

Wehbe, M. A., and J. M. Hunter. 1985. Flexor tendon gliding in the hand. Part I. In vivo excursions. *J Hand Surg Am* 10 (4):570-4.

Williams, L. N., S. H. Elder, J. L. Bouvard, and M. F. Horstemeyer. 2008. The anisotropic compressive mechanical properties of the rabbit patellar tendon. *Biorheology* 45 (5):577-86.

Wilson, W. F., and J. T. Hueston. 1973. The intratendinous architecture of the tendons of flexor digitorum profundus and flexor pollicis longus. *Hand* 5 (1):33-8.

Zheng, Y. P., Z. M. Li, A. P. Choi, M. H. Lu, X. Chen, and Q. H. Huang. 2006. Ultrasound palpation sensor for tissue thickness and elasticity measurement--assessment of transverse carpal ligament. *Ultrasonics* 44 Suppl 1:e313-7.